FRAGMENTATION OF QUARK AND GLUON JETS IN PROTON-ANTIPROTON COLLISIONS AT $\sqrt{s} = 1.8$ TeV

By

ALEXANDRE P. PRONKO

A DISSERTATION PRESENTED TO THE GRADUATE SCHOOL
OF THE UNIVERSITY OF FLORIDA IN PARTIAL FULFILLMENT
OF THE REQUIREMENTS FOR THE DEGREE OF
DOCTOR OF PHILOSOPHY

UNIVERSITY OF FLORIDA

2005

I dedicate this work to my wife Anna and my parents, Vera Vladimirovna and Pavel Antonovich Pronko.

ACKNOWLEDGMENTS

I am very grateful to my advisor Prof. Andrey Korytov for his guidance and support throughout my research. His knowledge of and dedication to high-energy physics were a true inspiration for me. The greatest lessons I have learned from Prof. Korytov are that all things (even small ones) must make sense and that you really understand something if you can explain it in a few words.

I am very thankful to Dr. Alexei Safonov for his invaluable help and patience while I was making my first steps in this analysis. He also gave me an example of how to work hard and still enjoy physics.

I would like to thank Prof. Guenakh Mitselmakher and Prof. Jacobo Konigsberg for their contribution to the successful completion of this dissertation.

I also thank Prof. Anwar Bhatti, Prof. Luc Demortier, Prof. Sally Seidel, Dr. Robert Plunkett, Prof. Richard Field, and Prof. Joey Huston for their help and useful suggestions that were very important at different stages of this work.

I appreciate the opportunity I had to be a part of the University of Florida group at the Collider Detector at Fermilab (CDF). I enjoyed working with such great colleagues as Dr. Sergei Klimenko, Dr. Alexander Sukhanov, Dr. Song Ming Wang, Dr. Roberto Rossin, Valentin Necula, George Lungu, Sergo Jindariani, and Lester Pinera. I especially want to emphasize the role which Prof. Jacobo Konigsberg, the UF CDF group leader, played in making us a strong team.

I am thankful to Lester Pinera for carefully reading the manuscript and his helpful suggestions.

Special thanks are due to Bobby Scurlock, Valentin Necula, and Roberto Rossin who were my officemates at different periods of time. Without you guys, I would have

completed this thesis much faster, but my whole experience as a graduate student could have turned into a misery of solitary confinement in front of a computer. I very much enjoyed talking to you about what men can talk about: politics, society, science, music, life.

To my friend and colleague Dr. Maxim Titov, thank you for your friendship which started when I was at summer school at DESY and which continues today.

Finally, but most of all, I would like to thank Anna, my wife and best friend, and my parents for their unconditional love and continuous support.

TABLE OF CONTENTS

page

ACKNOWLEDGMENTS iv

LIST OF TABLES viii

LIST OF FIGURES x

ABSTRACT xiii

CHAPTER

1 INTRODUCTION 1

1.1 Standard Model of Elementary Particles 1
1.2 Quantum Chromodynamics 2
1.3 Jets of Hadrons 5

2 FRAGMENTATION OF QUARK AND GLUON JETS 7

2.1 Analytical Perturbative Approach (APA) to Jet Fragmentation . . 7
2.1.1 Modified Leading Log Approximation (MLLA) 9
2.1.2 Local Parton Hadron Duality Hypothesis (LPHD) 10
2.2 APA Predictions 12
2.2.1 Mean Multiplicity of Charged Particles 13
2.2.2 Difference between Quark and Gluon jets 14
2.3 Jet Fragmentation in Monte Carlo Event Generators 16

3 STUDIES OF QUARK AND GLUON JETS 20

3.1 Physics Motivation 20
3.2 Experimental History 21
3.3 Feasibility of Quark and Gluon Jet Studies at CDF 30
3.4 Analysis Strategy at CDF 32

4 ACCELERATOR AND DETECTOR 35

4.1 Tevatron during the 1993–1995 Running Period 35
4.2 CDF Design and Overview 37
4.2.1 Vertex Detectors (VTX and SVX) 39
4.2.2 Central Tracking Chamber (CTC) 40
4.2.3 Preshower and Shower Maximum Detectors, Calorimetry . 41
4.3 CDF Trigger System 44

5 JETS AT CDF 46

6 PHOTONS AT CDF 49

7 ANALYSIS TOOLS 51

8 MEASUREMENTS 53

8.1 Data Samples 53
8.2 Event Selection Cuts 53
8.3 Fraction of Gluon Jets 56
8.4 Fraction of Real Photons 57
8.5 Multiplicity Measurements 59
8.5.1 Track Cuts 60
8.5.2 Background Tracks Removal 62
8.5.3 Tracking Efficiency 63
8.6 Effect of Fake Photons 65
8.7 Final Corrections and Results 68

9 SYSTEMATIC UNCERTAINTIES AND CROSS-CHECKS 70

9.1 Event Selection 70
9.2 Jet Reconstruction and Energy Corrections 74
9.3 Presence of Fake Photons 79
9.4 PDF Uncertainties 82
9.5 Uncertainties in Multiplicity Measurements 82

10 DISCUSSION OF RESULTS 88

10.1 Multiplicity of Charged Particles in Gluon and Quark Jets 88
10.2 Momentum Distribution of Charged Particles in Gluon and Quark Jets. 93

11 SUMMARY AND CONCLUSION. FUTURE PERSPECTIVES 99

REFERENCES 102

BIOGRAPHICAL SKETCH 107

LIST OF TABLES

Table page

1–1 Properties of leptons. 3

1–2 Properties of quarks. 3

1–3 Gauge bosons and forces of the Standard Model. 4

2–1 Numerical values of the perturbative corrections for the parton multiplicity in gluon jets, N_g, and the ratio of multiplicities, $r = N_g/N_q$. . 13

3–1 The summary of model-independent measurements of the difference between quark and gluon jets conducted on e^+e^- machines. 28

3–2 The summary of model-independent measurements of the difference between quark and gluon jets conducted at e^+e^- machines using unbiased gluon jets. 30

3–3 The summary of model-dependent and indirect measurements of the difference between gluon jets and light flavor, $u-, d-, s-$, quark jets. 31

4–1 Selected parameters of the CDF Central Tracking Chamber. 41

4–2 The CDF Calorimeter System coverage and detector segmentation. . . 44

8–1 Fractions of gluon jets in dijet events and in 100% pure γ-jet events obtained using Herwig and Pythia along with various sets of parton distribution functions. 59

8–2 Efficiencies of the track selection cuts for jets with the average energy E_{jet}=41 GeV. 64

8–3 Efficiencies of the track selection cuts for jets with the average energy E_{jet}=52.5 GeV. 65

8–4 The α-correction due to difference in multiplicities between a regular jet and a jet opposite to a fake photon. 66

8–5 Results of the measurements with the default set of cuts. 68

8–6 Effect of K^0_s and Λ decays on the charged particle multiplicity within a cone of the opening angle θ_c=0.47. 69

8–7 Charged particle multiplicities in small cones around gluon and quark jet directions and their ratio, N_g, N_q and $r = N_g/N_q$ respectively. . . 69

9–1 The summary of systematic uncertainties in the measurements of N_g, N_q, and $r = N_g/N_q$ obtained for the opening angle $\theta_c = 0.47$. 85

9–2 The summary of systematic uncertainties in the measurements of N_g, N_q, and $r = N_g/N_q$ obtained for the opening angle $\theta_c = 0.36$. 86

9–3 The summary of systematic uncertainties in the measurements of N_g, N_q, and $r = N_g/N_q$ obtained for the opening angle $\theta_c = 0.28$. 87

9–4 Fraction of real photons in the photon+jet sample and its associated systematic uncertainties. 87

10–1 Monte Carlo results for charged particle multiplicities in small cones around gluon and quark jet directions and their ratio. 92

10–2 Measured values of the momentum distribution, $\frac{1}{N_{jet}}\frac{dN}{d\xi}$, of charged particles in gluon jets. 96

10–3 Measured values of the momentum distribution, $\frac{1}{N_{jet}}\frac{dN}{d\xi}$, of charged particles in quark jets. 97

10–4 Measured values of the ratio of momentum distributions, $r(\xi)$, of charged particles in gluon and quark jets. 98

LIST OF FIGURES

Figure page

2–1 Example of the distribution of charged particle transverse momenta with respect to the jet direction. 10

2–2 Theoretical predictions for the ratio of multiplicities in gluon and quark jets, $r = N_g/n_q$. 15

3–1 History of measurements of the ratio of charged particle multiplicities in gluon and quark jets. 27

4–1 Overview of the Fermilab accelerator complex. 36

4–2 Drawing of the CDF detector. 38

4–3 The CTC end plate view. 40

8–1 Invariant mass spectrum of dijet and photon+jet events which pass event selection cuts. 56

8–2 Transverse energy spectrum of jets and photons from dijet and photon+jet events after event selection cuts. 57

8–3 Fractions of gluon jets in dijet and γ+jet samples. 58

8–4 Example of the distribution of $\log p_T$ versus $\log d$ for tracks within a cone of θ_c=0.47 rad around the jet direction. 60

8–5 Illustration of correlation between transverse particle momentum, P_T, and impact parameter, d, for electrons and positrons produced in γ-conversions. 61

8–6 Example of the Δz distribution for tracks from events with only one vertex (primary interaction). 62

8–7 Illustration of the definition of complementary cones. 63

8–8 The correlation between multiplicity in complementary cones (per event) and dijet multiplicity (per event). 64

8–9 The ratio of the measured energy of a fake photon (detector level) to the real energy of a parent jet (MC parton level). 67

8–10 The ratio of the measured invariant mass of a *fake* γ+jet event (detector level) to the real invariant mass (MC parton level). 67

9–1 The angular distribution of particles in cone 0.47 around jet direction. 71

9–2 Energy balance in data: $|\vec{E}_{T_1} + \vec{E}_{T_2}|/(E_{T_1} + E_{T_2})$. 73

9–3 Energy balance in Herwig Monte Carlo: $|\vec{E}_{T_1} + \vec{E}_{T_2}|/(E_{T_1} + E_{T_2})$. . . 73

9–4 Difference in charged particle multiplicities between jets reconstructed with different clustering cone sizes. 76

9–5 Difference in charged particle multiplicities between jets reconstructed with different clustering cone sizes. 77

9–6 Angle between the direction of an outgoing parton and the direction of a reconstructed jet. 77

9–7 Invariant mass spectrum of Monte Carlo dijet and γ+jet samples. . . 78

9–8 Isolation energy distribution in photon+jet data and Monte Carlo *fake* γ+jet events. 81

9–9 The predicted real photon content as a function of the cut on isolation energy in a cone around photon candidate (dots—prediction based on the shape of the isolation energy distributions in data and Monte Carlo fakes, band—real photon fraction and its uncertainty based on the standard conversion method). 81

10–1 The ratio of charged particle multiplicities in gluon and quark jets as a function of jet hardness Q. 89

10–2 Average charged particle multiplicities in gluon and quark jets as a function of jet hardness Q. 90

10–3 Comparison of CDF results on charged particle multiplicity in gluon jets with recent model-dependent and indirect results from OPAL. . 90

10–4 Comparison of Monte-Carlo predictions to data: average charged particle multiplicities in gluon and quark jets. 92

10–5 Comparison of Monte-Carlo predictions to data: the ratio of charged particle multiplicities in gluon and quark jets. 93

10–6 The ratio of momentum distributions, $r(\xi)$ (where $\xi = \ln(1/x) = \ln(E_{jet}/p)$), of charged particles in gluon and quark jets. 94

10–7 Inclusive momentum distribution, $\frac{1}{N_{jet}}\frac{dN}{d\xi}$, of charged particles in gluon jets. 96

10–8 Inclusive momentum distribution, $\frac{1}{N_{jet}}\frac{dN}{d\xi}$, of charged particles in quark jets. 97

10–9 The ratio of momentum distributions, $r(\xi)$, of charged particles in gluon and quark jets. 98

Abstract of Dissertation Presented to the Graduate School
of the University of Florida in Partial Fulfillment of the
Requirements for the Degree of Doctor of Philosophy

FRAGMENTATION OF QUARK AND GLUON JETS
IN PROTON-ANTIPROTON COLLISIONS AT $\sqrt{s} = 1.8$ TeV

By

Alexandre P. Pronko

May 2005

Chair: Andrey Korytov
Major Department: Department of Physics

We report the first model independent measurement of charged particle multiplicities in quark and gluon jets, N_q and N_g, produced at the Tevatron in $p\bar{p}$ collisions with center-of-mass energy 1.8 TeV and recorded by the Collider Detector at Fermilab. The measurements are made for jets with average energies 41 and 53 GeV by counting charged particle tracks in cones with opening angle of θ_c=0.28, 0.36, and 0.47 rad around the jet axis. The corresponding jet hardness $Q = E_{jet}\theta_c$ varies in the range from 12 GeV to 25 GeV. At Q=19.2 GeV, the ratio of multiplicities $r = N_g/N_q$ is found to be 1.64±0.17, where statistical and systematic uncertainties are added in quadrature. The results are in agreement with re-summed perturbative QCD calculations and are consistent with recent e^+e^- measurements.

CHAPTER 1
INTRODUCTION

The quest to understand the building blocks of our universe is as old as the history of the human race itself. With time, our knowledge of nature has evolved from the *Doctrine of the Four Elements* of Empedocles to the *Standard Model of Elementary Particles* which is the most compelling theory describing the fundamental constituents of matter and their interactions. The Standard Model can be truly considered one of the great scientific triumphs of the 20th century.

1.1 Standard Model of Elementary Particles

The Standard Model states that all visible matter consists of fundamental particles of two kinds: *leptons* and *quarks*. Both leptons and quarks are spin 1/2 *fermions*. There are six leptons and six quarks which are grouped into three generations according to their mass. The known leptons are electron (e), muon (μ), tau (τ) and their associated neutrinos (ν_e, ν_μ, ν_τ). The known quarks are up (u), down (d), strange (s), charm (c), bottom (b) and top (t). Fermions are involved in four known interactions: gravitational, electromagnetic, weak interaction and strong interaction. With the exception of gravity, all interactions in the Standard Model are mediated by the exchange of another type of elementary particles with spin 1 known as gauge *bosons*. The electromagnetic interaction involves charged particles (all fermions except neutrinos), and it is mediated by the exchange of photons (γ). All known fermions participate in the weak interaction which is responsible for such processes as nuclear beta decay. The weak interaction is mediated by the exchange of three bosons: W^+, W^- and Z. Among all the fermions, only quarks participate in the strong interaction which is mediated by gluons (g). The strong force is responsible for, among other things, binding quarks together to form nucleons (protons and neutrons) and holding

protons and neutrons together inside atomic nuclei. The properties of fermions and bosons are summarized in Tables 1–1, 1–2 and 1–3.

The Standard Model is a quantum field theory which is based on the gauge symmetry $SU(3)_C \times SU(2)_L \times U(1)_Y$ [1]. This gauge group includes the symmetry group of the strong interaction, $SU(3)_C$ and the symmetry group of the unified electroweak interaction, $SU(2)_L \times U(1)_Y$. The Standard Model defines the dynamics of both the interacting fermions and the exchange vector bosons. It allows for the calculation of cross-sections of various processes and decay rates of different particles. The numerous experimental studies of the past 30 years show a very high level of consistency between data and Standard Model predictions. The best illustration of this agreement between theory and experiment is the discoveries of the W [2, 3] and Z [4, 5] bosons by the UA1 and UA2 collaborations at CERN and the top quark by the CDF and D0 collaborations at the Tevatron [6]. The last particle predicted by the Standard Model and yet to be discovered is the long hypothesized Higgs boson (H) which is introduced in theory to give particles their masses. The search for the Higgs boson is one of the most important experimental problems to be addressed during Run 2 at the Tevatron and the future LHC experiments.

1.2 Quantum Chromodynamics

Quantum Chromodynamics (QCD) is the theory of strong interactions between color charged objects which are quarks and gluons. The history of QCD starts with the idea of the parton model in the late 1960's. This idea arose out of necessity to explain the scaling observed in the SLAC experiment on deep inelastic scattering of electrons on hadrons [7]. The surprising result was that the measured cross-section did not fall off exponentially as the inelasticity of the reaction increased. Instead, it had a so-called Bjorken scaling [8] behavior which suggested existence of a point-like structure inside the target nucleons. This gave rise to the *parton* model [8, 9] in which the constituents of hadrons were identified with partons. This phenomenological

Table 1–1: Properties of leptons. The spin, charge (e) and mass are listed for each particle.

	Particle	Spin	Charge	Mass
1^{st} generation	e^-	1/2	-1	$0.51099892 \pm 0.00000004$ MeV/c^2
	ν_e	1/2	0	< 3 eV/c^2
2^{nd} generation	μ^-	1/2	-1	105.658369 ± 0.000009 MeV/c^2
	ν_μ	1/2	0	< 0.19 MeV/c^2
3^{rd} generation	τ^-	1/2	-1	$1776.99^{+0.29}_{-0.26}$ MeV/c^2
	ν_τ	1/2	0	< 18.2 MeV/c^2

Table 1–2: Properties of quarks. The spin, charge (e) and mass are listed for each particle. Additionally, each quark can also carry one of three color charges (blue, green, red) responsible for the strong interaction.

	Particle	Spin	Charge	Mass
1^{st} generation	u	1/2	+2/3	1.5-4 MeV/c^2
	d	1/2	-1/3	4-8 MeV/c^2
2^{nd} generation	c	1/2	+2/3	1.15-1.35 GeV/c^2
	s	1/2	-1/3	80-130 MeV/c^2
3^{rd} generation	t	1/2	+2/3	178.0 ± 4.3 GeV/c^2
	b	1/2	-1/3	4.1-4.4 GeV/c^2

understanding of SLAC scaling was soon extended to other hard scattering processes such as e^+e^- annihilation into hadrons and inclusive high $p_\perp$ hadron production in hadron-hadron collisions. However, the idea of what exactly a parton was remained elusive despite the phenomenological successes of the parton model.

Another important moment in the history of QCD is the idea of *quarks*. Quarks were proposed in 1964 [10] by Gell-Mann and Zweig based on the studies of hadron spectroscopy. As they pointed out, the observed patterns can be understood in terms of the hypothesis that hadrons are composite structures built from an elementary triplet of spin-1/2 quarks (u-, d-, s- quarks; the other three quarks, c-, b-, t-, were discovered much later), corresponding to the fundamental representation of $SU(3)$ group. The quark model appeared to be quite successful in describing the properties of existing hadrons and predicting new states. However, this model, in order not

Table 1–3: Gauge bosons and forces of the Standard Model. There are eight different species of gluons each corresponding to a particular color charge.

Boson	Force	Spin	Charge [e]	Mass [GeV/c^2]	Range [fm]
γ	electromagnetic	1	0	$< 6 \times 10^{-23}$	∞
W	weak	1	± 1	80.425 ± 0.038	$\simeq 10^{-3}$
Z	weak	1	0	91.1876 ± 0.0021	$\simeq 10^{-3}$
g	strong	1	0	0	$<\sim 1$

to contradict the Pauli exclusion principle, required quarks to have one property, less obvious but of central importance for the strong interaction. This property was proposed by Greenberg [11] and is known as *color*.

The final step in this chain of arguments which led to QCD is the discovery by Pollitzer, Gross and Wilczek of the asymptotically free field theory among the class of non-Abelian gauge theories [12]. It became apparent that the gauge symmetry of this new theory is the local color transformation and the symmetry group which is generated by these transformations is the non-Abelian Lie group $SU(3)_C$. Therefore, three possible color charges of a quark are assumed to be the fundamental representation of the group and the gauge bosons mediating the strong interaction are eight gluons carrying double color charge. This model became known as Quantum Chromodynamics.

The most intriguing properties of the Quantum Chromodynamics are confinement and the asymptotic freedom. The consequence of confinement is that the free quarks (*i.e.* free color charges) are not observed in nature. What we see is hadrons which are colorless combinations of quarks. The existence of confinement suggests that the interaction between quarks becomes very strong at large distances so that they remain bound together. The other peculiar property of QCD is the asymptotic freedom which predicts that quarks inside hadrons (*i.e.* at very short distances) should behave almost as free particles. The asymptotic freedom is responsible for

the Bjorken scaling which was for the first time observed in a famous SLAC experiment on deep inelastic scattering [7]. Both asymptotic freedom and confinement are the consequences of unusual (different from electroweak interaction) behavior of the QCD coupling α_S. The dependence of the coupling $\alpha_S(Q)$ on the energy scale Q (also known as running of α_S) is given by the solution of the renormalization group equation [13]:

$$\alpha_S(Q^2) = \frac{4\pi}{b \ln (Q^2/\Lambda^2)}, \tag{1.1}$$

where $b = (33 - 2n_f)/3$, n_f is the number of active quark flavors (for which $m_q < Q$), Q is the energy scale or momentum transfer and Λ is a parameter with dimension of energy at which the coupling would diverge if extrapolated down to small Q. The value of Λ depends on the renormalization scheme, number of active flavors and can also be defined to leading or next-to-leading order. Experimental measurements of Λ (in the modified minimal subtraction scheme [13] and five active flavors) yield values of around 200 MeV [14]. The form of Eq. 1.1 suggests that the $\alpha_S(Q)$ becomes large and perturbation theory breaks down, for scales comparable with the masses of the light hadrons, *i.e.* $Q \simeq 1$ GeV. This is an indication that the confinement of quarks and gluons inside hadrons is actually a consequence of the growth of the coupling at low scale, which is opposite to the decrease at high scales that leads to the asymptotic freedom. This behavior of the QCD coupling is the result of the non-Abelian nature of the strong interaction which is characterized by the presence of self-interaction of gauge bosons (*i.e.*, the theory contains three- and four-gauge-boson vertices). It is these additional interactions that makes QCD so rich in various phenomena.

1.3 Jets of Hadrons

One of the most spectacular manifestations of the QCD is the existence of jets of hadrons which we see in detectors as collimated sprays of particles. It was first observed by the MARK1 collaboration at SPEAR in 1975 [15] that quarks produced in

e^+e^- collision appeared as hadronic jets. Five years later, the experiments at PETRA [16] proved the existence of jets from gluon emission in quark pair production. To get an idea of how jet formation happens, we need to consider a process of bremsstrahlung gluon radiation off a parton (quark or gluon). The differential spectrum of gluon radiation off a quark with momentum p is given by the well-known formula [17]:

$$dw^{q\to q+g} = \frac{\alpha_S(k_\perp)}{4\pi} 2C_F \left[1 + \left(1 - \frac{k}{p}\right)^2\right] \frac{dk}{k} \frac{dk_\perp^2}{k_\perp^2}, \tag{1.2}$$

$$\alpha_S(k_\perp) = \frac{2\pi}{b \ln\left(k_\perp/\Lambda\right)}, \quad C_F = (N_C^2 - 1)/2N_C = 4/3, \tag{1.3}$$

where $N_C = 3$ is the number of colors and k is the gluon momentum. By examining this formula, we can see that jet formation is driven by the quasi-collinear and/or soft gluon emissions [17]:

$$Intrajet\ activity : k_\perp \ll k \ll p \to w \sim \alpha_S \ln^2 p \sim 1 \tag{1.4}$$

At the same time, large angle emission off a parton with large momentum p can lead to an extra gluon jet, however, with a small probability [17]:

$$Multijet\ topology : k_\perp \sim k \sim p \to w \sim \alpha_S/\pi \ll 1 \tag{1.5}$$

The stage of parton cascade development is then followed by the hadronization stage when quarks and gluons from the parton shower pick up color matching partners from the sea of virtual quarks and gluons and become observable hadrons. Therefore, jets of hadrons are as close as we can get experimentally to "seeing" quarks and gluons.

CHAPTER 2
FRAGMENTATION OF QUARK AND GLUON JETS

This chapter gives an overview of the theoretical picture of quark and gluon jet fragmentation. We will consider currently available perturbative QCD (pQCD) tools for calculating a basic jet observable such as multiplicity of charged particles. We will also review models of jet fragmentation implemented in Monte Carlo event generators.

2.1 Analytical Perturbative Approach (APA) to Jet Fragmentation

When trying to obtain a quantitative description of jet properties, we have to remember that the fragmentation is a manifestation of both asymptotic freedom and confinement properties of the strong interaction. Perturbative QCD is applicable only if the strong coupling, α_S, is relatively small, *i.e* in the regime of high momentum transfers when the concept of free partons is valid. It is during this stage when the cascade of quarks and gluons develops, thus, forming the structure of a jet. However, what we see in detectors are not quarks and gluons but hadrons which are formed during the confinement stage of jet formation. In this regime, the strong coupling becomes too large, rendering perturbation theory ineffective. Fortunately, as Eq. 1.1 suggests, it happens at relatively small momentum transfers compatible with the masses of light hadrons (<1 GeV). Thus, we may hope that much of the jet structure developed during the parton branching with higher momentum transfers should remain unaltered by hadronization. The data from e^+e^- and ep collisions indeed confirmed that, phenomenologically, distributions of hadrons and partons look very similar. This has led to the hypothesis of local parton hadron duality (LPHD) [18]. The LPHD has provided an important link between the perturbative QCD calculations performed for partons and the experimental observables for hadrons. The

framework of pCQD and LPHD forms the so-called analytical perturbative approach (APA) to QCD jet physics. The goal of which is to describe the structure of the multi-hadronic final states with the minimal reference to the hadronization dynamics. By confronting the APA predictions with experimental data, we aim to find the areas of applicability and the limitations of this perturbative approach.

The success of the parton description of deep inelastic scattering (DIS) prompted detailed studies of QCD parton cascades. Historically, attempts to quantify logarithmic deviations from the true Bjorken scaling behavior has led to the development of the so-called Leading Log Approximation (LLA) [19]. In the LLA, the contributions to structure functions on the order of $\alpha_S^n \ln^n(Q^2)$ are resummed in all orders while the terms without large logs are neglected. The origin of this $\alpha_S \ln Q^2$ scaling breakdown stems from the fact that the parton's transverse momentum inside hadron is not restricted to be small. Thus, a quark can emit a gluon and acquire large transverse momentum $k_\perp$ with probability $w^{q\to q+g} \sim \int \alpha_S \; dk_\perp^2/k_\perp^2$ (see Eq. 1.3). The integral extends up to the kinematic limit $k_\perp^2 \sim Q^2$ and gives rise to the famous logarithmic scaling violation. The LLA was also extended to the e^+e^- annihilations for fragmentation functions in the region of finite momentum fractions, $0.1 < x < 1.0$.

Despite its success in DIS, the LLA is not enough to obtain a satisfying description of jet fragmentation which, as it was already shown (Eq. 1.5 in Chapter 1), is dominated by the soft gluon emissions. The dynamics of soft particles in jets is, to some extent, accounted for by the so-called Double Log Approximation (DLA) [20]. The DLA was initially developed for pure gluonic systems and was designed to account for only leading double logarithmic contributions, $\alpha_S \ln^2 Q^2 \sim 1$, while neglecting contributions of the order $\alpha_S \ln Q^2 \ll 1$ and $\alpha_S \ll 1$. This approximation is the simplest analytical representation of the QCD parton cascade. In the DLA, one re-sums in all orders terms $\alpha_S^n \ln^{2n} Q^2$ arising from double logarithmic (DL) infrared and collinear singularities of gluon emission ($q\to qg$, $g\to gg$ processes), but ignores the

energy and momentum conservation. The DLA is too crude for making quantitative predictions and is only valid at very high energies. However, it is conceptually simple and allows for qualitative description of many effects in jet fragmentation.

It is important to mention the role that color coherence effects play in the development of partonic cascades. Color coherence effects are common to any gauge theory. In jet fragmentation, they manifest themselves in a suppression in production of very soft particles compared to those with intermediate energies ($E_{had} \sim E_{jet}^{0.3-0.4}$). Coherence effects also result, on average, in a strong *angular ordering* (AO) [21] of consecutive gluon emissions. The essence of AO is that the soft gluon in a parton cascade is emitted only inside a cone formed by its two immediate predecessors. The effect of strong AO in QCD helps to present the pattern of the parton cascade in terms of purely probabilistic picture of Markov chains of independent elementary radiation events. This probabilistic scheme significantly simplifies large log re-summation in all orders of α_S.

2.1.1 Modified Leading Log Approximation (MLLA)

In order to make successful a quantitative description of jet evolution, one has to account for the sub-leading single logarithmic (SL) effects ($g \to q\bar{q}$ and $q \to qg$, $g \to gg$ splitting with hard momenta) on the order of $\alpha_S^n \ln^{2n-1} Q^2$ along with the leading double logs, $\alpha_S^n \ln^{2n} Q^2$ (DLA accuracy). This is done within the so-called Modified Leading Log Approximation (MLLA or also referenced as next-to-Leading Log Approximation, NLLA) [22], where SL and DL contributions are re-summed in all orders of α_S.

The only MLLA parameter, Q_{eff}, is the cut-off on the minimal allowed parton momentum with respect to the parent parton. It sets the lower limit on the parton virtuality, thus, playing the role of the effective parton mass. The Q_{eff} cutoff can also be considered as the scale below which non-perturbative hadronization effects

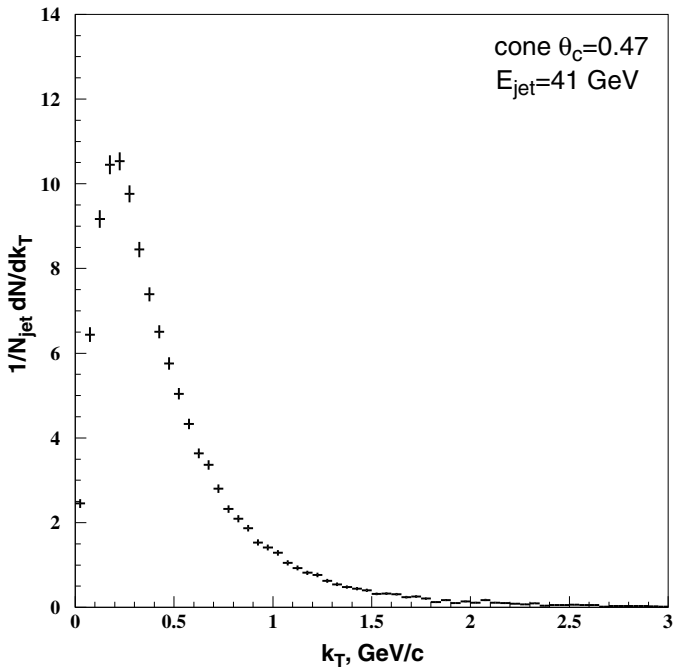

Figure 2–1: Example of the distribution of charged particle transverse momenta with respect to the jet direction. The distribution is obtained for particles within a cone θ_c=0.47 around jets from dijet events.

dominate in the jet formation. The value of Q_{eff} is not defined in the theory, but rather has to be determined experimentally.

Fig. 2–1 shows an example of the distribution of charged particle transverse momenta with respect to the jet direction, $k_\perp$. From this plot, one can see that most of particles have $k_\perp < 1$ GeV and, therefore, belong to the region where analytical calculations are very challenging. Spectrum of transverse momenta, $k_\perp$, in data also suggests that, in order for the MLLA to be a successful model of jet fragmentation, Q_{eff} has to be on the order of a few hundred MeV (Q_{eff} ~200 MeV).

2.1.2 Local Parton Hadron Duality Hypothesis (LPHD)

The application of pQCD to multiparticle production is not possible without an additional assumption about the hadronization stage of jet evolution which is governed by color-confinement. As mentioned before, such a link between partons and hadrons is provided by the hypothesis of local parton hadron duality, LPHD [18].

The LPHD assumes that the hadronization occurs locally at the end of the parton shower development. In other words, the conversion of partons to hadrons happens at a low virtuality scale on the order of hadronic masses ($Q_{eff} \sim$ few hundred MeV), it does not depend on the scale of the primary hard process, and it involves only small momentum transfers. Therefore, results obtained for partons with $k_\perp > Q_{eff}$ should apply to hadrons as well. The origin of this local duality is in the pre-confinement properties [23] of the QCD cascade: the color charge is locally compensated and the color neutral clusters of limited masses are formed in the cascade.

The naive interpretation of the LPHD is that every parton picks up color matching partners from the sea of virtual quarks and gluons and becomes a hadron which "remembers" the direction and momentum of the original parton. Therefore, one can assume that for sufficiently inclusive observables the following relation should hold:

$$O(x_1, x_2, ...)|_{hadrons} = K_{LPHD} O(x_1, x_2, ..., Q_{eff}, \Lambda)|_{partons} \tag{2.1}$$

In other words, the inclusive momentum distributions for partons and hadrons in jets are the same apart from a possible normalization. The same should be also true for the average multiplicities in jet:

$$N_{hadrons} = K_{LPHD} N_{partons}. \tag{2.2}$$

It is important to mention that one should not expect a one-to-one match between partons and hadrons on event-by-event basis, but only in their average behavior as well as in fluctuations around the average. Finally, the LPHD is expected to be asymptotically correct because the sensitivity to the cut-off decreases with the increasing energy.

2.2 APA Predictions

In this section, we will discuss the APA predictions for the mean charged particle multiplicities in gluon and quark jets. The multiplicities of hadrons are a very fundamental characteristic of jets, and they are given considerable attention in experimental measurements. The predictions for particle multiplicities in jets are based on calculations carried out in the framework of MLLA [17] and its extensions [24, 25, 26, 27], supplemented with the LPHD hypothesis [18]. Traditionally, the solutions of pQCD equations are obtained for the multiplicity of partons in gluon jets, N_g^{parton}, and for the ratio, $r = N_g^{parton}/N_q^{parton}$, of parton multiplicities in gluon and quark jets.

Theoretically, the parton multiplicity in a jet of energy E_{jet} is calculated for partons in a small cone defined by an opening angle, θ_c, around the direction of the initial quark or gluon emerging from $q\bar{q}$ or gg color singlet source [17]. The multiplicity $N^{parton}(y)$ depends only on one scaling variable $y = \ln(Q/Q_{eff}) = \ln(E_{jet}\theta_c/Q_{eff})$, where $Q = E_{jet}\theta_c$ is the jet hardness and Q_{eff} is the k_T cut-off for partonic cascade (in MLLA, Q_{eff} can be taken as low as Λ). To accommodate the multiplicity measurements performed at e^+e^- colliders for all charged particles in the full solid angle, the theoretical predictions are often extended to cones as large as a whole hemisphere, or $\theta_c = \pi/2$. Strictly speaking, this goes beyond the precision of the pQCD calculations and there is no unique prescription for doing such extrapolations. However, it seems natural to use $Q = 2E_{jet}tan(\theta_c/2)$ that has the correct limit at small opening angles and remains Lorentz-invariant for large angles with respect to boosts along the jet direction. For a full hemisphere, the energy scale becomes $Q = 2E_{jet}$. The definition of a scale in the case of three-jet events in e^+e^- collisions with all jets at large angles with respect to each other is even more ambiguous and we postpone this discussion till next chapter where we will review results obtained at e^+e^- colliders.

Table 2–1: Numerical values of the perturbative corrections for the parton multiplicity in gluon jets, N_g, and the ratio of multiplicities, $r = N_g/N_q$.

n_f	a_1	a_2	a_3	r_1	r_2	r_3
3	0.280	-0.379	0.209	0.185	0.426	0.189
4	0.297	-0.339	0.162	0.191	0.468	0.080
5	0.314	-0.301	0.112	0.198	0.510	-0.041

2.2.1 Mean Multiplicity of Charged Particles

According to the recent so-called next-to-next-to-next-to-Leading Log Approximation ($3NLLA$ extension of $MLLA$) [26], the mean parton multiplicity in gluon jets is given by

$$N_g^{parton}(y) = y^{-a_1 c^2} \exp\left\{ 2c\sqrt{y} + \frac{c}{\sqrt{y}}\left[2a_2c^2 + \frac{\beta_1}{\beta_0^2}(\ln 2y + 2)\right] + \frac{c^2}{y}\left[a_3c^2 - \frac{a_1\beta_1}{\beta_0^2}(\ln 2y + 1)\right]\right\}, \tag{2.3}$$

where coefficients a_i (i=1-3) are given in Table 2–1, and other parameters are defined below:

$$y = \ln(Q/Q_{eff}) = \ln(E_{jet}\theta_c/Q_{eff}), \quad c = (4N_C/\beta_0)^{1/2},$$
$$\beta_0 = \frac{11N_C - 2n_f}{3}, \quad \beta_1 = \frac{17N_C^2 - n_f(5N_C + 3C_F)}{3}.$$

In Eq. 2.3, the pre-exponential term and the first term in the exponent correspond to the $MLLA$ expression for multiplicity. The second term in the exponent, proportional to $c/\sqrt{y}$, is the $NNLLA$ [25] correction. The third term in the exponent, proportional to c^2/y is the $3NLLA$ result. The role of the $3NLLA$ correction is not important compared to the lower order terms because of the smallness of a_3. It is interesting to note that the $NNLLA$ and $3NLLA$ corrections are almost constant and somewhat compensate each other at currently accessible energies. Therefore, the $MLLA$ expression for gluon jets is a good approximation to the higher order result.

Strictly speaking, the next-to-$MLLA$ calculations ($NNLLA$ and $3NLLA$) are not the next order calculations of the contributions into the amplitudes of the branching processes. However, these terms are of some relevance because they include energy conservation at improved level of accuracy.

2.2.2 Difference between Quark and Gluon jets

In QCD, quarks and gluons have different probabilities (proportional to their color factors, C_F=4/3 and C_A=N_C=3 respectively, also frequently referred to as "color" charges) to emit gluons, and it is therefore expected that jets produced by quarks and gluons will exhibit a difference in their fragmentation properties. This difference is best characterized by the ratio of hadron multiplicities in gluon and quark jets, $r = N_g/N_q$. The asymptotic (at $E_{jet} \to \infty$) value of r is simply a ratio of gluon and quark color factors, $r = C_A/C_F = 9/4$ (DLA, see ref. [28]). At present energies, however, the asymptotic value of r can be achieved in the soft limit of the particle spectrum [29]. The inclusion of two loop α_S corrections [24] (one loop in $MLLA$) and energy conservation [25] up to $NNLLA$ level reduces the ratio to, respectively, $r \sim 2.1$ and $r \sim 1.7$ at experimentally accessible energies. Even higher order corrections which further diminish the predicted ratio, $r = N_g/N_q$, are obtained in the next-to-next-to-next-to-leading order ($3NLLA$ [26]):

$$r = \frac{C_A}{C_F}(1 - r_1\gamma_0 - r_2\gamma_0^2 - r_3\gamma_0^3), \tag{2.4}$$

where coefficients r_i (i=1-3) are given in Table 2–1, and γ_0 is defined below:

$$\gamma_0 = \sqrt{2N_C\alpha_S/\pi}, \quad \alpha_S = \frac{2\pi}{\beta_0 y}\left[1 - \frac{\beta_1 \ln(2y)}{\beta_0^2 y}\right].$$

The theoretical results discussed above for the ratio are presented in Fig. 2–2. Despite the fact that various calculations disagree on the absolute value of ratio, they all predict a weak dependence on the energy scale. These calculations also show the relative importance of the higher order α_S corrections and energy conservation. The

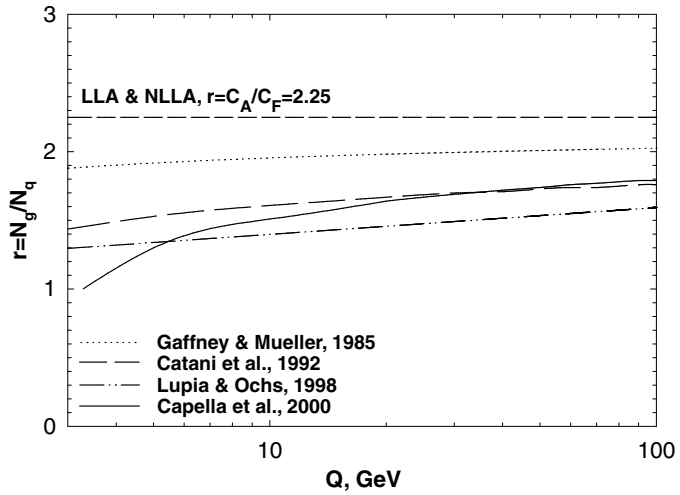

Figure 2–2: Theoretical predictions for the ratio of multiplicities in gluon and quark jets, $r = N_g/n_q$.

strict energy conservation and a corresponding limitation on the available phase space can be included even more accurately by solving the evolution equations numerically. This solution is presented in ref. [27]. The exact numerical solution reduces the ratio, $r = N_g/N_q$, by another 10% compared with the $3NLLA$ predictions.

As it was already mentioned above, the pQCD equations are traditionally solved for the multiplicity in gluon jets, N_g, and for the ratio of multiplicities in gluon and quark jets, $r = N_g/N_q$. Therefore, the $3NLLA$ prediction for the multiplicity in quark jets, N_q, is simply given by $N_q = N_g/r + O(\gamma_0^5)$ [26]:

$$N_q^{parton}(y) = \frac{C_F}{C_A} y^{-a_1 c^2} \exp\left\{ 2c\sqrt{y} + \frac{c}{\sqrt{y}}\left[r_1 + 2a_2 c^2 + \frac{\beta_1}{\beta_0^2}(\ln 2y + 2) \right] + \frac{c^2}{y}\left[r_2 + \frac{r_1^2}{2} + a_3 c^2 - \frac{a_1 \beta_1}{\beta_0^2}(\ln 2y + 1) \right] \right\}. \quad (2.5)$$

We also have to mention that the theoretical calculations discussed above are performed in the limit of massless quarks, i.e. applicable to light u-,d- and s- quarks only. Finally, the corresponding expectation of hadron multiplicities in jets is provided by

Eq. 2.2, $N_{g,q}^{hadrons} = K_{LPHD} N_{g,q}^{partons}$. The LPHD assumes that the constant K_{LPHD} is the same for gluons and light quarks.

2.3 Jet Fragmentation in Monte Carlo Event Generators

In this section, we will consider implementation of jet fragmentation in Monte Carlo (MC) event generators. Nowadays, Monte Carlo simulation is widely used for visualization of not only detector performance but also of physics phenomena. There are a number of specialized and general purpose MC event generators, among which Herwig [30] and Pythia [31] are, probably, the most popular general purpose ones.

Jet fragmentation in both Herwig and Pythia includes two steps: perturbative initial- and final-state parton branching, and conversion of final partons to hadrons via phenomenological hadronization models. This approach gives a good description of diverse jet evolution phenomena with relatively few adjustable parameters. Both generators were tuned to reproduce inclusive event characteristics (charged particle multiplicity and momentum spectra, event shapes, etc.) and inclusive spectra of identified hadrons in $e^+e^- \to hadrons$ reaction at the center-of-mass energy around the Z^0 pole.

The parton shower models of Herwig and Pythia are very similar. The cascade evolution is treated as a branching process based on the LLA. There are three types of parton splitting in this picture: $q \to qg$, $g \to gg$ and $g \to q\bar{q}$. The probability for the decay of parton a with virtual mass m_a into partons b and c is given by the "DGLAP" evolution equation [32] (used to be known as Altarelli-Parisi evolution equation):

$$\frac{dw_{a\to bc}}{dt} = \int dz \frac{\alpha_S(Q^2)}{2\pi} P_{a\to bc}(z), \tag{2.6}$$

where the evolution parameter t is related to parent's virtuality by $t{=}\ln(m_a^2/\Lambda^2)$ in case of Pythia. The evolution in Herwig is done in terms of $t{=}\ln(\zeta_a^2/\Lambda^2)$ (essentially

in terms of emission angle θ_{bc}), where ζ_a is defined by

$$\zeta_a = E_a\sqrt{\xi_{bc}}, \quad \xi_{bc} = \frac{p_b \cdot p_c}{E_b E_c}, \tag{2.7}$$

where p_b, p_c, E_b and E_c are the four-momenta and energies of partons b and c. The strong coupling $\alpha_S(Q^2)$ in Eq. 2.6 is evaluated at Q^2 equal to the transverse momentum squared of the branching. The splitting function $P_{a\to bc}(z)$ is used to generate the energy fractions z and $1-z$ of daughter partons. The QCD coherence effects are included in both Herwig and Pythia, however, with some difference. Thus, Herwig has an exact implementation of the angular ordering in initial- and final-state radiation via its evolution parameter ζ_a (see Eq. 2.7). In the case of Pythia, the angular ordering is implemented via ordering parton's virtuality and vetoing non-ordered angles. Azimuthal asymmetries for gluon decays both from coherence and spin effects are also included in Herwig and Pythia. The treatment of hard gluon emission in Herwig is improved by matching of the first gluon branching to the three-jet matrix element (NLO accuracy for high x). In both generators, the parton shower is terminated when the parton virtualities drop below Q_{cutoff}.

The real difference between Herwig and Pythia is in the implementation of the hadronization. Herwig exploits a so-called cluster model of hadronization [33] which is motivated by the preconfinement [23] property of the parton branching. The implementation of the cluster model is the following. At the end of the parton shower, all gluons are forced to non-perturbatively split into $q\bar{q}$ pairs. Neighboring $q\bar{q}$ pairs then form color-neutral clusters which decay isotropically in their rest frame into (usually) two hadrons. Special treatment is given to very light clusters, which are allowed to "decay" into a single hadron, and to very heavy clusters which can decay into clusters before decaying into hadrons. Baryons are produced from cluster decays into baryon-antibaryon pairs, i.e. clusters themselves always have zero baryon number. If a cluster contains a quark from the perturbative parton shower (not from

gluon splitting), the hadron formed from this quark "remembers" the original quark's direction (given by angular probability distribution $P(\theta^2) \sim e^{-\theta^2/2\theta_0^2}$). The advantage of the cluster model is its simplicity and that the global event shape and the hadron momentum spectrum are largely determined by the parameters, Λ and Q_{cutoff}, governing the parton shower, and to a lesser extent by the thresholds for clusters of too high and too low mass. The hadron flavor composition is mainly driven by the available phase space in cluster decay, in other words, by the cluster mass spectrum which is asymptotically Q-independent and universal.

The conversion of partons to hadrons in Pythia is accomplished by the Lund String Model [34]. It is easier to understand the concept of string fragmentation using an example of the $q\bar{q}$ pair production in e^+e^- annihilation. Neglecting for the moment the soft gluon radiation, the produced quark and antiquark move out in opposite directions, losing energy to the color field, which collapses into a string-like configuration between them. The string has a uniform energy per unit length, corresponding to a linear quark confining potential. The string then breaks up into hadrons through spontaneous $q\bar{q}$ pair production in its intense color field. The addition of gluon radiation results in kinks on the string, each initially carrying localized energy and momentum equal to that of its parent gluon. During a string breakup in its rest frame, the (equal and opposite) transverse momenta of quarks from a $q\bar{q}$ pair are generated according to a Gaussian distribution of width σ_q. Longitudinal hadron momenta are determined by means of phenomenological fragmentation functions: the Lund symmetric function for light (u,d,s) quarks, and the Peterson [35] function for c and b quarks. Baryon production is included by allowing diquark-antiquark pairs to be created. Meson production in the string between baryon and antibaryon is also allowed. The string model has a few parameters to describe the energy-momentum spectra of produced hadrons and many parameters to describe their flavor composition. The string model was tested extensively in e^+e^- collisions and showed an

excellent agreement with the data. However, it has a complicated structure and the presence of a large number of phenomenological parameters somewhat shadows the perturbative information.

CHAPTER 3
STUDIES OF QUARK AND GLUON JETS

This Chapter presents the motivation for measurements of quark and gluon jet differences at CDF and provides an overview of early experimental results. The feasibility and strategy of the analysis at CDF are also discussed.

3.1 Physics Motivation

Jet evolution is driven by multi-gluon emission with very small momentum transfers and is governed by soft QCD. Studies of jet fragmentation probe the region where pQCD calculations are notoriously difficult. They also facilitate investigation of the transition between the pQCD and non-pQCD domains. One aspect of fragmentation studies is the measurement of the mean charged particle multiplicities in gluon and quark jets. As it was discussed in Chapter 2, pQCD has a very definite prediction about the ratio of these multiplicities, $r = N_g/N_q$. The difference between quark and gluon jets is at the heart of QCD. Therefore, not surprisingly, it has sparked much of experimental interest. Measurements of the multiplicity differences between quark and gluon jets have a long history. Most of these measurements come from e^+e^- colliders. The pQCD calculations imply $r\sim$1.4-1.7 in the range of experimentally accessible jet energies. The earliest measurements of the ratio $r = N_g/N_q$ were consistent with 1 (see [36, 37] and the next section). Over the 10-year LEP era, the reported values varied from $r\simeq$1.1 to $r\simeq$1.5 [36] most of which had small uncertainties and were significantly below the theoretical predictions, $r\sim$1.4-1.7 (see Fig. 3–1). It should also be pointed out that there is a certain amount of controversy around some of these measurements related to the difficulties and possible biases arising from the necessity to identify and manipulate three-jet events—the only source of gluon jets at LEP (this is left for discussion in the next section). Therefore, the range of e^+e^-

results motivates an independent measurement of r in a different environment such as $p\bar{p}$ collisions.

The e^+e^- experiments have conducted very detailed studies of the fragmentation in quark jets. These measurements cover a wide range of jet energies from ~5 GeV to ~105 GeV. On the other hand, there are only two model-independent measurements of gluon jet properties at well defined scales (see next section). This definitely motivates more studies of gluon jets. Finally, jet fragmentation data from the Tevatron will complement measurements from e^+e^- and ep experiments, providing a unique test of the universality of jets.

There is also a practical motivation for studies of quark and gluon jets. Good understanding of jet fragmentation is important for the success of high-P_T physics programs of Run II at the Tevatron and future LHC experiments. Utilizing the differences in quark and gluon jet evolution can be an effective tool for reduction of QCD backgrounds in measurements involving b-jets and/or jets from $W^{\pm}\to q`\bar{q}"$ and $Z\to q\bar{q}$ decays. One of the analyses which can potentially benefit from this is the study of top quark properties in $t\bar{t}\to b\bar{b}jjjj$ channel, where the signal is all quark jets and the background is many gluon jets.

Many analyses rely on simulation of jets by Monte Carlo event generators (e.g., jet energy corrections, acceptance and background estimations). Despite the fact that both Herwig and Pythia were tuned to reproduce jet fragmentation in e^+e^- annihilations, it is not clear if they will perform equally well in the much more complicated and diverse environment of $p\bar{p}$ collisions. This makes it very important to compare quark and gluon jet fragmentation in data and Monte Carlo.

3.2 Experimental History

Most early experimental results on the differences between quark and gluon jets come from e^+e^- machines. Studying gluon jets in e^+e^- annihilations is not a trivial

task as one has to look for $q\bar{q}g$ events and identify which of the three jets is the gluon jet. A brief review of these measurements is given below.

One of the first quoted results on ratio, $r = N_g/N_q$, was obtained by the HRS collaboration. The analysis was based on selecting threefold symmetric $e^+e^- \to q\bar{q}g$ events where the quark and gluon jets were produced at about the same energies $E \simeq$10 GeV [38]. The probability for a gluon jet to have higher multiplicity was tested by assuming the Poissonian multiplicity distribution and independent production of each of the three jets (very naive assumptions). A value $r = 1.29^{+0.29}_{-0.46}$ was obtained.

The first result from LEP was obtained by the OPAL collaboration [39]. The "Y" shape events from $e^+e^- \to Z^0 \to hadrons$ were selected for the analysis. The ratio was found to be consistent with unity, $r = 1.02 \pm 0.04$(stat.), for jets with energies about 24 GeV. The analysis was based on a comparison of the multiplicity in different hemispheres with respect to the plane which was perpendicular to the three-jet event plane and contained the highest energy jet. The gluon-tagged and normal-mixture jets were used for the analysis. The results were not corrected for quark and gluon jets misidentification.

The ratio started climbing up with improvements in the experimental technique. The "Y" shape events from Z^0 peak were used in the next OPAL work [40]. The highest energy jet was assumed to be a quark jet. The lower energy jets were used to measure multiplicities. The angle between each of the lower energy jets and the leading jet was $150^o \pm 10^o$. The so-called k_T algorithm [41] was used to reconstruct jets and assign particles to them. The charged particle multiplicities in quark and gluon jets were derived from comparison of gluon-tagged jets and mixed jets. Monte Carlo was used to obtain the flavor composition of the sample. The results were presented for the energy scale $Q = E_{jet} = 24$ GeV. The average charged particle multiplicities in gluon and quark jets were $N_g = 9.10 \pm 0.10$ and $N_{q(NFM)} = 6.86 \pm 0.09$ respectively

(here and further, NFM stands for "natural flavor mixture"[1]). The obtained ratio was $r = N_g/N_{q(NFM)} = 1.326 \pm 0.054 \pm 0.073$. The results were not corrected for detector acceptance and resolution.

The SLD collaboration used essentially the same technique in their studies of quark and gluon jets from "Y" type events [42]. The only difference was that gluon jets were compared to jets originating from light flavor (u, d, s) quarks. The results were reported for the energy scale $Q = E_{jet} = 24$ GeV. The measured ratio was $r = N_g/N_{uds} = 1.294 \pm 0.064^{+0.047}_{-0.064}$.

The OPAL measurement [43] essentially repeated the previous [40] study with only slight improvements. This time, tuned Monte Carlo was used to derive sample purities and unfold multiplicity. The updated values were $N_g = 9.10 \pm 0.07 \pm 0.09$, $N_{q(NFM)} = 7.27 \pm 0.07 \pm 0.08$ and $r = N_g/N_{q(NFM)} = 1.251 \pm 0.024 \pm 0.073$.

In the next OPAL paper [44], the same approach was used to study differences between light quark jets and gluon jets. The corresponding results were $N_g = 9.16 \pm 0.07 \pm 0.12$, $N_{uds} = 6.18 \pm 0.06 \pm 0.13$ and $r = N_g/N_{uds} = 1.390 \pm 0.038 \pm 0.032$. The results were reported for the energy scale of $Q = E_{jet} = 24.4$ GeV. A novel part of this work was that all measurements were repeated with the cone jet finder and multiplicity was measured in the jet cone ($R = 30^o$). The corresponding results were $N_g = 6.18 \pm 0.06 \pm 0.13$, $N_{uds} = 5.44 \pm 0.05 \pm 0.04$ and $r = N_g/N_{uds} = 1.135 \pm 0.031 \pm 0.029$. The reported hardness scale was $Q = E_{jet} = 24.4$ GeV.

The ALEPH collaboration has also studied quark and gluon jets from "Y" shape events at the Z^0 peak [45] employing the same method as OPAL and SLD. Apart from light quarks, gluon jets were also compared to c- and b-flavor jets. For the energy scale $Q = E_{jet} = 24$ GeV, ALEPH has reported the following results: $N_g =$

[1] According to PDG [14], the fractions of u, d, s, c, b quark jets produced in $Z^0 \rightarrow hadrons$ are 14.5%, 23.3%, 23.79%, 16.79% and 21.62%, respectively.

$9.90 \pm 0.10 \pm 0.27$, $N_{uds} = 7.90 \pm 0.44 \pm 0.26$, $r = N_g/N_{uds} = 1.249 \pm 0.084 \pm 0.022$ and $r = N_g/N_{q(NFM)} = 1.194 \pm 0.027 \pm 0.019$.

Various techniques were employed in analysing data from the Z^0 peak by the DELPHI collaboration [46]. Quark and gluon jets were studied in symmetric "Y"-type and "Mercedes"-type events. For both event types, jets from tagged and mixed samples were used to find multiplicities in quark and gluon jets. In "Y" events, the highest energy jet was assumed to be a quark. The gluon jet was identified by tagging one of the lower energy jets as b-quark. The jets from the mixed sample had to fail heavy flavor tagging. In "Mercedes" events, the angle between jets was $120^o \pm 15^o$. The gluon jet was identified by tagging two other jets as b-quarks. The k_T-finder was used to reconstruct jets and assign tracks. Tuned Monte Carlo was used to derive sample purities and unfold multiplicity. The ratio from the analysis of "Y"-type events was measured to be $r = N_g/N_{uds} = 1.279 \pm 0.021 \pm 0.020$. The reported ratio from the analysis of "Mercedes"-type events was $r = N_g/N_{uds} = 1.323 \pm 0.053 \pm 0.020$ for the energy scale $Q = E_{jet} = 30.4$ GeV. The results from the analysis of symmetric $q\bar{q}g$ and $q\bar{q}\gamma$ events were also quoted in the same paper [46]. The method was similar to the analysis of "Y"-type events. The gluon jet was identified by tagging one of the lower energy jets as a b-quark. The multiplicity in quark jets of reduced energy was obtained from $q\bar{q}\gamma$ events. The $JADE$ [47] and k_T algorithms were used to reconstruct jets and assign particles. The reported energy scale was $Q = E_{jet} = 26.6$ GeV. The quark jet sample contained 33% of c-quarks and 11% of b-quarks which was slightly different from the NFM sample. The results obtained with k_T and $JADE$ algorithms were $r = N_g/N_{udscb} = 1.232 \pm 0.022 \pm 0.018$ and $r = N_g/N_{udscb} = 1.369 \pm 0.019 \pm 0.035$, respectively.

All the analyses discussed so far were based on the comparison of jets in twofold or threefold symmetric 3-jet events. These measurements suffered from one major problem—the ambiguous assignment of particles to jets in three-jet events which

heavily depended on the details of the particular jet finding algorithm (such jets are called *biased*). As a consequence, the results obtained with different algorithms were very inconsistent. The other basic problem was related to improper choice of the energy scale for comparison of the data and theory. Thus, the results were reported for the jet energy as the scale of fragmentation. However, it was later shown in ref. [48] that it is not the jet energy which describes the fragmentation of jets in three-jet events. Therefore, the discussed results are biased and cannot be used for comparison to theory predictions and CDF data.

The problems described above were realized and avoided in the later measurements by CLEO and OPAL. CLEO has obtained the ratio by comparing multiplicity in $\Upsilon \to gg\gamma$ and $e^+e^- \to q\bar{q}$ events [49]. The multiplicity in this measurement was defined inclusively as a number of charged particles in one hemisphere. The quark sample presented a natural flavor mixture where the fractions of u, d, s, c quarks were approximately the same. The results were reported for the dijet mass in the range 4 GeV $< M_{jj} <$ 7 GeV. The reported ratio was $r = 1.04 \pm 0.02 \pm 0.05$. The energy scale in this measurement was still too low to clearly see the difference between quark and gluon jets. In the earlier work [50], the CLEO collaboration has also reported the results on the charged particle multiplicity in gluon jets at the dijet mass of $M_{jj} = 10.3$ GeV: $2N_g = 9.339 \pm 0.090 \pm 0.045$.

The OPAL collaboration returned to studies of "Y" shape events with the significantly modified method [51]. A new analysis was based on selecting rare events where a gluon jet was recoiling against two almost collinear quark jets. Each such event was divided into two hemispheres by the plane perpendicular to the thrust axis. A gluon and two tagged b-quark jets were required to be in the opposite hemispheres. The multiplicity in a gluon jet was then defined inclusively as all charged particles in a hemisphere. The average gluon jet energy was $E_{jet} = 39.2$ GeV. It is important to note that the jet clustering algorithm was not used to define the gluon jet and

assign particles to it. It was demonstrated in ref. [52] that the properties of gluon jets selected as described above correspond very closely to the properties of gluon jets produced from a color singlet source. The multiplicity in quark jets was defined inclusively as half of the multiplicity in $Z^0 \to hadrons$ event. The events had to pass the light flavor (u, d, s) jet selection criteria. The average energy of quark jets was $E_{jet} = 45.6$ GeV. The multiplicity in quark jets was corrected to account for the difference in energy compared to gluon jets. Purities of both samples ($\sim$80% for gluons, and $\sim$86% for light quarks) and corrections for backgrounds were obtained based on Jetset Monte Carlo simulation. The corresponding results were $N_g = 14.63 \pm 0.38 \pm 0.60$, $N_{uds} = 9.50 \pm 0.04 \pm 0.24$ and $r = N_g/N_{uds} = 1.552 \pm 0.041 \pm 0.060$. The reported energy scale was $Q = 2E_{jet} = 78.4$ GeV.

The next OPAL measurements [53, 54] basically repeated with better statistics the previous analysis [51]. The [53] results were $N_g = 14.32 \pm 0.23 \pm 0.40$, $N_{uds} = 10.10 \pm 0.01 \pm 0.18$, $r = N_g/N_{uds} = 1.471 \pm 0.024 \pm 0.043$, with the corresponding energy scale $Q = 2E_{jet} = 83.6$ GeV. The results obtained in [54] were $N_g = 14.28 \pm 0.18 \pm 0.31$ and $r = N_g/N_{uds} = 1.514 \pm 0.019 \pm 0.034$. The scale was $Q = 2E_{jet} = 80.2$ GeV.

The discussed above CLEO [49, 50] and OPAL [51, 53, 54] measurements are the only model-independent studies of properties of unbiased gluon jets in e^+e^- annihilations at theoretically well defined energy scales. All so far discussed early experimental results on the difference between quark and gluon jets are summarized in Tables 3–1, 3–2 and presented in Fig. 3–1. There are also a few model-dependent and indirect studies of the multiplicity in gluon jets and the ratio $r = N_g/N_q$ performed by OPAL and CDF. These measurements are discussed below.

The OPAL collaboration has recently conducted two measurements of the gluon jet properties. In the first model-dependent study [55], the k_T algorithm was tuned to identify exactly three jets in every event, and only Y-shape events were retained for the analysis. The multiplicity in a gluon jet was extracted from the multiplicity in a

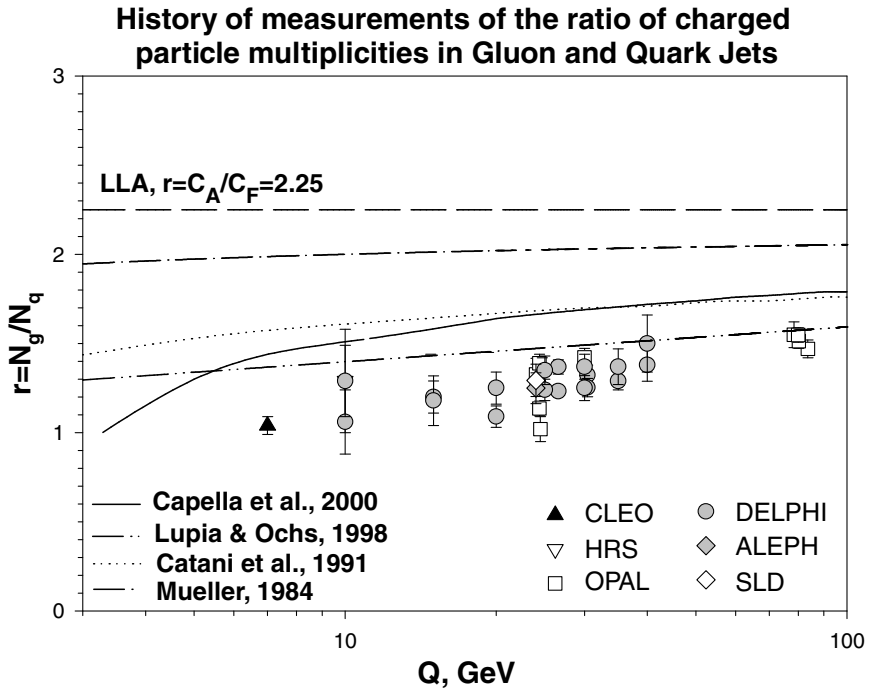

Figure 3–1: History of measurements of the ratio of charged particle multiplicities in gluon and quark jets.

3-jet event by using a theoretical formalism [48] which is valid up to $MLLA$ accuracy. The multiplicity in unbiased quark jets was obtained from the $3NLO$ fit [36] to the inclusive multiplicity in $e^+e^- \to hadrons$ events with removed contribution from c, b-quarks. The reported energy scale was $Q = P_{T,Lu}$. It was shown in ref. [48] that ${P_{T,Lu}}^2$ can be used as an energy scale for unbiased gluon jets from 3-jet events. The results for multiplicity in gluon jets and the ratio, $r = N_{gluon}/N_{uds}$, were reported for the energy scale in the range from Q=11.1 GeV to Q=30.5 GeV. At Q=30 GeV, the reported ratio is $r = 1.422 \pm 0.006 \pm 0.051$.

In the next measurement [56], gluon jets from 3-jet events were studied by applying the so-called jet boost algorithm [57] which was motivated by the color dipole

[2] $P_{T,Lu} = \sqrt{\frac{s_{qg}s_{\bar{q}g}}{s}}$, where s_{ij} is the invariant mass of i, j jets. The kinematic limit for this scale is $P_{T,Lu} < s/2$.

Table 3–1: The summary of model-independent measurements of the difference between quark and gluon jets conducted on e^+e^- machines. The results are obtained using biased gluon jets. Therefore, they can not be directly compared to theory or CDF results.

Experiment	Hardness, Q	N_{gluon}	N_{quark}	ratio
HRS[38]	$E_{jet}\simeq$10 GeV	-	-	$1.29^{+0.29}_{-0.46}$
OPAL[39]	$E_{jet}\simeq$24 GeV	-	-	1.02±0.04(stat.)
OPAL[40]	$E_{jet}\simeq$24 GeV	9.10±0.10	$N_{NFM}=$ 6.86±0.09	$N_g/N_{NFM}=$ 1.326±0.054±0.073
SLD[42]	$\langle E_{jet}\rangle\simeq$24 GeV	-	-	$N_g/N_{uds}=$ $1.294\pm0.064^{+0.047}_{-0.064}$
OPAL[43]			$N_{NFM}=$	$N_g/N_{NFM}=$
k_T-based	E_{jet}=24.39 GeV	9.10±0.07±0.09	7.27±0.07±0.08	1.251±0.024±0.029
Cone-based	E_{jet}=24.40 GeV	6.26±0.06±0.07	5.71±0.05±0.05	1.096±0.023±0.023
OPAL[44]			$N_{uds}=$	$N_g/N_{uds}=$
k_T-based	E_{jet}=24.38 GeV	9.16±0.07±0.12	6.59±0.06±0.10	1.390±0.038±0.032
Cone-based	E_{jet}=24.38 GeV	6.18±0.06±0.13	5.44±0.05±0.04	1.135±0.031±0.029
ALEPH[45]			$N_{uds}=$	$N_g/N_{uds}=$
	E_{jet}=24 GeV	9.90±0.10±0.27	7.90±0.44±0.26	1.249±0.084±0.022
			$N_{NFM}=$	$N_g/N_{NFM}=$
			8.286±0.09±0.22	1.194±0.027±0.019
DELPHI[46]			$N_{udscb}=$	$N_g/N_{udscb}=$
k_T-based	E_{jet}=10.0 GeV	5.78±0.06	5.43±0.90	1.06±0.18
k_T-based	E_{jet}=15.0 GeV	6.64±0.09	5.54±0.43	1.20±0.09
k_T-based	E_{jet}=20.0 GeV	8.18±0.17	7.52±0.36	1.09±0.06
k_T-based	E_{jet}=25.0 GeV	9.13±0.14	7.38±0.33	1.24±0.06
k_T-based	E_{jet}=30.0 GeV	9.83±0.30	7.89±0.35	1.25±0.07
k_T-based	E_{jet}=35.0 GeV	10.67±0.33	8.24±0.17	1.29±0.05
k_T-based	E_{jet}=40.0 GeV	11.86±0.68	8.61±0.20	1.38±0.09
k_T-based	$\langle E_{jet}\rangle$=26.6 GeV	-	-	1.232±0.022±0.018
Jade-based	E_{jet}=10.0 GeV	7.04±0.10	5.44±0.85	1.29±0.20
Jade-based	E_{jet}=15.0 GeV	7.95±0.14	6.73±0.81	1.18±0.14
Jade-based	E_{jet}=20.0 GeV	9.35±0.19	7.46±0.53	1.25±0.09
Jade-based	E_{jet}=25.0 GeV	10.16±0.43	7.50±0.33	1.35±0.06
Jade-based	E_{jet}=30.0 GeV	11.18±0.47	8.19±0.19	1.37±0.07
Jade-based	E_{jet}=35.0 GeV	11.27±0.74	8.20±0.23	1.37±0.10
Jade-based	E_{jet}=40.0 GeV	12.61±1.32	8.41±0.16	1.50±0.16
Jade-based	$\langle E_{jet}\rangle$=26.6 GeV	-	-	1.369±0.019±0.035
				$N_g/N_{uds}=$
k_T-based	E_{jet}=24.2 GeV	-	-	1.279±0.021±0.020
k_T-based	E_{jet}=30.4 GeV	-	-	1.323±0.053±0.020
k_T-based	E_{jet}=30.4 GeV	-	-	$N_g/N_{NFM}=$ 1.253±0.028±0.044

model of QCD [58]. According to this technique, the color charge of the gluon in $e^+e^- \to q\bar{q}g$ events can be decomposed into two parts: one equal and opposite to the color charge of the quark and the other equal and opposite to the color charge of the antiquark. Therefore, a $e^+e^- \to q\bar{q}g$ event consists of two independent dipoles. For symmetric 3-jet events, each dipole can be independently boosted to a back-to-back frame where the dipoles can be combined to yield an event with the color structure of a gg event from a color singlet. In this measurement, the symmetric Y-shape events were selected by adjusting the resolution of the k_T algorithm to identify exactly three jets in every event. The results on multiplicity in unbiased gluon were obtained for the energy scale, $Q = 2E^*_{jet} = 2E_{jet}\ sin(\vartheta/2)$ (ϑ is the angle between two lower energy jets), in the range from 10.5 GeV to 35.4 GeV. To obtain the results on ratio $r = N_{gluon}/N_{uds}$, the multiplicity in gluon jets was compared to the multiplicity in unbiased quark jets measured in other e^+e^- experiments. The reported ratio was $r \sim 1.2 - 1.5$ for $Q \sim$ 10.5-35.4 GeV. Despite the fact that properties of gluon jets in this analysis were not directly determined by using any theoretical formalism, the measurement still cannot be considered as direct because 3-jet events resembling the structure of gg events at specific energy scale were used rather than well defined gluon jets. Moreover, the ratio was obtained by comparing jets from different event topologies: gluons from 3-jet events and quarks from 2-jet events.

The CDF collaboration has also obtained results on the ratio $r = N_g/N_q$ in two model-dependent analyses of jets from dijet events. Both measurements were performed for events in a wide range of dijet invariant masses, 72 GeV $< M_{jj} <$ 740 GeV. The analyses were done in the dijet center-of-mass frame, and charged particles were counted in small cones around the jet directions ($\theta_c < 0.47$ rad). In the first measurement [59], the ratio was extracted from the $MLLA$ fits of the mean multiplicity evolution with the energy scale. The ratio was found to be r=1.7$\pm$0.3. In the other analysis [60], the ratio was obtained by considering the evolution of the

Table 3–2: The summary of model-independent measurements of the difference between quark and gluon jets conducted at e^+e^- machines using unbiased gluon jets. These results can be directly compared to theory or CDF data.

Experiment	Hardness, Q	N_{gluon}	N_{quark}	ratio
CLEO[49]	4 GeV$<M_{jj}<$7 GeV	-	-	$N_g/N_{udsc}=$
		$2N_g=$		1.04±0.02±0.05
	M_{jj}=4.5 GeV	4.88±0.10(stat.)	-	-
	M_{jj}=5.5 GeV	5.28±0.10(stat.)	-	-
	M_{jj}=6.5 GeV	5.65±0.12(stat.)	-	-
CLEO[50]	M_{jj}=10.3 GeV	$2N_g=$	-	-
		9.339±0.090±0.045	-	-
OPAL[51]			$N_{uds}=$	$N_g/N_{uds}=$
	$2E_{jet}$=78.4 GeV	14.63±0.38±0.60	9.50±0.04±0.24	1.552±0.041±0.060
OPAL[53]	$2E_{jet}$=83.6 GeV	14.32±0.23±0.40	10.10±0.01±0.18	1.471±0.024±0.043
OPAL[54]	$2E_{jet}$=80.2 GeV	14.28±0.18±0.31	-	1.514±0.019±0.034

charged particle momentum spectra with the energy scale. The ratio reported in this analysis was r=1.9±0.5.

The results of the last four measurements discussed above are summarized in the Table 3–3.

3.3 Feasibility of Quark and Gluon Jet Studies at CDF

The major advantage of studying differences between quark and gluon jets in $p\bar{p}$ collisions as compared to e^+e^- annihilations is that gluon jets are produced on equal footing with quark jets. Therefore, there is no need to look for peculiar 3-jet events to obtain a sample of gluon jets. Moreover, different rates of production of gluon jets in different subprocesses with similar event topology can be used to statistically separate quarks from gluons. For instance, one can use for an analysis jets from dijet and γ+jet or Z+jet events (compared to Z+jet sample, γ+jet events are more contaminated by background, but they have an advantage of much higher production rate).

In order to compare theory predictions with data from hadron collisions, the analysis has to be performed in the center-of-mass frame of the dijet (or γ/Z+jet) system where jets (or γ/Z and jet) are back-to-back. Theory also prescribes that

Table 3–3: The summary of model-dependent and indirect measurements of the difference between gluon jets and light flavor, $u-, d-, s-$, quark jets.

Experiment	Hardness, Q	$2N_g$	$r = N_g/N_q$
OPAL[55]	$Q = P_{T,Lu}$=30 GeV		1.422±0.006±0.051
	11.1 GeV	10.6±0.2±1.8	1.31±0.03±0.22
	12.6 GeV	11.0±0.3±1.7	1.29±0.03±0.20
	14.1 GeV	11.2±0.3±1.7	1.25±0.03±0.19
	15.5 GeV	13.0±0.3±1.9	1.39±0.04±0.20
	17.0 GeV	13.2±0.4±1.8	1.35±0.04±0.19
	18.4 GeV	13.3±0.4±1.7	1.31±0.04±0.17
	19.9 GeV	14.4±0.5±1.2	1.38±0.05±0.12
	21.4 GeV	14.5±0.5±1.1	1.344±0.046±0.098
	22.9 GeV	15.00±0.52±0.87	1.353±0.047±0.079
	24.0 GeV	15.53±0.57±0.94	1.371±0.050±0.083
	25.4 GeV	15.8±0.6±1.5	1.36±0.05±0.13
	26.7 GeV	15.9±0.6±1.9	1.34±0.05±0.16
	27.9 GeV	16.5±0.7±2.5	1.37±0.06±0.21
	28.7 GeV	17.9±0.7±2.0	1.46±0.06±0.16
	29.6 GeV	17.6±0.7±2.3	1.42±0.06±0.18
	30.2 GeV	19.1±0.7±1.6	1.53±0.06±0.13
	30.5 GeV	18.2±0.7±1.9	1.45±0.06±0.15
OPAL[56]	$Q = 2E^*_{jet} = 2E_{jet}\ sin(\vartheta/2) =$		
	∼10.5–35.44 GeV	-	r ∼1.3–1.5
	10.50 GeV	9.606±0.060±0.094	-
	11.96 GeV	10.380±0.060±0.124	-
	13.96 GeV	11.354±0.060±0.148	-
	16.86 GeV	12.582±0.060±0.180	-
	21.84 GeV	14.756±0.124±0.154	-
	28.48 GeV	17.24±0.26±0.20	-
	35.44 GeV	19.04±0.60±0.66	-
CDF[59]	72 GeV< M_{jj} <740 GeV	-	1.7±0.3
CDF[60]	72 GeV< M_{jj} <740 GeV	-	1.9±0.5

particles have to be counted in small cones, θ_c, around the jet directions (pQCD calculations are valid for $\theta_c \ll 1$). This, in fact, helps to avoid an ambiguity in assigning particles to jets (one of the major problems of early e^+e^- measurements).

Despite all the advantages of studying quark and gluon jets at a hadron collider such as the Tevatron, there are also factors complicating the analysis. Unlike to e^+e^- annihilations, the hard scattering in $p\bar{p}$ collisions is always accompanied by interactions of proton and anti-proton remnants (the underlying event) whose contribution has to be properly subtracted. There is also initial state radiation (ISR) from incoming partons and color connection between initial and final jets. To reduce the influence of these effects on measurements, central (at large angles with respect to beam direction) jets have to be selected for the analysis. The presence of multiple interactions in the same bunch crossing (secondary events are often referred as "pile-up") also has to be accounted for. Finally, jet energy measurement in $p\bar{p}$ collisions is more complicated because a part of the total energy (associated with the underlying event) always escapes the detector (in e^+e^- annihilations, the total energy that would be deposited in the calorimeter is known a priori).

3.4 Analysis Strategy at CDF

The CDF analysis on fragmentation of quark and gluon jets is largely independent of theoretical models of fragmentation. This independence is achieved by exploiting the difference in quark and gluon jet content of dijet events and γ+jet events in $p\bar{p}$ collisions. Dijet events have large gluon content because the gluon component in the proton (or anti-proton) is dominant at relatively small $x_T = 2E_T/\sqrt{s}$. In γ+jet events, the jet is usually originating from a quark. This difference in gluon jet content allows for distinguishing and measuring the properties of gluon and quark jets on statistical basis. Thus, we do not have to discriminate between quark and gluon jets when selecting events.

The average charged particle multiplicities per jet in, $N_{\gamma j}$ and N_{jj}, γ+jet and dijet data samples, respectively, can be expressed as functions of the multiplicities in gluon and quark jets, N_g and N_q:

$$N_{jj} = f_g^{jj} N_g + (1 - f_g^{jj}) N_q, \tag{3.1}$$

$$N_{\gamma j} = f_g^{\gamma j} N_g + (1 - f_g^{\gamma j}) N_q, \tag{3.2}$$

where f_g^{jj} and $f_g^{\gamma j}$ are fractions of gluon jets in dijet and γ+jet events. To take into account possible contamination of γ+jet events by fake photons (discussed in Chapter 8), Eq. 3.2 must be modified as follows:

$$N_{\gamma j} = \delta_\gamma (f_g^{\gamma j} N_g + (1 - f_g^{\gamma j}) N_q) + (1 - \delta_\gamma) N_{fj}, \tag{3.3}$$

where δ_γ is the fraction of real photons among the photon candidates, and N_{fj} is the multiplicity in the jet opposite to the fake photon. Eqs. 3.1, 3.3 allow us to extract the average charged particle multiplicities in gluon and quark jets, N_g and N_q, as well as their ratio, $r = N_g/N_q$:

$$r = \frac{N_g}{N_q} = 1 + \frac{\alpha - \delta_\gamma \times (\alpha - 1) - \frac{N_{\gamma j}}{N_{jj}}}{f_g^{jj} \times \frac{N_{\gamma j}}{N_{jj}} - \delta_\gamma \times f_g^{\gamma j} - (1 - \delta_\gamma) \times f_g^{jj} \times \alpha} \tag{3.4}$$

$$N_g = \frac{r N_{jj}}{f_g^{jj}(r - 1) + 1}, \tag{3.5}$$

$$N_q = \frac{N_{jj}}{f_g^{jj}(r - 1) + 1}, \tag{3.6}$$

where we introduced $\alpha = N_{fj}/N_{jj}$, to account for possible differences between a jet from a regular dijet event and a jet opposite to a fake photon.

In summary, we can measure the average charged particle multiplicities in gluon and quark jets, N_g and N_q, as well as their ratio, $r = N_g/N_q$, by directly measuring or

evaluating the following six independent parameters: multiplicity per jet in dijet and γ+jet events, N_{jj} and $N_{\gamma j}$; fraction of gluon jets in dijet and γ+jet events, f_g^{jj} and $f_g^{\gamma j}$; purity of the γ+jet sample, δ_γ; ratio of multiplicities in a jet from a regular dijet event and a jet opposite to a fake photon, α. These measurements will be described in Chapter 8.

CHAPTER 4
ACCELERATOR AND DETECTOR

The Fermi National Accelerator Laboratory (FNAL, Fermilab) is the leading facility in the experimental particle physics. Fermilab is the home of a hadron collider called the Tevatron. The Tevatron is the worlds most powerful accelerator. It was the site of the bottom and the top quark discoveries. There is a chance we can even witness a discovery of the long-hypothesized Higgs boson during the Run 2 of the Tevatron.

The Collider Detector at Fermilab (CDF) is one of the two (the other one is D0) multipurpose detectors built at collision points of the Tevatron. The analysis presented in this dissertation is based on the data sample collected by CDF during the 1993–1995 running period of the Tevatron.

4.1 Tevatron during the 1993–1995 Running Period

The Fermilab accelerator complex is shown on a schematic drawing on Fig. 4–1.

The $p\bar{p}$ collisions at the center-of-mass energy of 1.8 TeV were produced by a sequence of five individual accelerators. First, a Cocroft-Walton accelerator boosted negative hydrogen ions to 750 KeV energy. Then, the ions were directed to the second stage of the process provided by the Linac. The Linac is a 145 m long, two-stage linear accelerator that further increased the energy of ions up to 401.5 MeV. To produce the protons before the next stage, the ions were stripped of their electrons by passing through a carbon foil. Protons leaving the Linac entered the Booster. The Booster is a synchrotron accelerator of about 150 m in diameter. It was used to accelerate protons up to 8 GeV. Next, protons were injected into another circular accelerator called the Main Ring. The Main Ring is a 1 km radius machine which consists of a total of 774 dipole and 240 quadrupole superconducting magnets used to keep protons

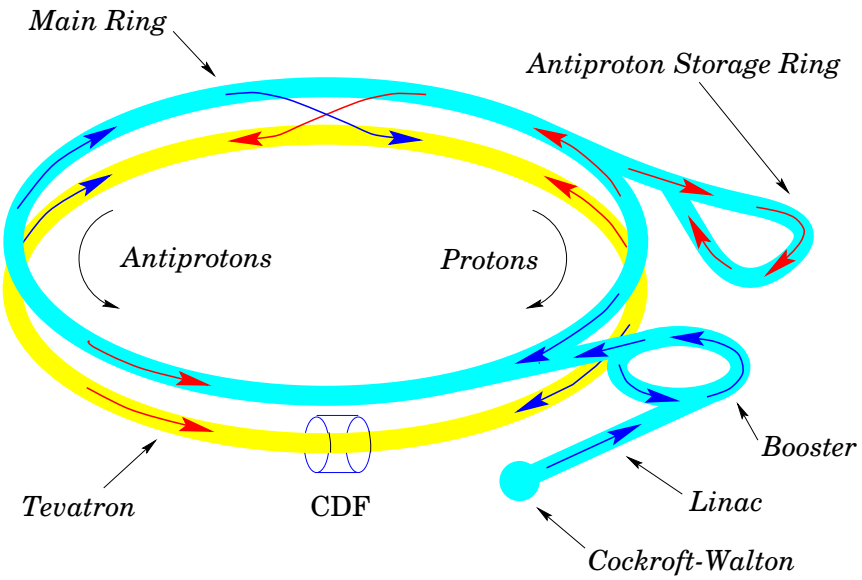

Figure 4–1: Overview of the Fermilab accelerator complex. The $p\bar{p}$ collisions at the center-of-mass energy of 1.8 TeV are produced by a sequence of five individual accelerators: the Cockroft-Walton, Linac, Booster, Main Ring, and Tevatron.

in a stable circular orbit. The Main Ring served two functions. It provided a source of 120 GeV protons which were used to produce anti-protons and boosted protons and anti-protons up to 150 GeV before injecting them into the Tevatron.

In order to produce anti-protons, protons of 120 GeV energy were transported from the Main Ring to a tungsten target. The produced sprays of secondary particles contained anti-protons. Those anti-protons were selected and stored into the Debuncher ring where they were stochastically cooled to reduce the momentum spread. At the end of this process, the anti-protons were stored in an Accumulator, until they were needed in the Tevatron. The Tevatron is located 65 cm below the Main Ring in the same tunnel. It is a synchrotron accelerator that uses a total of 774 dipole and 216 quadrupole superconducting magnets cooled down to 4.6 K by liquid helium.

Finally, 150 GeV protons and anti-protons were injected into the Tevatron where they were simultaneously accelerated to 900 GeV. Therefore, the center-of-mass energy of colliding beams was 1.8 TeV. The Tevatron counter-circulated six bunches of protons and anti-protons which were collided every 3.5 μs. The proton bunches

contained approximately 2×10^{11} protons, and the anti-proton bunches had 2-9$\times10^{10}$ anti-protons. During the Run 1B, the collision volume was approximately circular in the $x-y$ plane with an average radius of 25 μm and had a Gaussian distribution with a sigma of 30 cm in z direction.

The instantaneous luminosity of the Tevatron is given by

$$\mathcal{L}_{inst} = \frac{N_p N_{\bar{p}} f}{\mathcal{A}} \tag{4.1}$$

where N_p and $N_{\bar{p}}$ are the numbers of protons and anti-protons per bunch, f is the frequency of bunch crossings and $\mathcal{A}$ is the effective area of the crossing beams. For the Run 1B, the average initial luminosity was $\mathcal{L}_{inst}$ $\sim$1.6$\times10^{31}$ cm^{2}s^{-1}. The instantaneous luminosity exponentially decreases with time due to transverse spreading of the beam and losses of protons and anti-protons from collisions. The period of time when the same proton and anti-proton bunches continue to collide is called a store. The typical store duration during the Run 1B was about 8–18 hours. The luminosity decreases by approximately an order of magnitude during the lifetime of a store.

4.2 CDF Design and Overview

The CDF is a multipurpose collider detector located at one of the two colliding beam interaction points. It is designed to study a wide range of processes occurring in $p\bar{p}$ collisions. The CDF allows to observe and measure the properties of jets, photons, electrons, muons and charged hadrons.

A schematic drawing of the CDF detector can be found on Fig. 4–2. The CDF is approximately cylindrically symmetric about the beam direction. It is about 10 m high, extends about 27 m from end to end, and weighs over 5000 ton. The CDF uses a right-handed Cartesian coordinate system with its origin in the nominal interaction point (center of the detector). The positive z-axis points in the proton beam direction, positive y-axis points vertically upward, and the positive x-axis points toward the center of the Tevatron ring. The azimuthal angle ϕ is measured around the beam

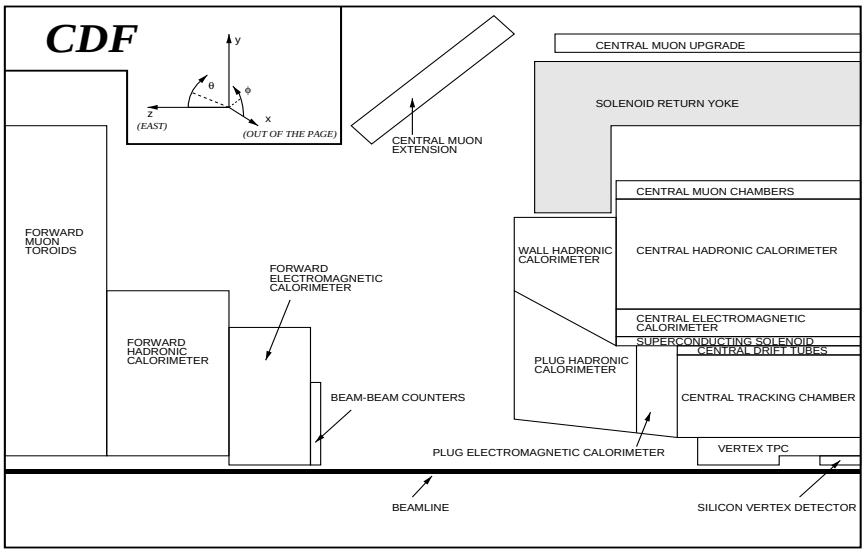

Figure 4–2: Drawing of the CDF detector. One quarter view.

axis from the positive x-axis. The polar angle θ is defined as the angle measured from the positive z-axis. It is more often that the pseudo-rapidity, $\eta = -\ln(\tan(\theta/2))$, is used in place of the polar angle. The pseudo-rapidity can be defined with respect to the actual position of the interaction vertex (event η) and with respect to the center of the detector (detector η_d)

The major components of the CDF detector are listed below:

- Silicon Vertex Detector (SVX). The SVX was designed for precise measurement of the position of the interaction vertex in the $r - \phi$ plane.
- Vertex Time Projection Chamber (VTX). It measures the z-position of the interaction vertex.
- Central Tracking Chamber (CTC). The CTC provides measurements of momentum and spatial parameters of particle's trajectories (tracks) in the magnetic field (B=1.4 T).
- Calorimetry (central, plug and forward calorimeters). Two types of calorimeters, electromagnetic (EM) and hadronic (HA), are used to measure the energy of photons, electrons and jets of particles.

- Central Preradiator detector (CPR) and Central Electromagnetic Strip Chamber (CES). The CPR and CES are important components of the photon and electron identification.
- Muon System (made of layers of drift chambers and scintillators). The Muon System is positioned (partially) behind a special protective steel wall, which absorbs all particles that may escape the calorimeter except for muons.
- Beam-Beam Counters (BBC). The BBC provides measurement of the instantaneous luminosity.

The CDF detector is described in ref. [61] and references therein. In the rest of this chapter we will discuss in more details the sub-detectors directly related to this analysis.

4.2.1 Vertex Detectors (VTX and SVX)

The Silicon Microstrip Detector (SVX) surrounds the beryllium beam pipe. The SVX is about 60 cm long and covers the radial region from 3.0 cm to 7.9 cm. It consists of 4 layers of silicon strips parallel to the beam line. The SVX covers $|\eta_d| < 1.0$ region and has acceptance of $\sim$60% in this range. Its single hit resolution in the transverse plane is $\sim$10 μm. The SVX is a part of the tracking system along with VTX and CTC. It provides a very precise measurement of the transverse position of the event vertex.

Directly outside of the SVX is the Vertex Time Projection Chamber (VTX) detector. The VTX is 2.8 m long in z direction and extends from an inner radius 8 cm out to a radius of 22 cm from the beam pipe. It is made of 8 octagonal modules divided into 8 separate wedges. The chambers are filled with a mixture of 50% argon and 50% ethane gases. The VTX provides $r - z$ tracking information which is used to determine the position of the interaction vertex in z direction with the resolution of $\sim$1 mm.

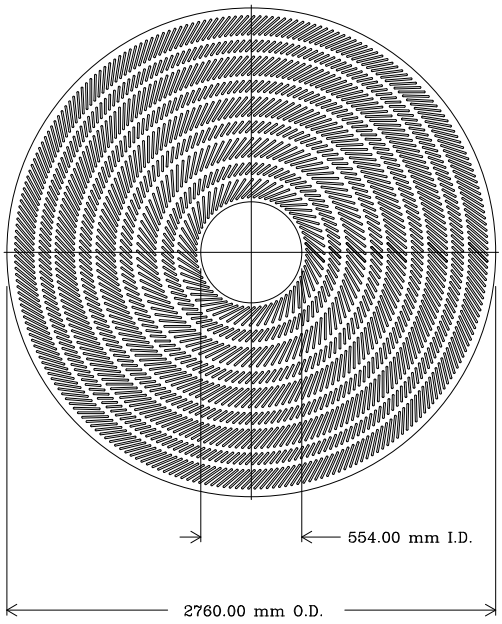

Figure 4–3: The CTC end plate view.

Both SVX and VTX are the critical components of the CDF detector used in many analyses. They allow to precisely determine the primary interaction position as well as to identify events with multiple interactions.

4.2.2 Central Tracking Chamber (CTC)

The Central Tracking Chamber (CTC) extends from a radius of 31 cm up to a radius of 132 cm from the beam pipe. It provides an angular coverage up to $|\eta_d| < 1.5$, however, it is most efficient in the region of $|\eta_d| < 1.0$. The CTC is a gas drift chamber of cylindrical shape. It has 9 super-layers of wires. The super-layers are divided on 5 axial and 4 stereo super-layers. Every axial layer has 12 sense wires arranged along the beam line. The role of axial super-layers is to provide $r - \phi$ information. Each of stereo layers has 6 sense wires which are tilted $\pm 3^o$ with respect to the beam axis. The stereo layers provide $r - z$ information about particle's trajectory. The wires in both stereo and axial layers are arranged in planes which make a 45^o angle with respect to radial direction to compensate for the drift of ions caused by the 1.4 T

Table 4–1: Selected parameters of the CDF Central Tracking Chamber.

Number of sense wires	30,504
Number of layers	84
Number of super-layers	9 (5 axial + 4 stereo)
Drift field	~1350 V/cm
Resolution ($\delta r\phi$)	<200 μm per wire
Efficiency	>98% per hit
Double track resolution	<5 mm or 100 ns
Maximum drift distance	40 mm
Maximum hits per wire	>7
Axial (z) resolution	~4 mm
Momentum resolution	$\delta p_T/p_T \simeq 0.002 \cdot p_T$
R_{min}, R_{max}	31 cm and 132 cm
Magnetic field, B	1.4 T

magnetic field. Fig. 4–3 shows the end plate view of the CTC, and some of the essential parameters of the CTC are summarized in Table 4–1.

The CTC is used to measure the momentum and spatial parameters of particle's trajectory by arranging hits produced by a passing detector particle into segments of hits in same layer and then linking into a full trajectory. The Tracking Algorithm then fits the obtained hits to a helix (particle's trajectory in the magnetic field). The momentum resolution of the CTC alone is better than $\delta p_T/p_T \simeq 0.002 \cdot p_T$. The resolution improves if the information from VTX, SVX and CTC is combined.

4.2.3 Preshower and Shower Maximum Detectors, Calorimetry

The Central Preradiator Detector (CPR) is positioned between the superconducting solenoid and the central calorimeter. The solenoid serves as a radiator that converts ~60% of the photons into electron-positron showers that are detected in the CPR. The CPR is an array of 24 multi-wire proportional chambers (one per azimuthal wedge of the central calorimeter). Each chamber is a rectangular cell 37.3 cm wide (15^o in ϕ) and 2.86 cm high that contains 32 sense wires. The sense wires are read out in pairs, thus providing an effective spatial resolution of 1.11 cm in $r-\phi$ view

(or 0.0065 radians in ϕ). There are four CPR cylinders of 124 cm long which cover the region between z=-248 cm and z=248 cm (or $|\eta_d| < 1.0$ angular region).

The Central Electromagnetic Strip chamber (CES) is located in the central electromagnetic calorimeter at depth of about 5.9 radiation lengths which corresponds to the point where maximum electromagnetic shower development occurs. The CES determines the shower position and transverse shower development by measuring the charge deposited on orthogonal strips and wires. Cathode strips are arranged in the azimuthal direction providing z-view information, while anode wires are arranged in the z direction providing the $r - \phi$ view information. The CES is located 184 cm from the beam line. There are 24 strip chambers corresponding to each wedge of the calorimeter. There are two strip and wire sections per wedge. The devision between sections is located at $|z|$=121.2 cm. In the first section, there are 69 strips of 1.67 cm wide which fill the region between 6.2 and 121.2 cm. In the second section, there are 59 strips of 2.01 cm wide which fill the region between 121.2 and 239.6 cm. There are also 62 wire cells in each half section. The segmentation of the CES detector provides a shower position resolution of $\sim$2 mm in each direction for 50 GeV electrons.

The CPR and CES detectors are the most important elements in the photon identification. The information from these detectors is used to suppress the neutral meson background as well as to determine the purity of the photon sample. The measurement of the fraction of real photons among the photon candidates is based on evaluating the γ-conversion probability in the CPR. It also uses the transverse profile of the electromagnetic shower measured by the CES detector.

The CDF calorimetry contains seven calorimeter systems: CEM (Central Electromagnetic), PEM (Plug Electromagnetic), FEM (Forward Electromagnetic),CHA (Central Hadronic), WHA (Wall Hadronic), PHA (Plug Hadronic) and FHA (Forward Hadronic). The CDF calorimeter system provides full 2π azimuthal coverage, and it extends up to 4.2 in pseudo-rapidity. The segmentation and rapidity coverage

of each of the calorimeter components are given in Table 4–2. We will further consider in more details the CEM, CHA and WHA calorimeters because they are directly used in this analysis.

The CDF calorimeter system has a projective geometry, i.e. all towers point to the center of the detector. Each tower of the center calorimeter has a few alternating layers of absorber (lead in CEM and iron in CHA and WHA) and active (polystyrene scintillator in CEM and acrylic scintillator in CHA and WHA) media. When a particle passes through the dense absorber media it interacts with its material loosing some energy and producing a shower of secondary particles. Then, secondary particles interact with the active media and produce light which is collected and converted into the energy measurement. The electromagnetic shower develops spatially faster than hadronic shower, therefore the electromagnetic calorimeter is positioned closer to the interaction point. The CEM extends from the radius of 173 cm up to 208 cm from the beam line. A total thickness of the CEM material is equivalent to about 18 radiation lengths. The CHA is located right after the CEM. Both CHA and WHA have a total material depth of about 4.5 interaction lengths. The energy resolution of the CEM for electrons (and photons) between 10 and 100 GeV is

$$\frac{\sigma(E)}{E} = \frac{13.5\%}{\sqrt{E_T}} \oplus 1.7\% \quad (CEM), \tag{4.2}$$

where E_T is the transverse energy of the electron (photon), and the symbol $\oplus$ indicates that two independent terms are added in quadrature. The energy resolution of the CHA and WHA for charged pions between 10 and 150 GeV is

$$\begin{aligned} \frac{\sigma(E)}{E} &= \frac{50\%}{\sqrt{E_T}} \oplus 3\% \quad (CHA), \\ \frac{\sigma(E)}{E} &= \frac{75\%}{\sqrt{E_T}} \oplus 4\% \quad (WHA), \end{aligned} \tag{4.3}$$

respectively. The initial calibration of the electromagnetic and hadronic calorimeters was performed with 50 GeV electrons and charged pions during the test beam.

Table 4–2: The CDF Calorimeter System coverage and detector segmentation.

	Detector	Pseudorapidity, $\lvert\eta_d\rvert$	$\eta_d - \phi$ segmentation
Central Calorimeter	CEM	0.0-1.1	0.11×15^o
	CHA	0.0-0.9	0.1×15^o
	WHA	0.7-1.3	0.11×15^o
Forward Calorimeter	PEM	1.1-2.4	0.09×5^o
	PHA	1.3-2.4	0.09×5^o
	FEM	2.2-4.2	0.1×5^o
	FEM	2.3-4.2	0.1×5^o

In this analysis the calorimeter was used to determine the momentum and direction of photons and jets.

4.3 CDF Trigger System

The inelastic $p\bar{p}$ cross section at $\sqrt{s} = 1.8$ TeV is about 50 mb ($\sim 50 \times 10^{-27}$ cm^2). For a typical instantaneous luminosity $\mathcal{L}_{inst} = 1.6 \times 10^{31}$ cm^{-2}/s we have about 800,000 inelastic collisions per second at CDF. The CDF readout electronics and event storage system are not physically capable to write events at such a high rate (CDF Run 1 storage media can write a few events per second). Moreover, most of these events do not present a significant interest for the CDF physics program. Another concern for the data acquisition system (DAQ) is to minimize the dead-time that occurs when a particular event is being read out of the detector electronics and processed. To reduce the readout rate and effectively process only events interesting in terms of physics, the CDF developed a sophisticated on-line three-level (Level 1, Level 2 and Level 3) trigger system [62]. Each next trigger level examines fewer events but in greater details. The Level 1 and Level 2 triggers present fast hardware implemented algorithms, while the Level 3 trigger is implemented in software running on the commercial computers. The individual trigger path can be prescaled which means only a fraction of events satisfying the trigger requirements is accepted. It is done to keep the trigger rates manageable and still have data samples for wide variety of processes.

The CDF Level 1 trigger examines every bunch crossing and makes a trigger decision within 3.5 μs between bunch crossings, thus it has no dead-time. The Level 1 uses the information about energy of calorimeter towers or hits in the muon system. It reduces the rate from $\sim$280 kHz down to 1 kHz.

The Level 2 trigger requires about 25-35 μs to process an event arrived from the Level 1 trigger and can incur dead-time of a few percent. The Level 2 output rate is limited to about 40–45 Hz. The Level 2 algorithm uses the information about high momentum tracks and clustered calorimeter energy. If the *accept* decision is made by the trigger, then the information from all subsystems is read out and passed on Level 3.

The Level 3 trigger consists of on-line software filters based on simplified versions of the offline reconstruction code. All events which pass the Level 3 trigger are written on disk or tape with a typical output rate of 8 Hz.

CHAPTER 5
JETS AT CDF

Jets at CDF are defined using a cone clustering algorithm based on the Snowmass convention [63]. Jets are reconstructed using calorimeter energies and the position of the primary vertex. The jet algorithm is implemented in the standard CDF routine JETCLU. The clustering is done in three steps: preclustering, clustering, and merging. A set of corrections is applied to raw jet energies in the cone to compensate for detector and physics effects.

Jet reconstruction begins by creating a list of calorimeter towers with $E_T \geq$ 1 GeV which are called seed towers. The seeds are stored in order of decreasing E_T. Preclusters are formed by combining seed towers within a cone of radius $R = \sqrt{(\Delta\phi)^2 + (\Delta\eta)^2}$ in η-ϕ space. A seed tower is added to the precluster if it is within a radius R from a seed tower which is already assigned to the precluster. Jets are typically clustered using three cone sizes R=0.4, 0.7, and 1.0. In this analysis, jets are defined using the radius R=0.7 (standard for many QCD analyses at CDF).

The jet clustering is performed using the E_T weighted centroid of a precluster (η_c, ϕ_c):

$$\eta_c = \frac{\sum_{i=1}^{n} E_T^i \eta^i}{\sum_{i=1}^{n} E_T^i} \qquad (5.1)$$
$$\phi_c = \frac{\sum_{i=1}^{n} E_T^i \phi^i}{\sum_{i=1}^{n} E_T^i},$$

where the sums are carried out over all seed towers in the precluster. The tower centroid (η^i, ϕ^i) is obtained by

$$\eta_i = \frac{E_{T,i}^{EM}\eta_i^{EM} + E_{T,i}^{HA}\eta_i^{HA}}{E_T^i} \qquad (5.2)$$
$$\phi_i = \frac{E_{T,i}^{EM}\phi_i^{EM} + E_{T,i}^{HA}\phi_i^{HA}}{E_T^i},$$

where $E_{T,i}^{EM}$ and $E_{T,i}^{HA}$ are transverse energies deposited in the electromagnetic and (EM) and hadronic (HA) parts of the i^{th} calorimeter tower, $(\eta_i^{EM}, \phi_i^{EM})$ and $(\eta_i^{HA}, \phi_i^{HA})$ are the centroids of the electromagnetic and hadronic components of the tower calculated with respect to the event vertex (not the same as the geometric center of the CDF detector).

A cone of radius R is formed around the centroid of a precluster. All towers with $E_T \geq 100$ MeV are merged to form a cluster if their centroids are within the cone. A new cluster centroid is re-calculated using all the towers within the cone, and a new cone is formed. The process continues until the cone centroid becomes stable. This procedure is repeated for all preclusters.

After the clustering stage, there can be some towers which are shared by two or more clusters. If one cluster is entirely within the other one, then the smaller cluster is dropped. If two clusters partially overlap, an overlap fraction is calculated by summing the E_T of shared towers and dividing the sum by E_T of the smaller cluster. The two clusters are merged if this fraction is above 0.75. If the fraction is less than 0.75, the clusters are kept unchanged and the towers are assigned to the nearest cluster in η-ϕ space. After all the towers are uniquely assigned to clusters, the clustering and merging procedures are repeated until all clusters remain stable.

After all jets are reconstructed, a set of corrections [64] is applied to the raw jet energy in the cone: to compensate for the non-linearity and non-uniformity of the energy response of the calorimeter; to subtract the energy deposited in the jet cone by sources other than the initial parton (underlying event, multiple interactions etc.);

and to add the energy radiated by the initial parton out of the jet cone (out-of-cone correction).

CHAPTER 6
PHOTONS AT CDF

Photon identification at CDF is based on three basic properties of prompt photons originating from hard scattering. The prompt photons are expected to be observed as localized and isolated deposits of electromagnetic energy in the calorimeter with no high momentum charged tracks associated with them. The last statement is not always true, however. A photon can convert into an electron-positron pair prior to entering the tracking chamber, or it can accidentally overlap with a track from the underlying event. Nonetheless, this is one of the basic criteria which allows to distinguish a photon from an electron.

The photon identification and reconstruction is based on information from the calorimeter, shower max detector (CES), and tracking chamber (COT). The energy and direction of the photon are calculated with respect to the event vertex.

The offline photon reconstruction begins by selecting the clusters of one to three towers adjacent in η (electromagnetic showers are usually contained in one tower with small leakage into neighboring towers). These clusters are required to carry at least 5 GeV of total energy and have less than 12.5% of this energy observed in the hadronic calorimeter (energetic electromagnetic objects can loose a small fraction of their energy in the hadronic portion of the calorimeter due to a late development of the shower).

The selected electromagnetic clusters are required to be isolated. That is, extra transverse energy (other than candidate energy) in calorimeter towers within a cone of radius R=0.4 around the candidate has to be below a certain threshold (usually 1 GeV in most of the CDF analyses involving photons). This requirement helps to suppress photons due to bremsstrahlung from an initial or final state quarks. These

photons tend to be collinear with the quark, and therefore the jet, and usually accompanied by other debris from jet fragmentation. This requirement also helps to reduce contamination due to background photons from energetic π^0's and η's produced during jet fragmentation.

The photon candidates are required to have no high momentum tracks pointing to the electromagnetic cluster. This requirement is primarily used to distinguish between photons and electrons.

The position (i.e. direction) of the photon candidate is determined based on the location of the shower maximum as it is measured by the CES chamber. The additional requirements on the shape of the electromagnetic shower and presence of other CES clusters can be applied to further reduce the multi-meson backgrounds. The CES shower profile, χ^2, is usually required to be consistent with that of a single photon. The quantity χ^2 is defined by the following equation [65]:

$$\chi^2 = \frac{\chi^2_W + \chi^2_S}{2} \tag{6.1}$$

where the individual contributions from the strips (wires) $\chi^2_{S(W)}$ are given by

$$\chi^2_{S(W)} = \sum (p_i - y_i)^2/\sigma_i^2, \tag{6.2}$$

$$\sigma_i^2 = 4[0.026^2 + 0.096^2 y_i](10\ GeV/E)^{0.747}.$$

The p_i are measured strip (wire) pulse heights (normalized to a total pulse hight of unity) and y_i are the expected pulse heights. The forms for the y_i and σ_i^2 were determined empirically from test beam data.

CHAPTER 7
ANALYSIS TOOLS

Monte Carlo event generators have become an invaluable tool in high energy physics. They are used for a large variety of tasks which include, but are not limited to, geometrical acceptance estimation, event selection optimization and efficiency estimation, background studies, corrections for detector effects, etc.

The Monte Carlo event generators incorporate certain theoretical models and allow to simulate a wide range of physics processes. Given a set of initial conditions for a specific process, they return a list of final particles and their momenta. In practice, the data obtained in real measurements always suffers from detector inefficiencies and resolution effects. As a result, a fraction of particles can be lost altogether while those particles which are detected can be reconstructed with distorted parameters. To reproduce these detector effects, the output of the event generator is passed through a detector simulation program which converts the generated particles into a set of observable in the detector quantities.

In order to simulate a specific hard scattering process $ab \to cd$ (e.g., $q\bar{q} \to \gamma g$) in $p\bar{p}$ collisions, the Monte Carlo generator has to use the information about densities of partons a and b inside of a proton and anti-proton. This information is provided in the form of Parton Distribution Functions (PDF's). Two partons which take part in the hard scattering will each carry some fraction x_a and x_b of the initial proton and anti-proton momenta. The square of the center-of-mass energy in the hard scattering process, $\hat{s}$, is related to the square of the energy in the proton and anti-proton center-of-mass, s, by $\hat{s} = x_a x_b s$. Finally, the cross section for hard scattering process $ab \to cd$ will depend on scale Q^2 and on the momentum fraction distribution of the partons seen by the probe at this scale, $f(x, Q^2)$.

In this analysis, Herwig 5.6 [30] and Pythia 6.115 [31] Monte Carlo generators are used. For QCD hard scattering, both generators use Leading Order QCD calculations and can be linked to different parton distribution functions. For jet fragmentation, Herwig and Pythia incorporate various color coherence effects and use re-summed Leading Log Approximation calculations. Hadronization in Herwig is done by means of the cluster model while Pythia utilizes the string model. The fragmentation and hadronization models of both generators have been already discussed in details in Section 2.3. Herwig is probably the most advanced generator in terms of handling the color coherence effects. This is the primary reason for choosing Herwig as a baseline Monte Carlo generator in this analysis.

At CDF, the detector simulation is done by a special package called QFL [66]. QFL takes a properly formated list of particles and their parameters from a Monte Carlo event generator and propagates them through the detector. This propagation of particles includes all the appropriate effects such as multiple scattering, decays of short-lived particles, photon conversions and other interactions of particles in the material. QFL also simulates the response of individual detector components to passing particles as well as the geometrical and instrumental inefficiencies.

CHAPTER 8
MEASUREMENTS

This chapter presents a detailed discussion of the measurements. It starts with the description of data samples and event selection cuts followed by the explanation of how all the independent parameters introduced in Section 3.4 are measured. The corrections applied to data are also discussed.

8.1 Data Samples

This analysis is based on events produced in $p\bar{p}$ collisions with center-of-mass energy $\sqrt{s}$=1.8 TeV and recorded by CDF during the 1993-1995 run period (Run 1B). The total integrated luminosity is 95$\pm$7 pb^{-1}.

The dijet sample is accumulated by using the inclusive jet trigger with E_T threshold 20 GeV (Jet20 trigger). The trigger is pre-scaled by 1000. Its detailed description can be found in ref. [67]. There are also Jet50, Jet70 and Jet100 triggers, but events from the corresponding jet samples are not used in the analysis.

The γ+jet sample is collected using the inclusive photon triggers with thresholds of 23 and 50 GeV on E_T. To reduce the contamination from fake photons in the lower energy γ+jet sample, the 23 GeV trigger requires photon isolation, i.e. extra transverse energy (other than candidate energy) in neighboring calorimeter towers around the candidate has to be less than 4 GeV. More detailed information about photon triggers can be found in ref. [68].

8.2 Event Selection Cuts

In this measurement, the jets are defined by a cone algorithm with cone radius $R = \sqrt{(\Delta\phi)^2 + (\Delta\eta)^2} = 0.7$ and the jet energy is corrected to the parton level using the standard JTC96X.CDF routine (also see Chapter 5).

The following cuts are applied in the offline to select the dijet events:

1. Good run required (this means that all the sub-detectors and components of the CDF detector were functioning properly during the entire run).
2. Number of leading jets is 2 (to avoid a bias toward narrow jets, we also allowed for third and fourth extra jets if their raw energies were below 7 GeV because sometimes a single astray track can be identified as a jet).
3. Both leading jets are required to be in the central region, $|\eta_{jet1,2}| < 0.9$. There are three reasons for this: in this region E_T is of the order of E (theoretically motivated), efficient track reconstruction in CTC, and complementary cones can be defined only for jets in the central region (see Section 8.5.b for more information).
4. The jets have to be well balanced: $|\vec{E}_{T_1} + \vec{E}_{T_2}|/(E_{T_1} + E_{T_2}) < 0.15$, which corresponds to about $\pm 2\sigma$ cut to remove events with large missing E_T.
5. Number of good primary vertices is no more than 2 (selecting only single vertex events would have unnecessarily reduced the statistics).
6. The z-position of the primary vertex has to be within $|z_{vx}| < 60$ cm to insure that vertex detectors are fully efficient.
7. For events with two primary interactions, all tracks are associated with vertices by their proximity. The separation between vertices is required to be $|z_{vx1} - z_{vx2}| > 12$ cm (corresponding to $\sim 12\sigma_z$ for tracks) to allow for unambiguous assignment of tracks. The vertex that has the largest ΣP_T of tracks from cones with R=0.7 around the jet directions is taken to be the one associated with the hard collision.

The γ+jet events must pass exactly the same cuts (treating the photon as one of two jets) and satisfy specific photon identification requirements. To identify photons, we used standard PHO94.CDF routine with the following cuts:

1. Cut on the fraction of cluster energy observed in the hadronic calorimeter: $HA/EM_{total} < 0.125$ (this cut is applied in the offline clustering, it suppresses hadron background).
2. Exactly one photon candidate with E_T >20 GeV.
3. To remove events where photon hits near the edge of the calorimeter wedges (and, therefore, its energy is poorly measured or cannot be measured at all), the following fiducial cuts on (x, z)-coordinates of the electromagnetic shower profile center are applied: $|X_{CES}| < 17.5$ cm and 14 cm $< |Z_{CES}| < 217$ cm.
4. Photon isolation cut of 1 GeV on the extra transverse energy in a cone $R = 0.4$ around the photon candidate (to remove fake photon content due to regular jets).
5. No 3D CTC reconstructed tracks pointing to the EM cluster associated with a photon candidate (to remove electrons and further suppress jet associated background).
6. Energy in the second CES cluster in the same wedge as the photon (if present) <1 GeV (to reduce the single and multiple meson background).
7. The electromagnetic transverse shower profile measured by the CES has to be consistent with that of a single photon: $\chi^2_{CES} < 20$.

The selected events are then subdivided into two bins according to invariant mass, which is defined as $M=\sqrt{(E_1+E_2)^2/c^4-(\vec{P}_1+\vec{P}_2)^2/c^2}$, where E_i and $\vec{P}_i$ are the jet or photon energy and momentum and jets are treated as massless objects. The bins have width $\Delta \ln M$=0.3, which is chosen to be greater than the dijet mass spread due to calorimeter resolution, $\frac{\delta M}{M}\simeq$10%. In the lower bin (72-94 GeV/c^2), our sample consists of 3602 dijet and 2526 γ+jet events with an average invariant mass of 82 GeV/c^2. The other bin (94-120 GeV/c^2) has 1768 dijet and 910 γ+jet events with an average invariant mass of 105 GeV/c^2. The choice of invariant mass range, 72 GeV $< M <$ 120 GeV, has two explanations. Dijet events with $M <$ 72

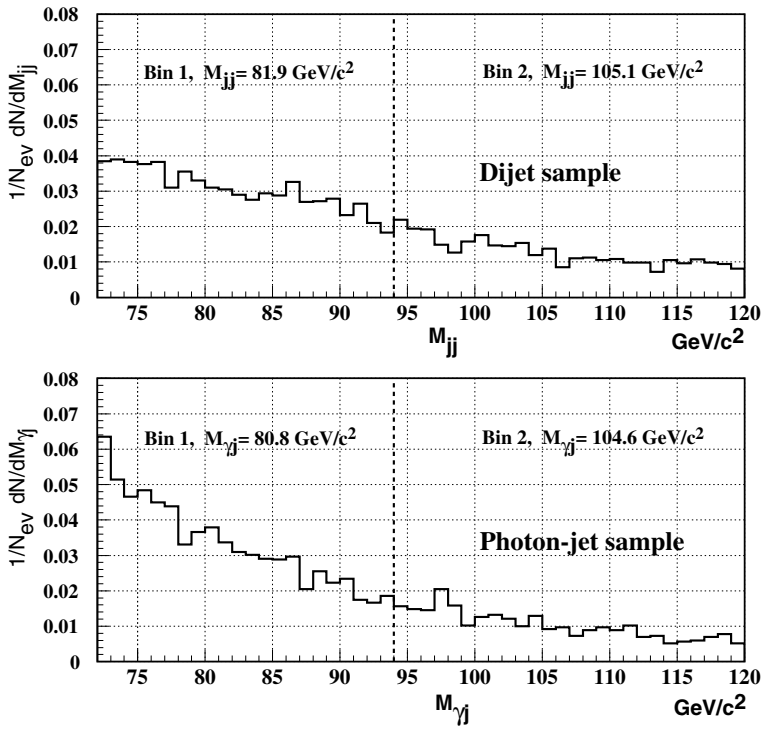

Figure 8–1: Invariant mass spectrum of dijet and photon+jet events which pass event selection cuts.

GeV cannot be used in the analysis because properties of jets from these events are biased by trigger requirements (trigger is not fully efficient for jets with energies close to the trigger threshold). At high energies ($M > 120$ GeV), the γ+jet sample has insufficient statistics. The invariant mass and E_T spectra for both data samples can be found on Fig. 8–1,8–2.

8.3 Fraction of Gluon Jets

The fractions of gluon jets in dijet events, f_g^{jj}, and pure photon+jet events, $f_g^{\gamma j}$, are determined from Herwig 5.6 and Pythia 6.115 Monte Carlo generators with parton distribution function sets CTEQ4M, CTEQ4A2, and CTEQ4A4 [69]. The results obtained with Herwig+CTEQ4M are taken as default. Fig. 8–3 shows the evolution of the gluon jet content with dijet or photon+jet invariant mass. The results on gluon jet fractions are presented in Table 8–1. The PDFs are very stable and well

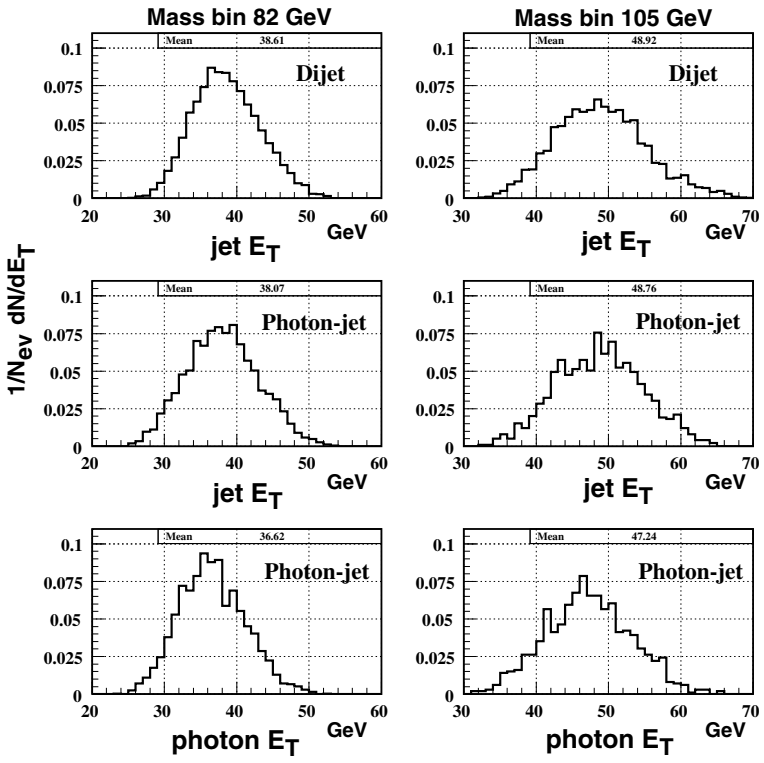

Figure 8–2: Transverse energy spectrum of jets and photons from dijet and photon+jet events after event selection cuts.

known in the region of relatively small $x_T = 2E_T/\sqrt{s}$ corresponding to jet energies used in the analysis.

8.4 Fraction of Real Photons

Generally, the photon+jet sample is contaminated by dijet events with one of the jets fragmented in such a way as to pass photon selection criteria (e.g., one prompt π^0 accompanied by a few very soft $\pi^{\pm}$, π^0's; see ref. [68] for more details). Requirement of the photon isolation in the calorimeter usually reduces the fraction of fakes by a large factor. However, the much larger dijet QCD production cross section results in a noticeable fraction of fake photons in the final sample.

There are two statistical methods to determine the remaining fraction of fake photons [68]. The conversion method is based on determining the number of photon conversions in the solenoid material by using the Central Preradiator Detector

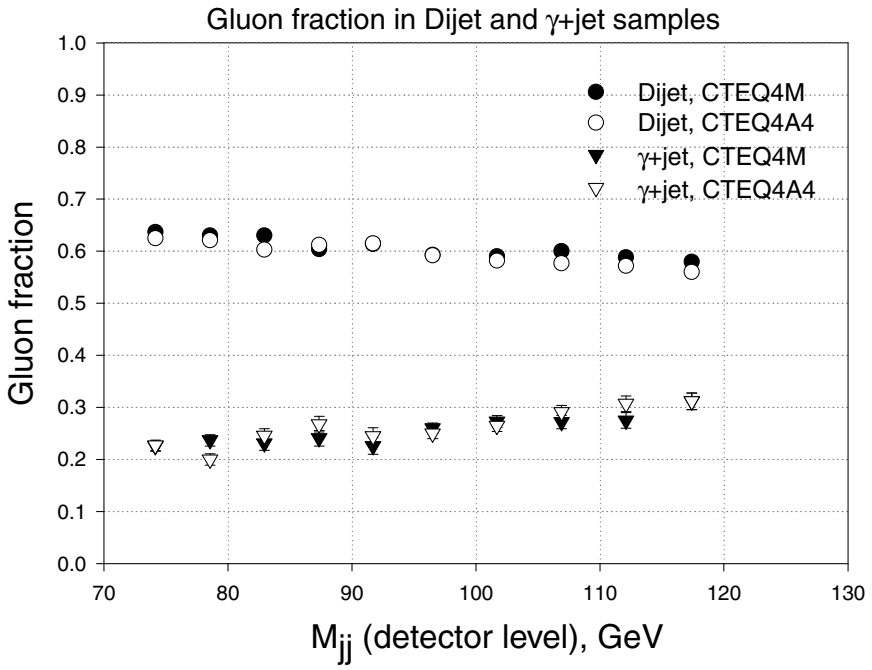

Figure 8–3: Fractions of gluon jets in dijet and γ+jet samples.

(CPR). The profile method exploits the difference in the transverse profile of the electromagnetic showers in the Central Electromagnetic Strip chambers (CES) caused by prompt single photons and background. The conversion method has an advantage of much smaller systematic uncertainties at high P_T's and an unlimited P_T range, while the profile method better separates signal from background in the low P_T region (it becomes inefficient at P_T>30 GeV). In our analysis, we consider photons with P_T>30 GeV and, therefore, use the conversion method implemented in the standard routine GETCPRWEIGHT.CDF.

The conversion method is based on evaluating the probability of conversions in the CPR right in front of the tower with electromagnetic cluster. Real photons have a conversion probability $\mu_\gamma = 1 - e^{-7/9X}$ (X is the amount of material in radiation lengths in front of the CPR), while fakes, being mostly π^0s, i.e. two photons, have higher conversion probability $\mu_B \simeq 1 - (1-\mu_\gamma)^2 = 2\mu_\gamma - \mu_\gamma^2$ (see ref. [68] for more details). The typical values of μ_γ and μ_B are ~0.6 and ~0.8, respectively. Therefore,

Table 8–1: Fractions of gluon jets in dijet events and in 100% pure γ-jet events obtained using Herwig and Pythia along with various sets of parton distribution functions.

PDF set	Dijet		100% pure γ-jet	
	41 GeV	52.5 GeV	41 GeV	52.5 GeV
Herwig+CTEQ4M (Default)	0.615±0.006	0.588±0.008	0.216±0.009	0.256±0.015
Herwig+CTEQ4A2	0.623±0.006	0.595±0.008	0.218±0.009	0.253±0.015
Herwig+CTEQ4A4	0.613±0.006	0.576±0.008	0.218±0.009	0.262±0.015
Pythia+CTEQ4M	0.623±0.006	0.598±0.008	0.197±0.009	0.250±0.015

if one has N photon candidates, out of which μN had conversions, the numbers of real photons and background can be estimated from the two equations: $N = N_B + N_\gamma$ and $\mu N = \mu_\gamma N_\gamma + \mu_B N_B$.

The fractions of real photons, δ_γ, in two mass bins are 75% (82 GeV/c^2) and 90% (105 GeV/c^2). As a cross-check we developed another empirical method of evaluating the fraction of fakes among photon candidates. It is described in Chapter 9. The method gave results consistent with the CPR weights.

8.5 Multiplicity Measurements

The analysis is carried out in the dijet (or photon+jet) center-of-mass frame, so that E_{jet}=$Mc^2/2$. Multiplicities of charged particles associated with jets in dijet and photon+jet events (N_{jj} and $N_{\gamma j}$) are measured for particles (tracks) falling into a restricted cone of $\theta_c = 0.28, 0.36, 0.47$ rad, where θ_c is the angle between the jet axis and the cone side (opening angle). The multiplicities are normalized "per jet".

There are three major sources of uncertainties we have to deal with when measuring the multiplicity of charged particles in jets from both data samples:

1. tracks from γ-conversions, K^0 and Λ decays (background correlated with jet direction);
2. secondary interactions, underlying event and accelerator induced backgrounds (background not correlated with jet direction);
3. CTC track reconstruction inefficiency.

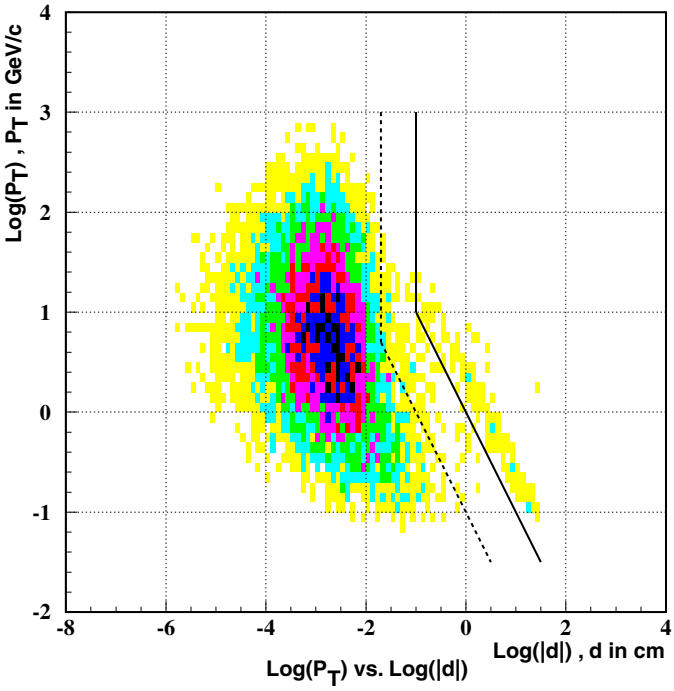

Figure 8–4: Example of the distribution of $\log p_T$ versus $\log d$ for tracks within a cone of θ_c=0.47 rad around the jet direction. Here, p_T is the transverse momentum of a track and d is the impact parameter. The default cut on the impact parameter is shown by the solid line, while the cut shown by the dashed line is used to estimate the systematic uncertainty.

8.5.1 Track Cuts

We apply vertex cuts to suppress tracks due to secondary interactions, γ-conversions, K^0 and Λ decays, or other backgrounds.

The first cut is on the track impact parameter, d, defined as the shortest distance (in $r-\phi$ plane) between the interaction point as measured by the SVX detector and the particle trajectory as obtained by the CTC tracking algorithm fit.

Fig. 8–4 shows the distribution of $\log(p_T)$ versus $\log(d)$ for the dijet events from the first bin (M_{jj}=82 GeV), where the large cluster of points corresponds to particles produced at the interaction point, and the straight line of correlated points to the right of the main region corresponds to $\gamma-$conversions happening in the cables

$$R = p/eB$$

$$d = \sqrt{R^2 + r^2} - R \approx R\left(1 + \frac{1}{2}\frac{r^2}{R^2}\right) - R = \frac{r^2}{2R} = \frac{eBr^2}{2p}$$

$$\log d = \log\left(\frac{eBr^2}{2}\right) - \log p$$

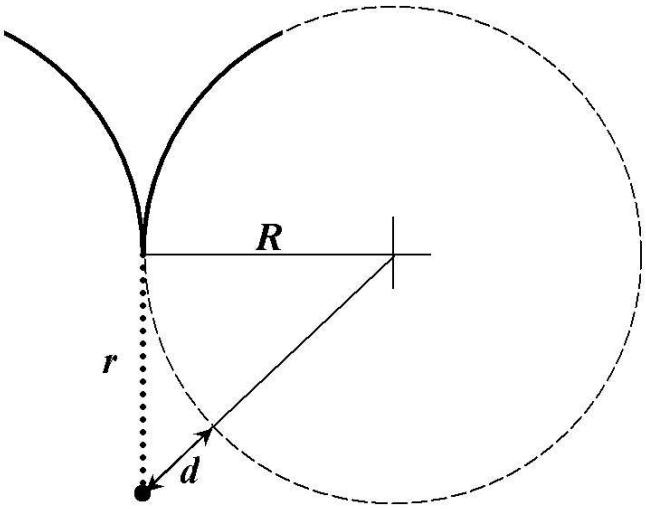

Figure 8–5: Illustration of correlation between transverse particle momentum, P_T, and impact parameter, d, for electrons and positrons produced in γ-conversions.

between the VTX and the CTC chambers. It can be shown (see Fig. 8–5) that for electrons and positrons produced in γ-conversions at radius r from the beam line, P_T and d have the following correlation:

$$\log P_T \simeq \log\left(0.15 r^2 B\right) - \log|d|, \tag{8.1}$$

where r and d are measured in meters, the magnetic field B in Tesla, and P_T in GeV/c.

The default cut on the impact parameter selects only tracks which, on the ($\log|d|$, $\log P_T$)-plane, are to the left of the strait line segments defined by the equations: $\log|d| = -1$ and $\log(|P_T d|) = 0$ (solid lines on Fig. 8–4).

The second vertex cut used is on Δz, defined as the difference between the z position of the track at the point of its closest approach to the beam-line and the position of the primary vertex as measured by the vertex detector (see Fig. 8–6).

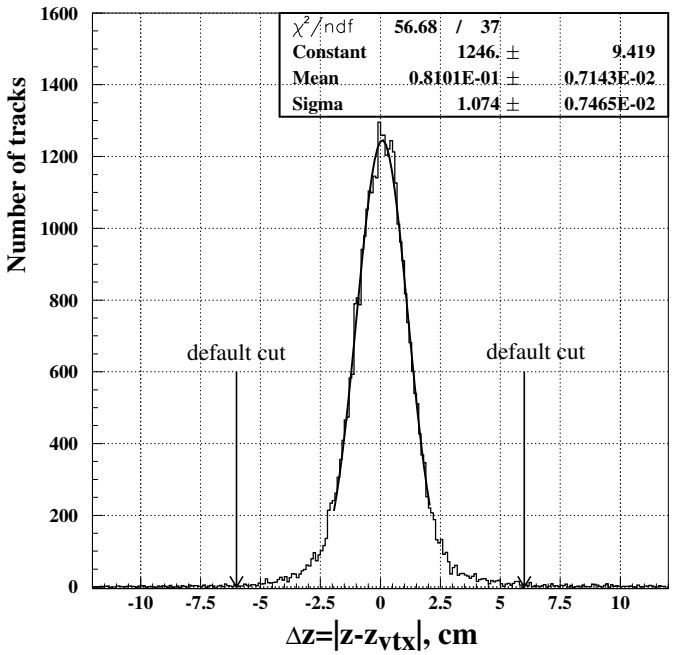

Figure 8–6: Example of the Δz distribution for tracks from events with only one vertex (primary interaction). Tracks are counted within a cone of θ_c=0.47 rad around the jet direction.

This cut helps to remove tracks from the secondary interactions. The default value of this cut is: $|\Delta z| < 6.0$ cm ($\sim 6\sigma_{\Delta z}$).

After applying vertex cuts, there is still a small number of correlated background tracks remaining, mostly due to $\gamma-$conversions. These are estimated by turning on/off conversions in the QFL detector simulation package. This fraction is found to be around 3.5%.

8.5.2 Background Tracks Removal

Tracks coming from the underlying event, multiple interactions in the same bunch crossing (with unresolved z-vertices), and any other uncorrelated backgrounds can be easily subtracted on average using complementary cones. A pair of complementary cones is defined such that their axis is in the plane normal to the dijet direction and at the same polar angle as the dijet axis (Fig. 8–7 shows the orientation of the complementary cones). Note that such cones can only be defined for jets in the region $45^o < \theta_{cm} < 135^o$ (corresponds to $|\eta_{jet1,2}| < 0.9$). These cones are expected

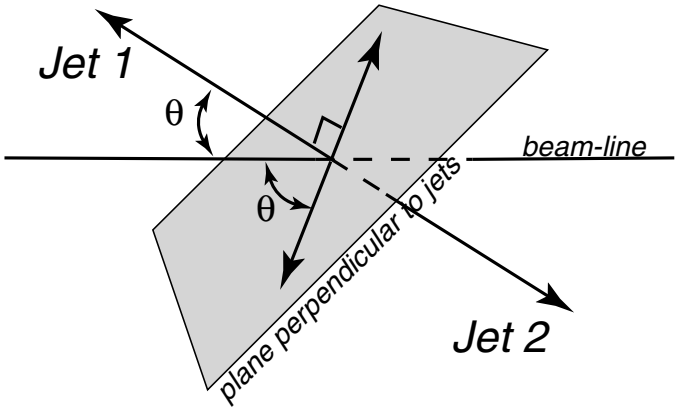

Figure 8–7: Illustration of the definition of complementary cones. The unlabeled arrows are the axes of cones complementary to jets 1 and 2.

to collect statistically the same uncorrelated background as the cones around the jets. However, there still could be a small fraction of tracks associated with jets which found their way into the complementary cones. There are several indications of that. In photon+jet events, the multiplicity in the half cone on the photon side of the complementary cone is about 7-9% less than that on the jet side. Finally, there is a small correlation between the multiplicity in the complementary cones and the multiplicity in cones around jets (see Fig. 8–8). To estimate the true contribution of the uncorrelated background, we made a linear fit of the dependence of mean complementary cone multiplicity on mean multiplicity in jets for events from dijet and photon+jet samples. The extrapolation of this function to zero was taken as an estimate of the uncorrelated background contribution in the jet cone (0.55 and 0.46 tracks per cone of θ_c =0.47 rad in dijet and photon+jet events, respectively).

8.5.3 Tracking Efficiency

We also corrected the measured multiplicities for the CTC track reconstruction inefficiency. We use the results of the method developed in ref. [70]. This method is based on embedding tracks at the CTC hit level into real events and re-running the full CTC track reconstruction. For this purpose, a track selected from one of the jets in dijet event is rotated 180^o in the center-of-mass frame, and embedded into the

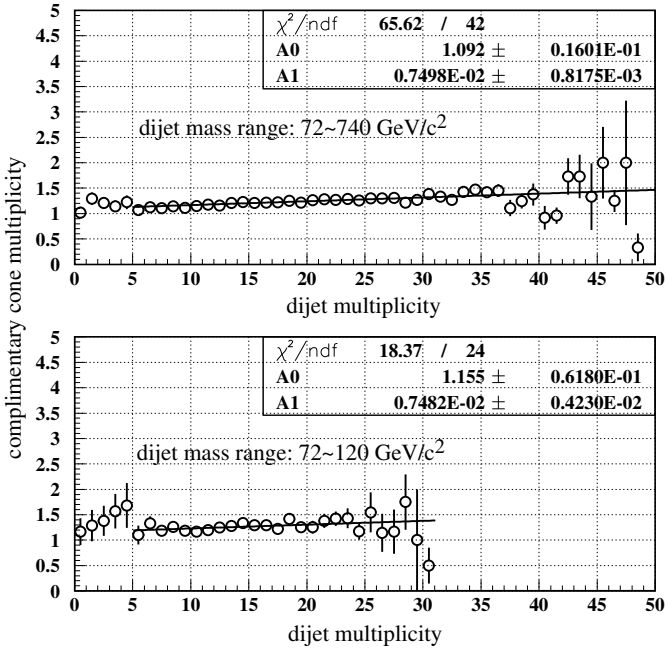

Figure 8–8: The correlation between multiplicity in complementary cones (per event) and dijet multiplicity (per event). The results of linear fit, $n_{compl.cone} = p_0 + p_1 \times n_{dijet}$ are shown. We do not fit the dependence in the region $n_{dijet} < 5$, because the contribution of uncorrelated background tracks can dominate in the dijet multiplicity in this region. The expected multiplicity of uncorrelated background tracks in a cone around the jet direction is estimated as $\frac{p_0}{2(1-p_1)}$. The results of the fit are almost the same (within statistical errors) for events with very different dijet mass which implies a very small dependence of the complementary cone multiplicity on the jet energy.

Table 8–2: Efficiencies of the track selection cuts for jets with the average energy E_{jet}=41 GeV. Stages of multiplicity measurements: raw multiplicity in cone, *Step1*; cut on $|dz|$, *Step2*; cut on impact parameter, d, and $\log P_T$, *Step3*; CTC efficiency corrections, *Step4*; correction for remaining γ-conversions, *Step5*; complementary cone subtraction, *Step6*.

	cone $\theta_c = 0.28$		cone $\theta_c = 0.36$		cone $\theta_c = 0.47$	
	Dijet	γ-jet	Dijet	γ-jet	Dijet	γ-jet
Step1	5.11 (100%)	4.71 (100%)	6.18 (100%)	5.65 (100%)	7.43 (100%)	6.74 (100%)
Step2	4.92 (96.4%)	4.50 (95.5%)	5.90 (95.5%)	5.33 (94.5%)	6.99 (94.1%)	6.29 (93.3%)
Step3	4.53 (88.7%)	4.03 (85.5%)	5.42 (87.7%)	4.76 (84.3%)	6.41 (86.3%)	5.61 (83.3%)
Step4	4.80 (94.1%)	4.28 (90.8%)	5.77 (93.4%)	5.07 (89.8%)	6.80 (91.6%)	5.95 (88.4%)
Step5	4.67 (91.4%)	4.16 (88.3%)	5.59 (90.4%)	4.91 (87.0%)	6.55 (88.2%)	5.74 (85.2%)
Step6	4.48 (87.7%)	4.01 (85.1%)	5.29 (85.6%)	4.64 (82.2%)	6.05 (81.5%)	5.31 (78.8%)

Table 8–3: Efficiencies of the track selection cuts for jets with the average energy E_{jet}=52.5 GeV. Stages of multiplicity measurements: raw multiplicity in cone, *Step1*; cut on $|dz|$, *Step2*; cut on impact parameter, d, and $\log P_T$, *Step3*; CTC efficiency corrections, *Step4*; correction for remaining γ-conversions, *Step5*; complementary cone subtraction, *Step6*.

	cone $\theta = 0.28$		cone $\theta = 0.36$		cone $\theta = 0.47$	
	Dijet	γ-jet	Dijet	γ-jet	Dijet	γ-jet
Step1	5.82 (100%)	5.29 (100%)	6.98 (100%)	6.29 (100%)	8.33 (100%)	7.49 (100%)
Step2	5.61 (96.3%)	5.06 (95.5%)	6.66 (95.4%)	5.95 (94.5%)	7.85 (94.1%)	6.99 (93.3%)
Step3	5.16 (88.7%)	4.48 (84.7%)	6.11 (87.5%)	5.29 (84.0%)	7.19 (86.3%)	6.20 (82.7%)
Step4	5.54 (95.2%)	4.82 (91.1%)	6.56 (94.0%)	5.69 (90.4%)	7.72 (92.7%)	6.67 (89.0%)
Step5	5.38 (92.5%)	4.68 (88.4%)	6.35 (91.0%)	5.50 (87.4%)	7.44 (89.2%)	6.42 (85.7%)
Step6	5.19 (89.2%)	4.53 (85.6%)	6.05 (86.7%)	5.23 (83.2%)	6.94 (83.3%)	5.99 (80.0%)

other jet. Then, the parameters of the reconstructed tracks are compared with their original values before embedding. Corrections obtained this way take into account the efficiency dependence on jet energy, particle momentum, and particle angle with respect to the jet axis. The size of these corrections on average multiplicities is 6-8%, depending on jet energy and cone size θ_c.

The results of multiplicity measurements with default set of cuts and corrections can be found in Tables 8–2,8–3.

8.6 Effect of Fake Photons

We use Monte Carlo (HERWIG and PYTHIA along with detector simulation) to study the $fake$ γ+jet events . To obtain the $fake$ γ+jet sample, we generated regular dijet events and selected only events passing the photon cuts. To get statistically meaningful sample of $fake$ γ+jet events ($\sim 3 * 10^3$ events), we had to generate $\sim 3 * 10^7$ dijet events (numbers are quoted for Pythia). Therefore, we found that the probability for a jet to fake a photon is on the order of $\sim 10^{-4}$. Fake photons, based on these studies, appear to be regular jets with usually a single π^0 faking a photon. It turns out that this π^0, on average, carries only about 90–93% of the original jet energy (see Fig. 8–9). The remaining 10% of the energy is carried by other particles from the original jet. This effect results in a mis-measurement of the dijet mass of

Table 8–4: The α-correction due to difference in multiplicities between a regular jet and a jet opposite to a fake photon. The opening angles are $\theta_C = 0.28,\ 0.36,\ 0.47$.

E_{jet}, GeV	Cone, θ_c	$Q{=}E_{jet}\theta_C$, GeV	HERWIG	PYTHIA	"Shifted" data
41	0.28	11.5	1.042±0.018	1.087±0.019	1.024±0.011
	0.36	14.7	1.025±0.016	1.075±0.017	1.025±0.010
	0.47	19.2	1.032±0.015	1.084±0.016	1.030±0.009
52.5	0.28	14.7	1.040±0.031	1.056±0.029	1.026±0.014
	0.36	18.9	1.023±0.028	1.056±0.029	1.035±0.013
	0.47	24.7	1.0±0.026	1.055±0.027	1.037±0.012

fake γ+jet events by about 3–5% (see Fig. 8–10). Therefore, *fake* γ+jet, on average, have higher true invariant mass than the reconstructed one. Consequently, the γ+jet mass bins are actually populated with *fake* γ+jet events of higher true $M_{\gamma j}$ values than the same mass bins in the case of dijet events. Thus, one can assume that the higher true energy may result in a higher multiplicity in the jet opposite to the fake photon (simply *fake* later in text) as compared to a regular jet from a dijet event. We found that multiplicities in jets opposite to fakes, N_{fj}, are typically a few percent higher than those in jets from regular dijet events, N_{jj}. Table 8–4 presents the results for the ratio $\alpha{=}N_{fj}/N_{jj}$ obtained in these studies.

Assuming that jet fragmentation occurs independently in each of the jets, one can also obtain α from the dijet data sample by artificially shifting the energy of one of the jets (*fake*) by the same 7–10%. This crosscheck gives similar results to what we have obtained from Monte Carlo simulations. As a default estimate of α, we take the average results obtained from HERWIG, PYTHIA, and "shifted" dijet data.

There is one more interesting observation which we can make with the Monte Carlo studies of *fake* γ+jet events. It turns out that only about 3–6% (Herwig predicts smaller fraction than Pythia) fakes are gluon jets. As we show in these studies, quark jets have, on average, lower particle multiplicity then the gluon jets and it is, therefore, conceivable that it is easier for a quark jet to fluctuate into a single high energy pion.

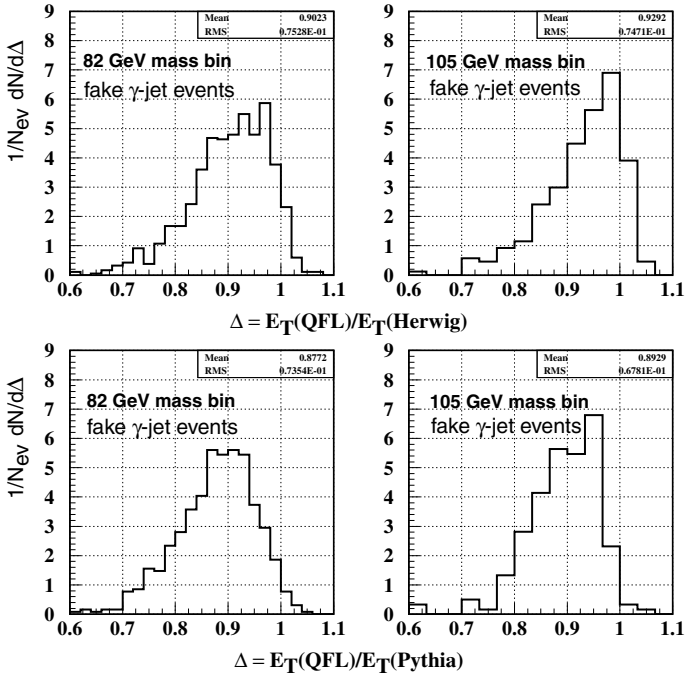

Figure 8–9: The ratio of the measured energy of a fake photon (detector level) to the real energy of a parent jet (MC parton level).

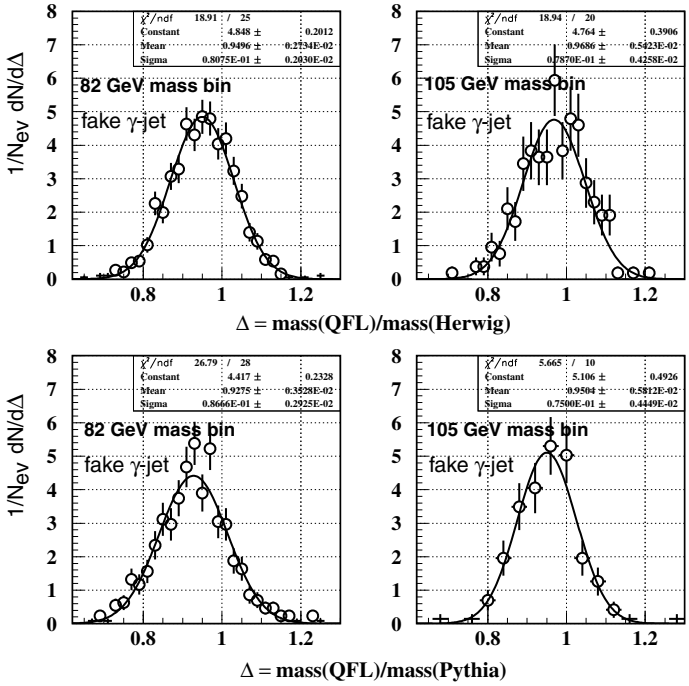

Figure 8–10: The ratio of the measured invariant mass of a $fake\ \gamma$+jet event (detector level) to the real invariant mass (MC parton level).

Table 8–5: Results of the measurements with the default set of cuts. The multiplicities in dijet events, N_{jj}, and in photon+jet events, $N_{\gamma j}$, do not include corrections for remaining particles from K_s^0 and Λ decays and losses of low P_T tracks.

E_{jet}		41 GeV			52.5 GeV	
θ_c	0.28 rad	0.36 rad	0.47 rad	0.28 rad	0.36 rad	0.47 rad
$Q=E_{jet}\theta_c$	11.5 GeV	14.7 GeV	19.2 GeV	14.7 GeV	18.9 GeV	24.7 GeV
N_{jj}	4.476±0.025	5.287±0.027	6.052±0.029	5.19±0.04	6.05±0.04	6.94±0.04
$N_{\gamma j}$	4.01±0.04	4.64±0.04	5.31±0.05	4.53±0.07	5.23±0.08	6.00±0.08
f_g^{jj}	0.615±0.006	same	same	0.588±0.008	same	same
$f_g^{\gamma j}$	0.216±0.009	same	same	0.256±0.015	same	same
δ_γ	0.75±0.04	same	same	0.90±0.07	same	same
α	1.040±0.016	1.035±0.014	1.041±0.015	1.032±0.012	1.036±0.011	1.034±0.011

8.7 Final Corrections and Results

Now that we measured or evaluated N_{jj}, $N_{\gamma j}$, f_g^{jj}, $f_g^{\gamma j}$, δ_γ and α (see Table 8–5), we can calculate N_g, N_q and $r = N_g/N_q$, using Eqs. 3.4-3.6. In order to obtain the final results, two corrections must be applied. These corrections are derived from Monte Carlo and are expected to be different for quarks and gluons, which makes it natural for them to be applied in the last order.

The production rates of K_s^0 and Λ's depend on jet type. The fraction of these particles is enhanced in jets originating from $s-$ and c-type quarks compared to gluon jets or jets originating from u and d quarks. Therefore, including their decay products can bias the measurement of the ratio of charged particle multiplicities. One of the purposes of the vertex cuts is to suppress tracks due to K_s^0 and Λ decays. However, there is still a considerable fraction of charged particles from these decays which pass the cuts. In order to evaluate and remove this contribution the following study was performed. We compared two Monte Carlo samples: one sample with γ-conversions, K_s^0 and Λ decays switched "OFF", and another sample with only γ-conversions switched "OFF". Comparing the MC level multiplicities, we were able to find the fraction of particles coming from K_s^0 and Λ decays. From comparison with the detector level (MC+QFL) multiplicities, we found what fraction of these particles passed the cuts. Given these numbers, we obtained multiplicity correction factors:

Table 8–6: Effect of K_s^0 and Λ decays on the charged particle multiplicity within a cone of the opening angle θ_c=0.47. The results presented in the Table are based on Herwig. Multiplicity correction factors are essentially the same for Pythia and smaller opening angles, θ_c=0.28, 0.36.

Jet type	Fraction of ch. particles from K_s^0 and Λ decays	Fraction of ch. particles from decays which passed cuts	Multiplicity corr. factor
Gluon	8%	47%	0.96
u, d-quarks	9%	46%	0.96
s-quark	15%	56%	0.92
c-quark	10%	44%	0.96
all quarks	10%	49%	0.95

Table 8–7: Charged particle multiplicities in small cones around gluon and quark jet directions and their ratio, N_g, N_q and $r = N_g/N_q$ respectively. Multiplicities do not include charged particles from K_s^0 and Λ decays.

E_{jet}	θ_c	Q=$E_{jet}\theta_c$	N_g	N_q	$r = \frac{N_g}{N_q}$
	0.28	11.5 GeV	4.98±0.07±0.52	3.28±0.11±0.37	1.52±0.08±0.13
41 GeV	0.36	14.7 GeV	6.02±0.08±0.55	3.70±0.11±0.40	1.63±0.09±0.14
	0.47	19.2 GeV	6.94±0.08±0.58	4.23±0.12±0.47	1.64±0.09±0.14
	0.28	14.7 GeV	5.94±0.12±0.69	3.70±0.17±0.43	1.60±0.12±0.19
52.5 GeV	0.36	18.9 GeV	7.02±0.13±0.72	4.22±0.18±0.49	1.66±0.13±0.20
	0.47	24.7 GeV	8.08±0.14±0.72	4.86±0.19±0.57	1.66±0.13±0.18

$\sim$0.96 for gluon jets and $\sim$0.95 for quark jets. Results of these studies can be found in Table 8–6.

Finally, the measured multiplicities were corrected for losses of low P_T tracks due to curling in the magnetic field of the solenoid (the efficiency for reconstructing tracks with $P_T < 300$ MeV is practically zero). To make this correction, we estimate the fraction of Monte Carlo tracks (before detector simulation) with $P_T < 300$ MeV (below this threshold P_T distribution of charged tracks after QFL simulation is falling sharply). The correction is small: $\sim$2% for gluon jets and $\sim$1% for quark jets.

The final results (including the described above corrections) on N_g, N_q and $r = N_g/N_q$, are presented in Table 8–7.

CHAPTER 9
SYSTEMATIC UNCERTAINTIES AND CROSS-CHECKS

The sources of systematic uncertainties are discussed in the following sections and are summarized in Tables 9–1,9–2, 9–3.

9.1 Event Selection

Ideally, the results of an analysis should not depend on the event selection. In practice, the event selection cuts always introduce certain biases in properties of objects being studied. It is important to choose the cuts such that these biases are minimal or could be corrected by a simple procedure.

The systematic uncertainties due to the event selection cuts include effects related to the choice of η-cut on jets, presence of the second vertex, and difference in the energy balance between dijet and photon+jet events. We do not include in this list effects related to photon identification and jet reconstruction because the uncertainties associated with these effects will be discussed separately.

There are two reasons why the multiplicity in jets may depend on η_{jet}: detector effect associated with a decrease in tracking efficiency in the forward region, and a real physics effects associated with the initial-to-final state color coherence. The first effect is accounted for by the CTC efficiency corrections [70]. The second effect is expected to make almost no impact on the inclusive properties of jets such as multiplicities if particles are counted in *small cones* around the *centrally* produced jets (these two conditions are met in our analysis). To confirm that the initial-to-final color coherence effects are negligible at the conditions of the analysis, the following test was conducted. The coherence effects, if present, should reveal themselves in the angular distribution, $dn/d\beta$, of particles around jets (see [71, 72]). The radial or polar angle β is defined in (η, ϕ)-plane as follows: $\Delta\eta = \Delta R cos\beta$, $\Delta\phi = \Delta R sin\beta$ where $\Delta\eta$,

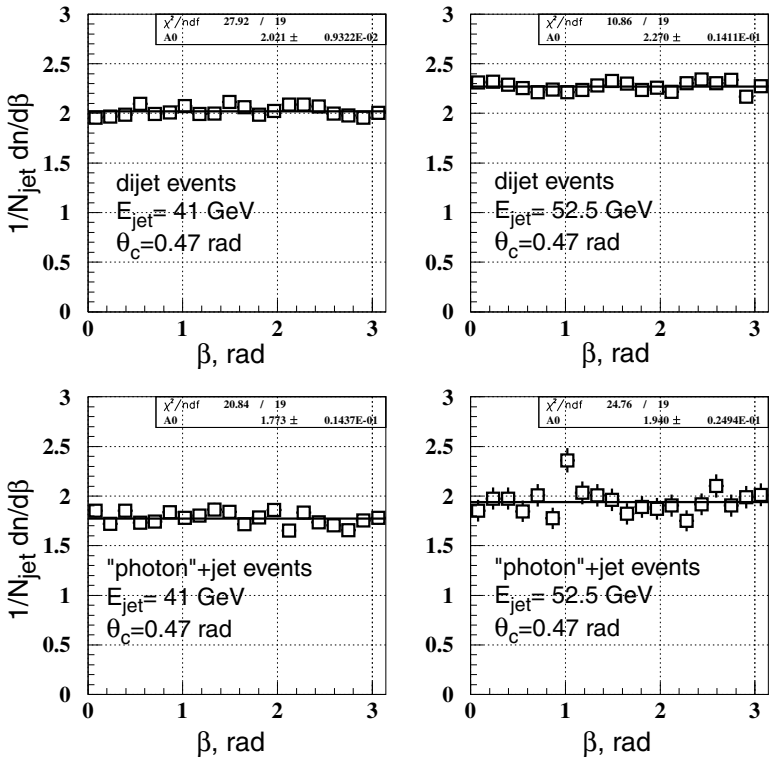

Figure 9–1: The angular distribution of particles in cone 0.47 around jet direction. No signature of the color coherence effects is observed (distributions are fairly flat). The color coherence effects would reveal themselves in the increased density of particles in the preferred direction ($\beta = \pi/2$ for γ+jet events and $\beta = 0,\ \pi$ for dijet events).

$\Delta\phi$, and $\Delta R = \sqrt{\Delta\eta^2 + \Delta\phi^2}$ correspond to an angular distance between a particle and a jet. Fig. 9–1 shows that the angular distribution is fairly flat. Therefore, the coherence effects are negligible because otherwise we would see an increase in particle production in certain preferred directions (see ref. [72] for more details).

The default set of event selection cuts allows up to two primary vertices in an event. The fraction of N_{vx}=2 events in our data set is $\sim 17\%$. One of the reasons we keep such events is that the CPR method was tuned on an inclusive sample of photons with some fraction of events with multiple vertices (mostly N_{vx}=1 and N_{vx}=2 events, with a small fraction of $N_{vx} \geq$3 events). On the other hand, the presence of the second vertex introduces some ambiguities in assigning tracks to vertices which results in a 4–6% difference in particle multiplicity in jets from one and two vertex events. To

estimate the systematic uncertainty associated with this effect, we repeat the analysis conservatively assuming that multiplicities in jets from N_{vx12}=1 and N_{vx12}=2 events are the same (i.e., use $N_{jj,\gamma j}^{N_{vx}=1}$ instead of $N_{jj,\gamma j}^{N_{vx}\leq 2}$). The effect on the multiplicities in quark and gluon jets is found to be ~1-2%. The corresponding value of uncertainty on the ratio r is ~2-4%.

An energy balance cut is applied to select events with well measured jets. The dijet and photon+jet events are required to pass exactly the same cut: $|\vec{E}_{T_1} + \vec{E}_{T_2}|/(E_{T_1}+E_{T_2}) < 0.15$. It is important that jets in selected dijet and real photon+jet events have the same properties. However, applying the same energy balance cut to events from both samples can lead to a small bias. The photon energy resolution is much better than that of jets. Therefore, from this naive point of view, γ-*jet* balance is expected to be better (or narrower) than *jet*-*jet* one. At the same, time there are factors which can lead to a broadening of the γ-*jet* balance (in fact, we see in data that γ-*jet* and *jet*-*jet* are almost the same; see Fig. 9–2). One of these factors is the presence of fakes which energies are ~10% less than energies of jets recoiling against them. The other factor is a small relative offset (~ 4% according to MC) in the energy scales of quarks and gluons (because jet corrections are obtained for an average jet from dijet sample). Therefore, it leads to a natural offset in balance of γ-g and γ-q pairs which, in turn, results in broadening of a generic γ-*jet* balance. Because all these effects described above are quite small and there is no a clear way to correct for them, we simply assign a systematic uncertainty associated with the effect of the energy balance cut. To evaluate this effect we use a tighter cut (motivated by MC studies; see Fig. 9–3) for photon+jet events: $|\vec{P}_{T_1} + \vec{P}_{T_2}|/(P_{T_1} + P_{T_2}) < 0.125$. The corresponding uncertainties turn out to be ~3% for the ratio r and ~1-2% for the measured multiplicties, N_q and N_g.

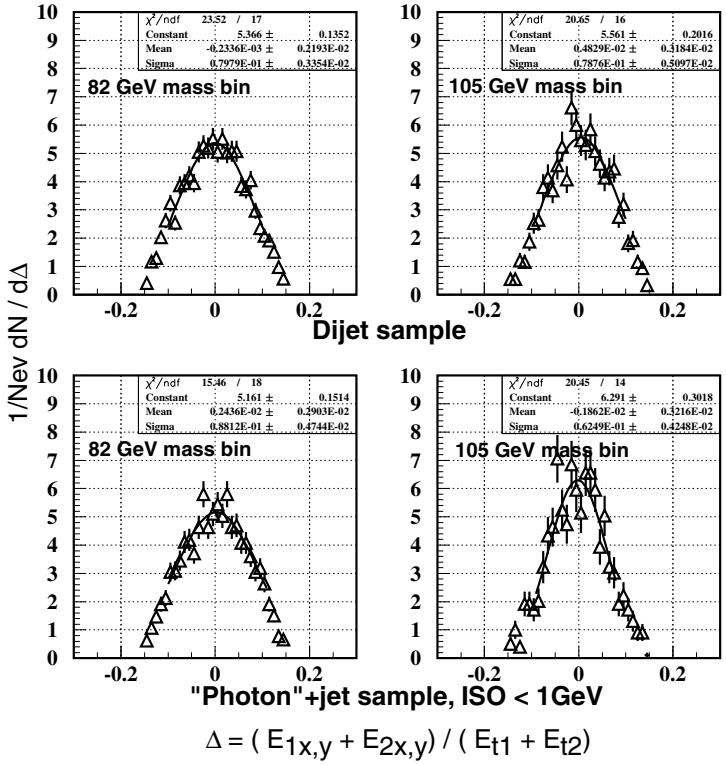

Figure 9–2: Energy balance in data: $|\vec{E}_{T_1} + \vec{E}_{T_2}|/(E_{T_1} + E_{T_2})$.

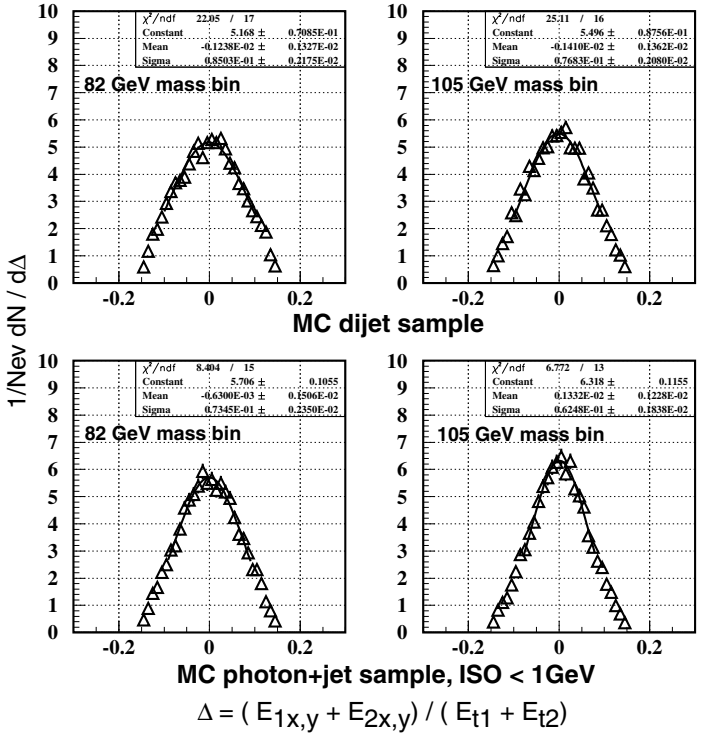

Figure 9–3: Energy balance in Herwig Monte Carlo: $|\vec{E}_{T_1} + \vec{E}_{T_2}|/(E_{T_1} + E_{T_2})$.

9.2 Jet Reconstruction and Energy Corrections

There are four effects associated with jet reconstruction and energy corrections: jet algorithm bias, mis-measurement of the jet direction, uncertainty in the jet energy scale, and migration of events between mass bins. These effects and their corresponding uncertainties are discussed below.

In theory, there are only two initial partons or jets. In practice, the number of reconstructed jets depends on the resolution parameters of the clustering algorithm. Therefore, the properties of jets will depend in some way on the jet clustering algorithm. To estimate this potential bias, the following study was conducted. We compare the properties of Monte Carlo jets reconstructed with three different jet clustering cones: R=0.4, R=0.7 (default in our analysis) and R=1.0. The events are selected using the standard set of cuts. To disentangle effects related to jet algorithm and energy corrections, the comparison is done for jets of the same energy at MC generator level (true energy of outgoing partons). Charged particles are counted in cones of various sizes around the true direction of the outgoing parton and the direction of the reconstructed jet. This procedure allows for an estimate of the potential bias due to selecting jets with specific properties and the bias due to mis-measurement of the jet direction. The results of the study can be found in Figs. 9–4, 9–5. From these plots one can make two conclusions: the bias due to the size of a clustering cone depends on the opening angle θ_c and a flavor of a jet (it is bigger for gluon jets than for quark jets). Thus, the effect of the jet algorithm is found to be negligible for the results obtained with the opening angle θ_c=0.47. However, it becomes one of the leading systematic uncertainties for multiplicities in quark and gluon jets measured in smaller opening angles, θ_c=0.28 and θ_c=0.36. The corresponding bias in the measurements of the ratio r turns out to be small (1-3%) for all three opening angles.

To understand the effect of the jet clustering algorithm, it is helpful to consider how the cluster merging procedure of the cone algorithm works. In general, a jet has

a subjet structure in the angular distribution of particles. These subjets, or clusters, can be merged by the jet finder in one jet or reconstructed as separate jets. The chance for two clusters to be merged depends on the clustering cone size and on the fraction of energy they share. For instance, two clusters of about the same energy and separation ΔR=0.6 will be reconstructed as *two* R=0.4 jets in about 80% of the cases and as *one* R=0.7 jet in about 80%-90% of the cases. Based on this example, one can conclude that cone R=0.4 jets will have much fewer subjets than cone R=1.0 jets which has two consequences for jet direction resolution. First, it results in a better jet direction resolution for smaller clustering cones (see Fig. 9–6). Second, there are situations when the reconstructed jet direction does not coincide with the direction of any of the subjets. It happens more frequently for cone R=1.0 jets than for cone R=0.4 jets. Therefore, for small opening angles θ_c one may count particles in the region between subjets where the density of particles is small. This explains the multiplicity behavior in cones with small opening angle: $N_{R=0.4\ jet} \geq N_{R=0.7\ jet} \geq N_{R=1.0\ jet}$. The situation changes for large opening angles. It was shown above that the chance for a cone R=1.0 jet to consist of two clusters (or subjets) is greater than for a cone R=0.4 jet. It is also known that $N(E_1) + N(E_2) \geq N(E_0 = E_1 + E_2)$, where $N(E)$ is the multiplicity in a jet (or subjet) with energy E. Therefore, it is more likely for large opening angle cones to contain most tracks from both clusters (or subjets). All this explains why the multiplicity behavior at large opening angles is reversed: $N_{R=0.4\ jet} \leq N_{R=0.7\ jet} \leq N_{R=1.0\ jet}$.

The systematic uncertainty due to imprecise knowledge of the actual jet direction is evaluated by using Monte Carlo quark and gluon jets. The difference between the multiplicity in a cone around the reconstructed jet direction and the multiplicity in a cone around the true direction of an initial parton is taken to be an estimate of the corresponding systematic uncertainty. The effect appears to be negligible.

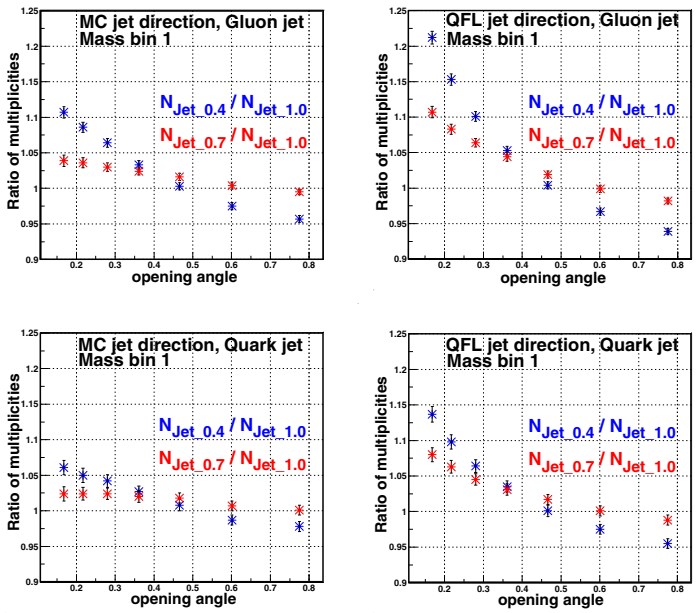

Figure 9–4: Difference in charged particle multiplicities between jets reconstructed with different clustering cone sizes. The multiplicity ratios, $N_{R=0.4\ jet}/N_{R=1.0\ jet}$ and $N_{R=0.7\ jet}/N_{R=1.0\ jet}$, are presented as functions of the opening angle θ_c. Results are obtained by counting particles around the true parton direction and the reconstructed jet direction (QFL jets). MC data from mass bin 1 is presented.

The overall uncertainty on the jet energy scale is 5%. To evaluate its effect on the measurements, we use the standard CDF routine JTC96X to vary the jet energy around the measured value. It includes both systematic *up* and *down* shifts in the absolute energy scale and the relative, η_d-dependent, scale. After each shift in the jet energy scale, the entire data set is re-processed and events are re-selected with default cuts. The maximum variation in results is taken as an estimate of the corresponding systematic uncertainty. Imprecise knowledge on the jet energy scale is one of the leading sources of systematic uncertainties in the analysis. The size of this uncertainty is 2-5% for the multiplicities in quark and gluon jets and 4-9% for the ratio, $r = N_g/N_q$.

There is another effect closely related to the jet energy measurement. It is a migration of events between mass bins. Given the $\sim$ 10% jet energy resolution, a jet's measured energy can fluctuate to significantly lower or higher values compared

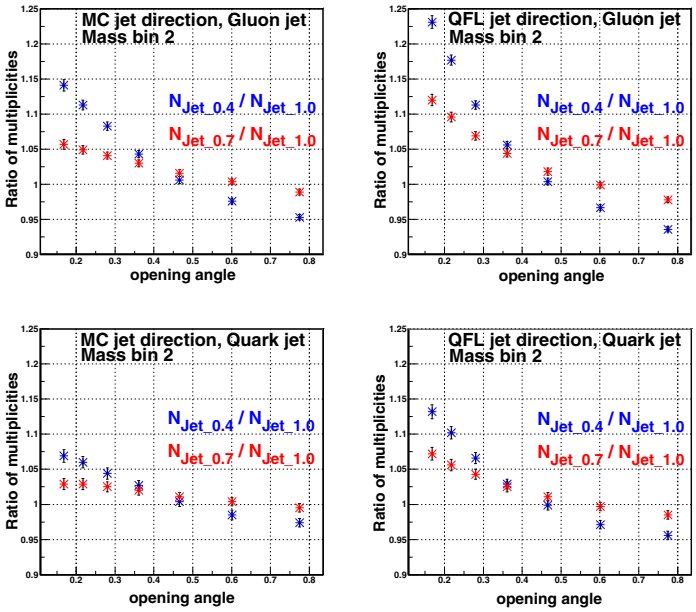

Figure 9–5: Difference in charged particle multiplicities between jets reconstructed with different clustering cone sizes. The multiplicity ratios, $N_{R=0.4\ jet}/N_{R=1.0\ jet}$ and $N_{R=0.7\ jet}/N_{R=1.0\ jet}$, are presented as functions of the opening angle θ_c. Results are obtained by counting particles around the true parton direction and the reconstructed jet direction (QFL jets). MC data from mass bin 2 is presented.

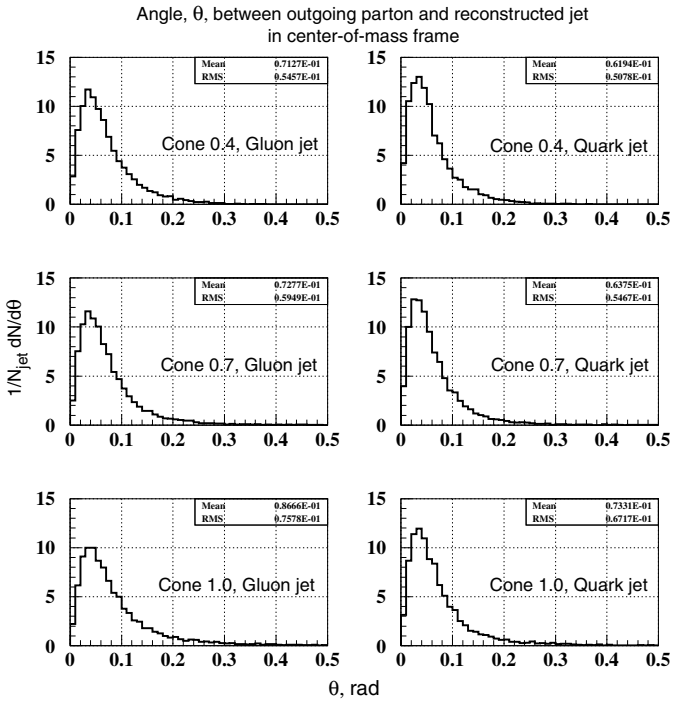

Figure 9–6: Angle between the direction of an outgoing parton and the direction of a reconstructed jet.

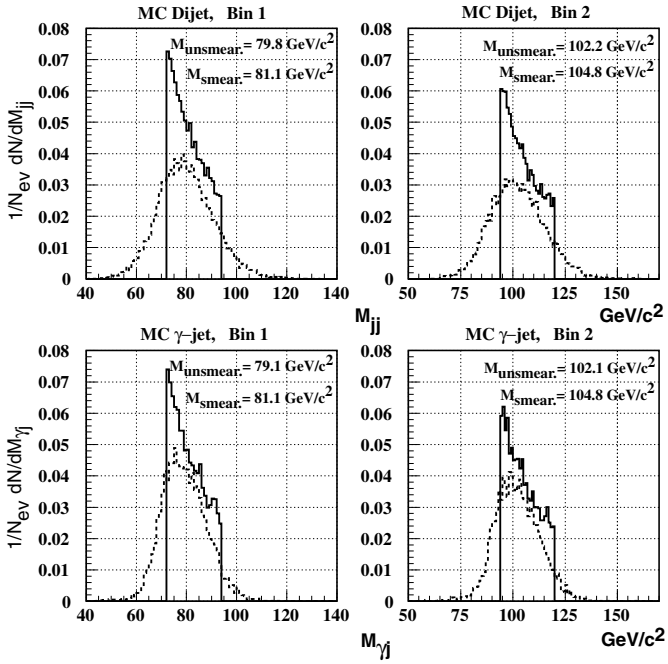

Figure 9–7: Invariant mass spectrum of Monte Carlo dijet and γ+jet samples. The solid line histogram is the detector level (smeared) distribution. The dashed line histogram is the unsmeared distribution.

to its true energy. This can also propagate into the measured invariant mass of an entire event so that it can fall into a wrong mass bin. Taking into account that the invariant mass spectrum is close to a falling exponential, it leads to an average effective migration of the events to the higher masses (see Fig. 9–7). As a result of this migration, the unsmeared invariant mass is about 2% less than the measured (smeared) one. Given the fact that the multiplicity depends on the logarithm of the energy and that this smearing effect is smaller than the uncertainty on the jet energy scale, we decided not to apply any unsmearing correction to the data. But to be conservative, we assign the corresponding systematic uncertainty which is estimated by comparing the default results with the results obtained by applying the unsmearing procedure and taking into account a small difference in invariant mass distributions of dijet and photon+jet events. The effect of the smearing correction turns out to be negligible for both mass bins.

9.3 Presence of Fake Photons

The photon identification cuts obviously do not affect the properties of jets in pure photon+jet events because a photon and a jet are independent objects in these events. On the other hand, the photon selection cuts have a direct impact on the purity of the sample and the properties of *fake* γ+jet events. In the analysis, the presence of fake photons is accounted for by two parameters, δ_γ and α. Below we will discuss the systematic uncertainties associated with the evaluation of these parameters.

We use the conversion method to determine the real photon content in the photon+jet data sample as described in Section 8.4. This method was developed by the CDF photon group and implemented in the standard routine GETCPRWEIGHT.CDF. This routine also provides means of estimating the systematic uncertainties associated with the conversion method.

The main backgrounds for prompt photons are single π^0's and η's decaying into two γ's. There are smaller backgrounds from other multi-π^0 states ($\eta \to \pi^0\pi^0\pi^0$, $K^0_S \to \pi^0\pi^0$ and jets with $2\pi^0$) which, obviously, give more photons. The conversion probability for background photons is re-calculated using the measured η/π^0 and K^0_S/π^0 production rates. All these corrections are implemented in the standard GETCPRWEIGHT.CDF routine. The deviation from a simple two-photon model is taken to be the systematic uncertainty. The GETCPRWEIGHT.CDF routine also provides estimates of the systematic uncertainties due to back-scattered electromagnetic showers and the presence of CPR hits from the underlying event. All these individual sources of uncertainties in the determination of the real photon content, δ_γ, are summarized in Table 9–4. We repeat all the measurements using these deviated values of δ_γ to evaluate the corresponding effect on the final results. The uncertainty in the fraction of real photons, δ_γ, leads to a significant uncertainty, 4-6%, in the measurements of the ratio, $r = N_g/N_q$.

We rely on Monte Carlo simulation of the *fake* γ+jet events. To make sure that MC provides an adequate description of these events, we conduct the following test which is based on the difference in shape of the isolation energy distributions for real photons and fakes. Thus, the additional (isolation) energy in cones R =0.4 around real photons is mostly due to the underlying event and its distribution has an approximately exponential shape with typical average value of 0.65 GeV per cone R=0.4 [73, 74]. At the same time, the isolation energy in cones around fake photons is dominated by contributions from jet debris. According to Monte Carlo simulation, the isolation energy in cones around fakes has a fairly flat distribution (see Fig. 9–8). From Fig. 9–8, we can also notice that the distribution in photon+jet data looks very much like a weighted sum of the exponential (which is how the underlying event contribution should look) and a "shelf–like" contribution due to fakes. If true, the weights can be extracted and used as a direct measurement of the photon content in a data sample. We can try to use this to discriminate between the two in attempt to estimate the fraction of real photons in the data sample and also to predict such fraction for any given isolation cut. Thus, we perform a very simple calculation. We estimate the area under the real data curve in the region from ISO=3 GeV to ISO=4 GeV (see Fig. 9–8). Assuming that this region is dominated by fakes, we can then use the number of fakes per unit of ISO to predict the fraction of fakes (or real photons) in a sample with arbitrary cut on isolation. Fig. 9–9 shows the comparison of this proposed method to the standard CPR based results. One can see that even with our *"back of the envelope"* calculations, we obtain an impressively good agreement. This test gives us confidence that Monte Carlo correctly reproduces main properties of fake photons.

Finally, we estimate the systematic uncertainty associated with the α-correction. This correction depends on the Monte Carlo simulation of fake photons which relies on a particular fragmentation model. The fragmentation models implemented in

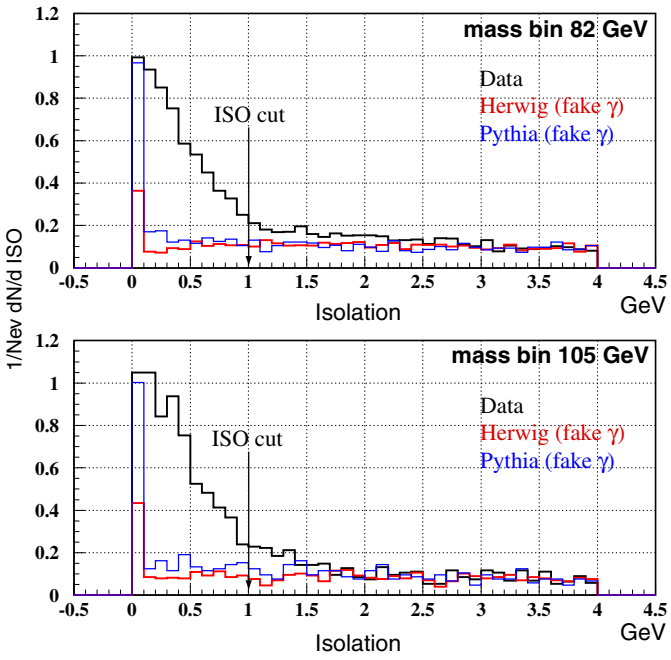

Figure 9–8: Isolation energy distribution in photon+jet data and Monte Carlo *fake* γ+jet events. The Monte Carlo distributions are scaled to be the same as data in the region $ISO > 3.0$ GeV (mostly populated by fakes).

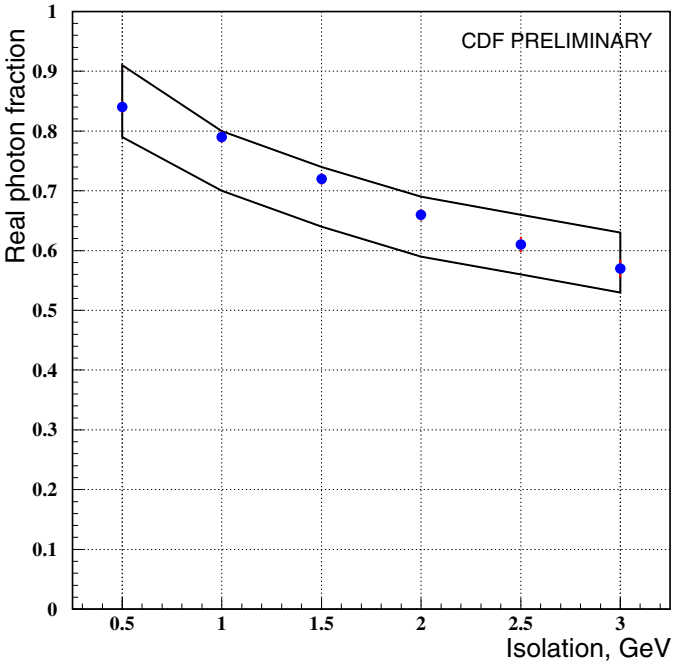

Figure 9–9: The predicted real photon content as a function of the cut on isolation energy in a cone around photon candidate (dots—prediction based on the shape of the isolation energy distributions in data and Monte Carlo fakes, band—real photon fraction and its uncertainty based on the standard conversion method). The results are presented for events from both mass bins

Herwig and Pythia are very different. We repeat the measurements using the Herwig and Pythia based values of the α-parameter. The difference between results is taken to be a systematic uncertainty associated with the dependence on the Monte Carlo fragmentation model in the evaluation of the α-parameter. The effect turns out to be small.

9.4 PDF Uncertainties

As mentioned in Section 8.3, the fractions of gluon jets in dijet events, f_g^{jj}, and pure γ-jet events, $f_g^{\gamma j}$, are determined from Herwig and Pythia Monte Carlo generators with PDF sets CTEQ4M, CTEQ4A2, and CTEQ4A4. The results obtained with Herwig+CTEQ4M are taken as default. The largest variations in results (typically 1-3%) obtained with different Monte Carlo generators and PDFs are treated as estimates of the corresponding systematic uncertainties.

9.5 Uncertainties in Multiplicity Measurements

The choice of the impact parameter cut is motivated by the distribution of correlated points on the ($\log|d|$,$\log P_T$)-plane (see discussion in Section 8.5 and Fig. 8–4). The position of the straight line on the Fig. 8–4 corresponds to roughly $6\sigma_d$ of the impact parameter resolution. Moving this cut further to the left would remove more background tracks, but would also start eliminating some signal tracks from the tails of the impact parameter resolution. The natural point of closest approach is around $3\sigma_d$. Thus, the position of the deviated cut is set to eliminate all tracks outside the region of $3\sigma_{impact}$ (dashed line on the Fig. 8–4). For all measured values, the difference in results is assigned to the systematic uncertainty associated with the impact parameter requirements.

The parameter Δz is used to exclude tracks due to secondary interactions in the same bunch crossing. Fig. 8–6 shows Δz distribution for tracks from dijet events with only one vertex. The $|\Delta z| < 6.0$ cm criterion motivated the requirement $|z_1 - z_2| <$ 12.0 cm on the spatial separation of primary vertices in two-vertex events used in the

event selection described earlier. To estimate the systematics due to a choice of Δz cut, we repeat all the measurements with tightened cut of $|\Delta z| < 4.0$ cm which is three times less than the distance between two vertices.

The background track removal by means of cuts on Δz and impact parameters is the leading source of systematic uncertainty (typical value is 5-8%) in the measurement of multiplicity in quark and gluon jets. At the same time, these cuts have a small effect (typically less than 3%) on the measurement of the ratio, $r = N_g/N_q$.

For the γ-conversions remaining after the vertex cuts, the correction based on Monte Carlo studies is applied. We conservatively estimate the associated uncertainty to be equal to the correction itself (typical value is $\sim$3.5%).

The results are also corrected for the remaining (after vertex cuts) decay products of K_s^0 and Λ. The correction procedure is based on Monte Carlo studies. The associated systematic uncertainty is conservatively taken to be equal to the correction itself (typical value is $\sim$4-5%).

The contribution of uncorrelated background to multiplicity in jet cone is determined using the complementary cone technique. The multiplicity of tracks (0.55 tracks per cone of θ_c=0.47 rad in dijet events and 0.46 tracks in photon+jet events for both mass bins) from complementary cones associated with this source of background is extracted from fitting procedure described in Section 8.5. To estimate the systematic uncertainty due to uncorrelated background subtraction, we repeat all the measurements with the average (not extrapolated) complementary cone multiplicity.

As mentioned earlier, the jet multiplicity is corrected for CTC inefficiency. This correction is the same for dijet and photon+jet data samples. The default correction is equal to 6.3% for events with jet energy of E_{jet}=41 GeV and 7.5% for E_{jet}=52.5 GeV (both corrections are quoted for θ_c=0.47). To estimate the systematic effect of CTC corrections on the ratio r, we repeat all the measurements with no CTC correction and with both *"optimistic"* and *"pessimistic"* CTC correction scenarios

(see ref. [60, 70]). The variations in r appear to be negligible. In the case of charged particle multiplicities in quark and gluon jets, the difference in the results obtained with *"optimistic"* and *"pessimistic"* scenarios is assigned to be the corresponding systematic uncertainty (<2%).

Another source of systematic uncertainty is the losses of low P_T tracks because of curling in the magnetic field of the solenoid. We evaluate the fraction of lost tracks from Herwig. The correction turns out to be small (<2%), so we conservatively estimate the associated uncertainty to be equal to correction itself.

Table 9–1: The summary of systematic uncertainties in the measurements of N_g, N_q, and $r = N_g/N_q$ obtained for the opening angle $\theta_c = 0.47$. The errors are rounded.

Default cuts & corrections	Syst. uncertainty evaluation method	E_{jet}=41 GeV ΔN_g	ΔN_q	$\Delta r = \frac{N_g}{N_q}$	E_{jet}=52.5 GeV ΔN_g	ΔN_q	$\Delta r = \frac{N_g}{N_q}$
correction for N_{vx12}=2 events	use $N_{jj,\gamma j}^{N_{vx12}=1}$	-0.04	0.06	-0.03	-0.07	0.11	-0.05
Jet energy scale: JTC96X option: DDYY	max. dev. using MDYY, PDYY, DMYY & DPYY	0.20	DMYY -0.09	0.09	-0.31	PDYY 0.15	-0.11
Jet energy balance: $\frac{\lvert\vec{E}_{T_1}+\vec{E}_{T_2}\rvert}{(E_{T_1}+E_{T_2})} < 0.15$	< 0.125 (photon+jet only)	-0.06	0.04	-0.05	0.06	-0.09	0.05
Inv. mass spec. correction: N/A	Applied	-0.01	0.0	0.0	0.0	0.0	0.0
Jet algorithm: Cone R=0.7 jets	MC comparison of, R=0.4, 0.7, 1.0 jets	0.13	0.07	0.0	0.14	0.05	0.01
Impact param.: $\lvert d\rvert < 6\sigma_d$	$\lvert d\rvert < 3\sigma_d$	-0.30	-0.28	0.03	-0.32	-0.35	0.06
$\lvert\Delta z\rvert < 6$ cm	$\lvert\Delta z\rvert < 4$ cm	-0.13	-0.10	0.01	-0.14	-0.15	0.02
remaining γ-conv. corr.: MC-based	no correction	0.23	0.15	0.0	0.28	0.17	0.0
K_s^0 and Λ decays corr.: MC-based	no correction	0.28	0.22	-0.02	0.33	0.25	-0.01
uncorrelated bckg.: extrapolated compl. cone multiplicity	measured compl. cone multiplicity	-0.07	-0.08	0.02	-0.15	-0.01	-0.03
Default CTC efficiency corr.	no eff. correction	N/A	N/A	0.0	N/A	N/A	0.01
	"optimistic" corr.	-0.01	-0.01	0.0	-0.04	-0.03	0.0
	"pessimistic" corr.	0.02	0.01	0.0	0.05	0.02	0.0
P_T <300 MeV trks.: MC correction	no correction	-0.13	-0.06	-0.01	-0.16	-0.05	-0.01
Jet direction: reconstructed jet	MC comparison: QFL jet vs. MC jet	0.06	0.04	0.0	0.06	0.04	0.0
fraction of gl. jets: CTEQ4M+Herwig	CTEQ4A2+Herwig	-0.04	0.0	-0.01	-0.05	0.03	-0.02
	CTEQ4A4+Herwig	0.01	-0.01	0.01	0.12	-0.07	0.05
fraction of real photons: default CPR method	CPR hit rate	-0.06	0.09	-0.05	-0.06	0.09	-0.04
	Back-scattering	0.07	-0.12	0.06	0.11	-0.15	0.07
	η/π^0 rate	0.02	-0.03	0.01	0.01	-0.01	0.0
	K_S/π^0 rate	-0.02	0.03	-0.01	-0.01	0.01	0.0
α-correction: average of all meth.	difference between Herwig & Pythia	0.01	-0.08	0.03	-0.06	-0.01	-0.01

Table 9–2: The summary of systematic uncertainties in the measurements of N_g, N_q, and $r = N_g/N_q$ obtained for the opening angle $\theta_c = 0.36$. The errors are rounded.

Default cuts & corrections	Syst. uncertainty evaluation method	E_{jet}=41 GeV ΔN_g	ΔN_q	$\Delta r = \frac{N_g}{N_q}$	E_{jet}=52.5 GeV ΔN_g	ΔN_q	$\Delta r = \frac{N_g}{N_q}$
correction for N_{vx12}=2 events	use $N_{jj,\gamma j}^{N_{vx12}=1}$	-0.05	0.07	-0.04	-0.09	0.14	-0.07
Jet energy scale: JTC96X option: DDYY	max. dev. using MDYY, PDYY, DMYY & DPYY	0.14	DMYY -0.07	0.07	-0.34	PDYY 0.18	-0.14
Jet energy balance: $\frac{\lvert\vec{E}_{T_1}+\vec{E}_{T_2}\rvert}{(E_{T_1}+E_{T_2})} < 0.15$	< 0.125 (photon+jet only)	-0.07	0.10	-0.06	0.02	-0.03	0.02
Inv. mass spec. correction: N/A	Applied	0.0	0.01	0.0	-0.01	0.0	0.0
Jet algorithm: Cone R=0.7 jets	MC comparison of, R=0.4, 0.7, 1.0 jets	0.25	0.11	0.02	0.31	0.10	0.03
Impact param.: $\lvert d\rvert < 6\sigma_d$	$\lvert d\rvert < 3\sigma_d$	-0.28	-0.23	0.02	-0.30	-0.27	0.04
$\lvert\Delta z\rvert < 6$ cm	$\lvert\Delta z\rvert < 4$ cm	-0.10	-0.08	0.01	-0.11	-0.11	0.02
remaining γ-conv. corr.: MC-based	no correction	0.18	0.10	0.0	0.21	0.12	0.0
K_s^0 and Λ decays corr.: MC-based	no correction	0.24	0.18	0.02	0.28	0.21	0.02
uncorrelated bckg.: extrapolated compl. cone multiplicity	measured compl. cone multiplicity	0.07	-0.04	0.03	-0.11	0.06	-0.05
Default CTC efficiency corr.	no eff. correction	N/A	N/A	0.0	N/A	N/A	0.01
	"optimistic" corr.	-0.06	-0.03	0.0	-0.09	-0.05	0.0
	"pessimistic" corr.	0.05	0.03	0.0	0.09	0.05	0.0
P_T <300 MeV trks.: MC correction	no correction	-0.08	-0.04	-0.01	-0.11	-0.03	-0.01
Jet direction: reconstructed jet	MC comparison: QFL jet vs. MC jet	0.09	0.05	0.0	0.11	0.06	0.0
fraction of gl. jets: CTEQ4M+Herwig	CTEQ4A2+Herwig	-0.03	0.0	-0.01	-0.05	0.03	-0.02
	CTEQ4A4+Herwig	0.01	-0.02	0.01	0.10	-0.06	0.05
fraction of real photons: default CPR method	CPR hit rate	-0.05	0.07	-0.05	-0.05	0.07	-0.04
	Back-scattering	0.06	-0.10	0.06	0.09	-0.13	0.08
	η/π^0 rate	0.01	-0.02	0.02	0.01	-0.01	0.01
	K_S/π^0 rate	-0.02	0.02	-0.02	0.0	0.01	0.0
α-correction: average of all meth.	difference between Herwig & Pythia	0.01	-0.05	0.02	-0.06	0.02	-0.02

Table 9–3: The summary of systematic uncertainties in the measurements of N_g, N_q, and $r = N_g/N_q$ obtained for the opening angle $\theta_c = 0.28$. The errors are rounded.

Default cuts & corrections	Syst. uncertainty evaluation method	E_{jet}=41 GeV ΔN_g	ΔN_q	$\Delta r = \frac{N_g}{N_q}$	E_{jet}=52.5 GeV ΔN_g	ΔN_q	$\Delta r = \frac{N_g}{N_q}$
correction for N_{vx12}=2 events	use $N_{jj,\gamma j}^{N_{vx12}=1}$	-0.03	0.05	-0.03	-0.06	0.09	-0.05
Jet energy scale: JTC96X option: DDYY	max. dev. using MDYY, PDYY, DMYY & DPYY	0.14	DMYY -0.07	0.07	-0.32	PDYY 0.15	-0.14
Jet energy balance: $\frac{\lvert\vec{E}_{T_1}+\vec{E}_{T_2}\rvert}{(E_{T_1}+E_{T_2})} < 0.15$	< 0.125 (photon+jet only)	-0.07	0.11	-0.07	0.0	-0.01	0.01
Inv. mass spec. correction: N/A	Applied	0.0	0.01	0.0	0.01	0.01	0.0
Jet algorithm: Cone R=0.7 jets	MC comparison of, R=0.4, 0.7, 1.0 jets	0.32	0.15	0.03	0.41	0.15	0.05
Impact param.: $\lvert d\rvert < 6\sigma_d$	$\lvert d\rvert < 3\sigma_d$	-0.25	-0.19	0.01	-0.27	-0.23	0.03
$\lvert\Delta z\rvert < 6$ cm	$\lvert\Delta z\rvert < 4$ cm	-0.07	-0.06	0.01	-0.08	-0.08	0.02
remaining γ-conv. corr.: MC-based	no correction	0.13	0.09	0.0	0.16	0.10	0.0
K_s^0 and Λ decays corr.: MC-based	no correction	0.20	0.16	-0.01	0.24	0.18	-0.01
uncorrelated bckg.: extrapolated compl. cone multiplicity	measured compl. cone multiplicity	-0.01	-0.02	0.0	-0.03	-0.01	0.0
Default CTC efficiency corr.	no eff. correction	N/A	N/A	0.0	N/A	N/A	0.01
	"optimistic" corr.	-0.04	-0.03	0.0	-0.07	-0.04	0.0
	"pessimistic" corr.	0.05	0.03	0.0	0.07	0.05	0.0
P_T <300 MeV trks.: MC correction	no correction	-0.05	-0.03	0.0	-0.07	-0.02	0.0
Jet direction: reconstructed jet	MC comparison: QFL jet vs. MC jet	0.11	0.06	-0.01	0.13	0.07	0.0
fraction of gl. jets: CTEQ4M+Herwig	CTEQ4A2+Herwig	-0.02	0.0	-0.01	-0.04	0.02	-0.02
	CTEQ4A4+Herwig	0.01	-0.01	0.01	0.06	-0.04	0.05
fraction of real photons: default CPR method	CPR hit rate	-0.03	0.05	-0.04	-0.04	0.06	-0.03
	Back-scattering	0.05	-0.07	0.05	0.07	-0.10	0.07
	η/π^0 rate	0.01	-0.02	0.01	0.0	0.0	0.0
	K_S/π^0 rate	-0.01	0.01	-0.01	-0.01	0.01	0.0
α-correction: average of all meth.	difference between Herwig & Pythia	0.02	-0.05	0.03	-0.06	0.03	-0.02

Table 9–4: Fraction of real photons in the photon+jet sample and its associated systematic uncertainties. Results are based on CPR weights calculated by GETCPRWEIGHT.CDF routine.

Jet Energy (GeV)	Default	CPR hit rate	Back–scattering	η/π^0	K_S/π^0
41	0.75±0.04	0.78±0.04	0.70±0.04	0.73±0.04	0.75±0.04
52.5	0.90±0.07	0.94±0.07	0.85±0.07	0.90±0.07	0.90±0.07

CHAPTER 10
DISCUSSION OF RESULTS

In this Chapter, the experimental results on the differences between quark and gluon jets that were obtained in this study are presented and compared to the theory calculations, other experimental measurements and Monte Carlo predictions.

10.1 Multiplicity of Charged Particles in Gluon and Quark Jets

The average multiplicities of charged particles in gluon and quark jets, N_g and N_q, for two different jet energies and three opening angles, as well as their ratio r, are summarized in Table 8–7 and presented in Figs. 10–1, 10–2,10–3.

The comparison of CDF results on the ratio $r = N_g/N_q$ to the theoretical predictions and the model-independent e^+e^- experimental results can be found in Fig. 10–1. The NLLA curves [24, 25, 26, 27] on this plot are calculated using Q_{eff}=230 MeV [60]. The ratio agrees well with re-summed perturbative QCD calculations, $1.4 \leq r \leq 1.8$ [24, 25, 26, 27], and is consistent with recent results from OPAL, $r \simeq 1.5$ [54]. The ratio is also in good agreement with the previous CDF model-dependent measurement, $r=1.7\pm0.3$ [59]. From Fig. 10–1, one can also see that the ratio r tends to increase with energy scale. This trend is statistically significant, because both statistical and systematic uncertainties are strongly correlated. At a jet energy of E_{jet}=41 GeV and opening angles θ_c=0.28 and 0.47 rad (Q=11.5 GeV and 19.2 GeV), we find $\Delta r = r(19.2\text{ GeV}) - r(11.5\text{ GeV}) = 0.12 \pm 0.02(\text{stat}) \pm 0.05(\text{syst})$ which is a $\sim 2\sigma$ significance level.

Fig. 10–2 shows the measured charged particle multiplicities in gluon and quark jets. Also shown on Fig. 10–2 are the fits to CDF data obtained by using recent 3NLLA expressions [26] with normalization constant as the only free parameter (the other parameter Q_{eff} is set to 230 MeV [60]). The fits for gluon and quark jet data

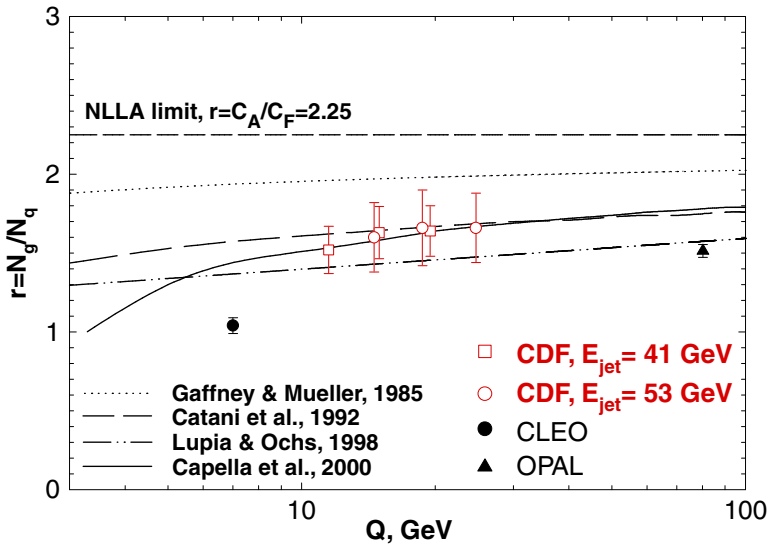

Figure 10–1: The ratio of charged particle multiplicities in gluon and quark jets as a function of jet hardness Q, which is $Q{=}E_{jet}\theta_c$ for CDF data and $Q{=}E_{c.m.}{=}2E_{jet}$ for e^+e^- data. CDF results are obtained for cone sizes θ_c=0.28, 0.36, and 0.47 rad. The NLLA curves [24, 25, 26, 27] are calculated using Q_{eff}=230 MeV [60]. The asymptotic value ($Q{\to}\infty$, of r is simply the ratio of the gluon and quark color charges, C_A=3 and C_F=4/3, respectively.

points are independent. The width of bands corresponds to the uncertainty in the overall normalization. From Fig. 10–2, one can see that the multiplicities in quark and gluon jets follow the predicted evolution with jet energy and opening angle as a function of $Q{=}E_{jet}\theta_c$. The model-independent e^+e^- results [49, 54, 75] (except for CLEO data at $Q{\sim}$5-7 GeV) fall within the fit bands and, thus, are in agreement with CDF results. This comparison, however, is indirect because the measurements are done at very different energy scales.

Fig. 10–3 shows the comparison of CDF results on multiplicity in gluon jets with recent model-dependent and indirect results from OPAL [55, 56]. The range of energy scales is the same in both experiments, thus allowing for a direct comparison. One can see that CDF and OPAL data are in good agreement.

To compare the results of this analysis to the predictions of Monte Carlo event generators, we use Herwig 5.6 and Pythia 6.115 along with QFL detector simulation.

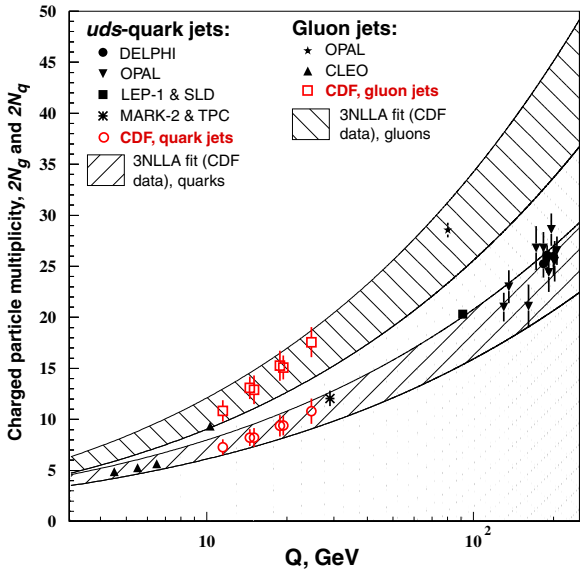

Figure 10–2: Average charged particle multiplicities in gluon and quark jets as a function of jet hardness Q, which is $Q{=}E_{jet}\theta_c$ for CDF data and $Q{=}E_{c.m.}{=}2E_{jet}$ for e^+e^- data. For the purpose of comparison to the e^+e^- measurements, CDF results on this plot include charged particles from K^0_S and Λ decays and are multiplied by two. The fits to CDF data are obtained by using the recent NLLA expressions from Ref. [26] with normalization constant as the only free parameter (the other parameter Q_{eff} is set to 230 MeV [60]). The width of the bands corresponds to the uncertainty in the overall normalization.

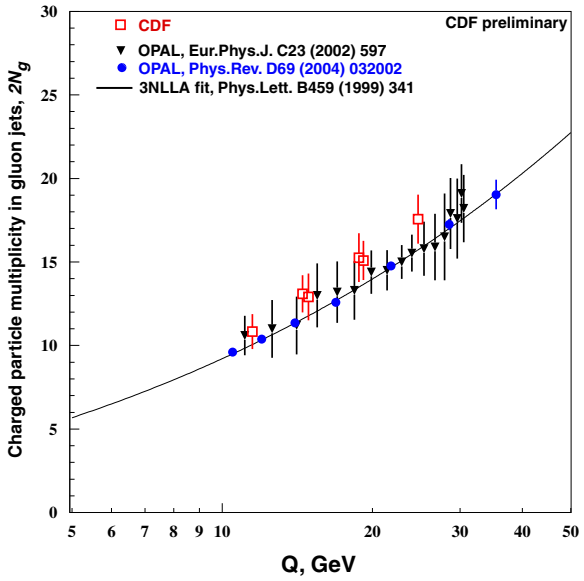

Figure 10–3: Comparison of CDF results on charged particle multiplicity in gluon jets with recent model-dependent and indirect results from OPAL. The theoretical curve on this plot is the 3NLLA fit [76] to model-independent e^+e^- results on multiplicity in gluon jets [50, 54].

First, we investigated if the properties of quark and gluon jets from dijet events are similar to those from photon+jet events. To disentangle the detector resolution and event reconstruction effects, we compare the charged particle multiplicities in jets of the same energies at the hadron level of the generator before the detector simulation. The differences in multiplicity in jets of the same type (gluon, u,d,s,c-quarks) are found to be within statistical uncertainties (typically $< 1.5\%$). Therefore, Monte Carlo does assume the universality of jets.

Three approaches were used to find the multiplicities in gluon and quark jets and their ratio: 1) considering jets from dijets events only, 2) considering jets from photon+jet events only, and 3) using the results from modified Eqs. 3.4-3.6. In order to apply Eq. 3.4 to Monte Carlo data, we, of course, take δ_γ=1. Then, the MC version of Eq. 3.4 reads as follows:

$$r = \frac{N_g}{N_q} = 1 + \frac{1 - \frac{N_{\gamma j}}{N_{jj}}}{f_g^{jj} \times \frac{N_{\gamma j}}{N_{jj}} - f_g^{\gamma j}} \tag{10.1}$$

The results for all three methods are found to be essentially the same, the combined results are presented in Table 10–1. Looking on this data, we can draw several important conclusions. First, Pythia predicts higher multiplicity in gluon and quark jets compared to Herwig: 1.6-6.3% and 1.4-4.0%, depending on the cone size. Second, the Monte Carlo results follow the $E_{jet}\theta_c$ scaling. Third, the differences between data and Monte Carlo multiplicities in gluon jets are well within the statistical uncertainties of this measurement, and the multiplicity in Monte Carlo quark jets is about 30% ($\sim 2\sigma_{syst}$) higher than that in the data (see Fig. 10–4). Finally, Monte Carlo predicts the ratio, $r = N_g/N_q$, to be in the range $1.2 \leq r \leq 1.4$ (see Fig. 10–5) which is lower by the same $2\sigma_{syst}$ than the measured ratio in the data, $1.5 \leq r \leq 1.7$.

Table 10–1: Monte Carlo results for charged particle multiplicities in small cones around gluon and quark jet directions and their ratio, N_g, N_q and $r = N_g/N_q$ respectively. Multiplicities do not include charged particles from K^0_s and Λ decays.

MC gen.	E_{jet}		40.6 GeV			52.4 GeV	
	cone, θ_c	0.28 rad	0.36 rad	0.47 rad	0.28 rad	0.36 rad	0.47 rad
	Q=$E_{jet}\theta_c$	11.4 GeV	14.6 GeV	19.1 GeV	14.7 GeV	18.9 GeV	24.6 GeV
Herwig	N_g	5.05±0.03	6.04±0.02	7.20±0.02	5.92±0.04	7.05±0.05	8.27±0.03
	N_q	4.19±0.02	4.78±0.02	5.47±0.02	4.77±0.03	5.40±0.03	6.18±0.04
	$r = \frac{N_g}{N_q}$	1.21±0.01	1.27±0.01	1.32±0.01	1.25±0.01	1.32±0.01	1.34±0.01
Pythia	N_g	5.14±0.05	6.27±0.03	7.51±0.02	6.11±0.08	7.33±0.06	8.65±0.06
	N_q	4.26±0.04	4.93±0.06	5.62±0.06	4.85±0.04	5.58±0.03	6.32±0.07
	$r = \frac{N_g}{N_q}$	1.21±0.01	1.29±0.01	1.34±0.01	1.28±0.01	1.34±0.01	1.38±0.01

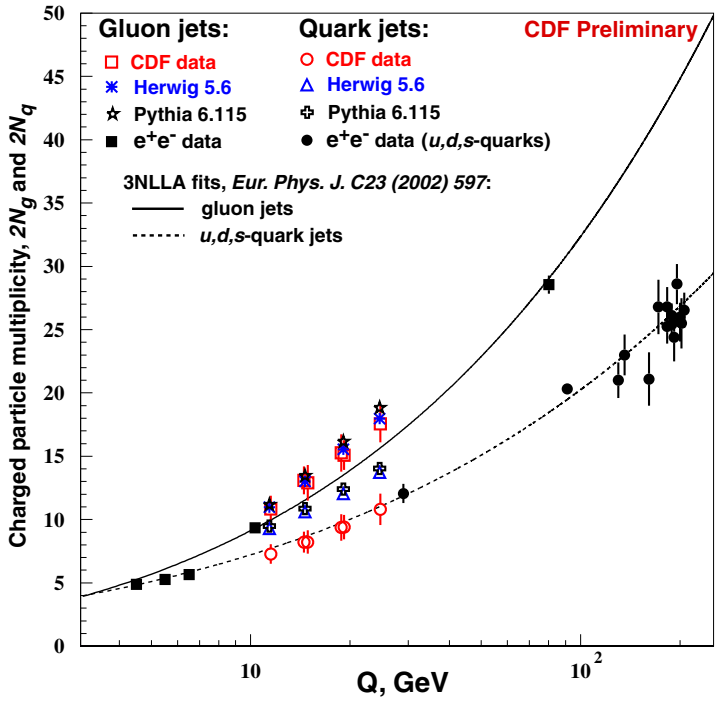

Figure 10–4: Comparison of Monte-Carlo predictions to data: average charged particle multiplicities in gluon and quark jets. The theory curves are 3NLLA fits [26] to gluon and quark data from e^+e^- experiments. The fit parameters are taken from the last publication under ref. [75]. This particular choice of theory curves is motivated only by convenience of comparison. The e^+e^- results include only model-independent measurements.

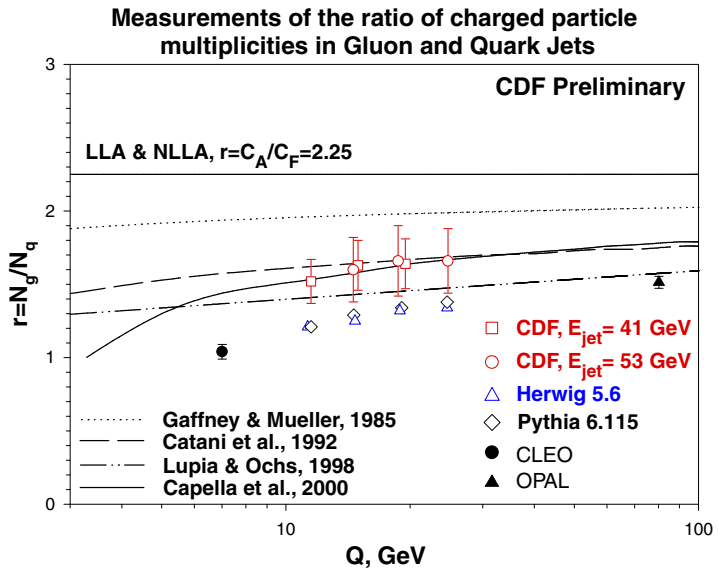

Figure 10–5: Comparison of Monte-Carlo predictions to data: the ratio of charged particle multiplicities in gluon and quark jets. Theory curves and experimental points are the same as on Fig.10–1. The e^+e^- results include only model-independent measurements.

10.2 Momentum Distribution of Charged Particles in Gluon and Quark Jets.

In addition to average multiplicities, we also obtained the momentum distributions, $\frac{1}{N_{jet}}\frac{dN}{d\xi}$ (where $\xi = \ln\frac{E_{jet}}{p}$ and p is particle's momentum), of charged particles from gluon and quark jets, as well as their ratio $r(\xi) = \frac{1/N_{g.jet}dN_g(\xi)/d\xi}{1/N_{q.jet}dN_q(\xi)/d\xi}$, for E_{jet}=41 GeV and θ_c=0.47 rad. The technique was almost the same, except that the momentum spectrum of charged particles was subdivided into bins of width $\Delta\xi = 0.5$ and multiplicities were measured for each bin. These results are summarized in Tables 10–2,10–3,10–4 and presented on Figs. 10–6-10–9.

It is interesting to consider the ratio of momentum distributions, $r(\xi)$, of charged particles from gluon and quark jets. The ratio of multiplicities in gluon and quark jets, r, should approach r=C_A/C_F=2.25 in the asymptotic limit of infinite jet energies. However, this regime can be reached even at current jet energies [29]. For the limited region of phase space, the conservation laws are not a constraint. Thus, the asymptotic condition can be met for soft particles with $p \ll E_{jet}$. The qualitative

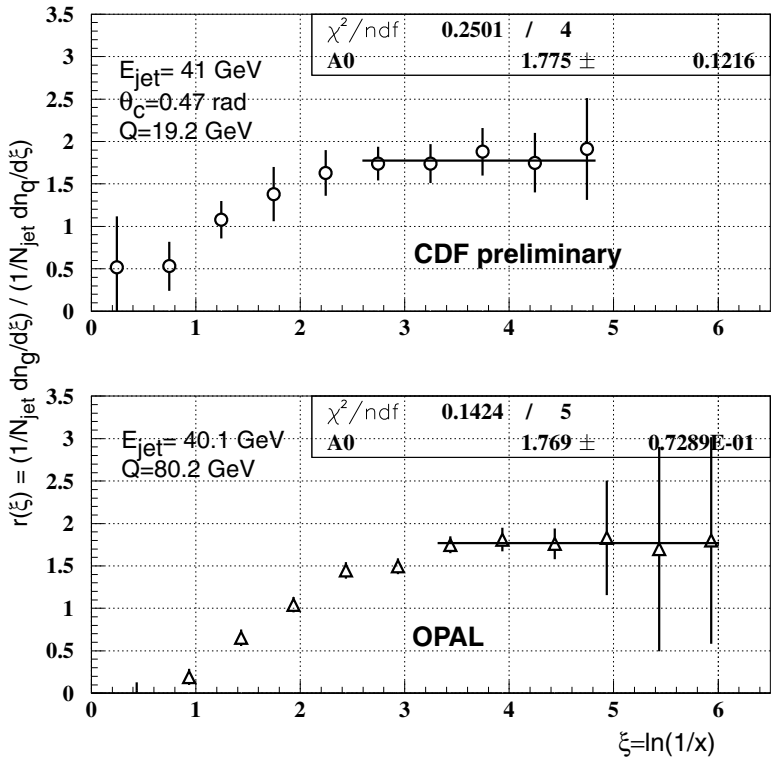

Figure 10–6: The ratio of momentum distributions, $r(\xi)$ (where $\xi = \ln(1/x) = \ln(E_{jet}/p)$), of charged particles in gluon and quark jets. Comparison of CDF and OPAL data.

picture of the effect is that soft gluons have long wavelengths and can not resolve individual partons within a jet. Instead, they only see the color charge of the initial parton. Thus, the ratio of mean multiplicities of soft gluons in gluon and quark jets, r_{soft}, should not depend on the energy scale and should approach the asymptotic value of $r_{soft} \to C_A/C_F$=2.25. As one can see from Fig. 10–6, the ratio $r(\xi)$ is significantly below unity for energetic particles, and it is monotonically growing as particle momentum gets softer. The ratio appears to saturate at $r_{soft} \simeq 1.8$ which is, however, still below the asymptotic value C_A/C_F=2.25. It is also interesting to note that the OPAL [54] experiment observed the same behavior of $r(\xi)$ and found that the ratio saturates at $r(\xi) \to r_{soft} \simeq 1.8$.

To get deeper insight on the origin of the disagreement in multiplicities between data and Monte Carlo, we compare inclusive momentum distributions of charged

particles. From Table 10–2 and Fig. 10–7, one can see that Herwig 5.6 results for charged particle momentum spectra in gluon jets are in a good agreement with data while Pythia 6.115 predicts somewhat higher number of charged particles in the region around the peak of distribution, $2.5<\xi<3.5$. In the case of quark jets (see Table 10–3 and Fig.10–8), both Herwig and Pythia disagree with data significantly, with Pythia predicting a slightly higher number of particles with $1.5<\xi<3.5$ than Herwig. The difference in the momentum distribution of particles from quark jets, $\frac{1}{N_{q.jet}}\frac{dN_q}{d\xi}$, further propagates into a difference in the ratio $r(\xi)$. Thus, both Herwig and Pythia qualitatively describe the data, but predict lower ratios in almost the entire range of particle momenta (see Table 10–4 and Fig.10–9). It is interesting to note that the shape of Herwig $r(\xi)$-distribution somewhat better resembles the trend in data ("leveling off" of $r(\xi)$ in the soft part of the momentum spectrum) than Pythia.

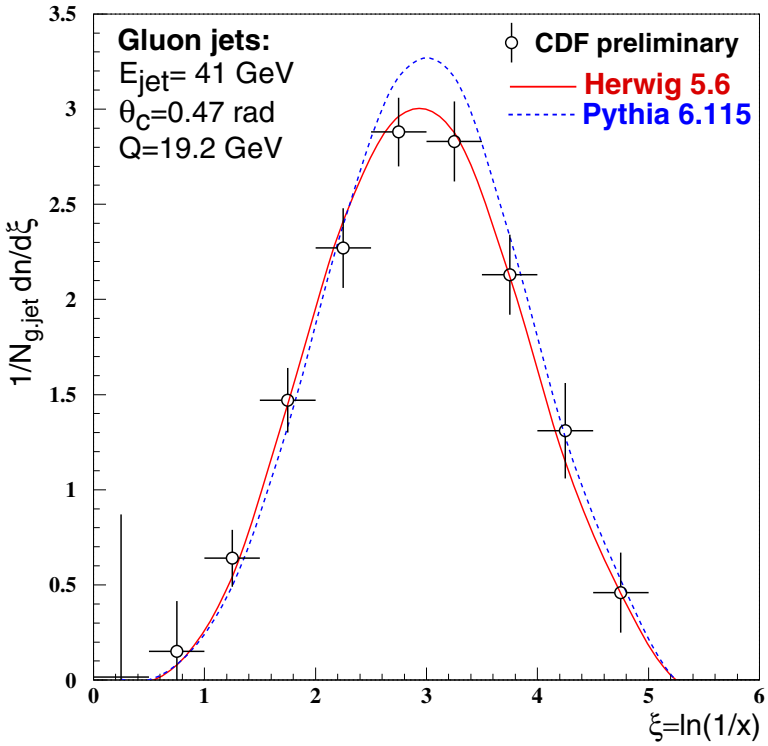

Figure 10–7: Inclusive momentum distribution, $\frac{1}{N_{jet}}\frac{dN}{d\xi}$ (where $\xi = \ln\frac{E_{jet}}{p}$), of charged particles in gluon jets. The results are presented for E_{jet}=41 GeV and the opening angle θ_c=0.47 rad. The integral of the distribution gives the average charged particle multiplicity in gluon jets. The error bars correspond to statistical and systematic uncertainties added in quadrature.

Table 10–2: Measured values of the momentum distribution, $\frac{1}{N_{jet}}\frac{dN}{d\xi}$, of charged particles in gluon jets. The results are presented for E_{jet}=41 GeV and the opening angle θ_c=0.47.

$\xi = \log\frac{E_{jet}}{p}$	Data	Herwig	Pythia
0.25	0.02±0.85±0.01	0.0020±0.0005	0.0052±0.0009
0.75	0.15±0.26±0.05	0.0793±0.0032	0.0818±0.0035
1.25	0.64±0.14±0.05	0.542±0.008	0.494±0.009
1.75	1.47±0.10±0.14	1.450±0.013	1.332±0.014
2.25	2.27±0.10±0.18	2.411±0.017	2.391±0.019
2.75	2.88±0.09±0.16	2.961±0.019	3.169±0.022
3.25	2.83±0.09±0.19	2.876±0.019	3.169±0.022
3.75	2.13±0.10±0.18	2.119±0.016	2.331±0.019
4.25	1.31±0.11±0.22	1.148±0.012	1.276±0.014
4.75	0.46±0.16±0.14	0.455±0.008	0.525±0.009

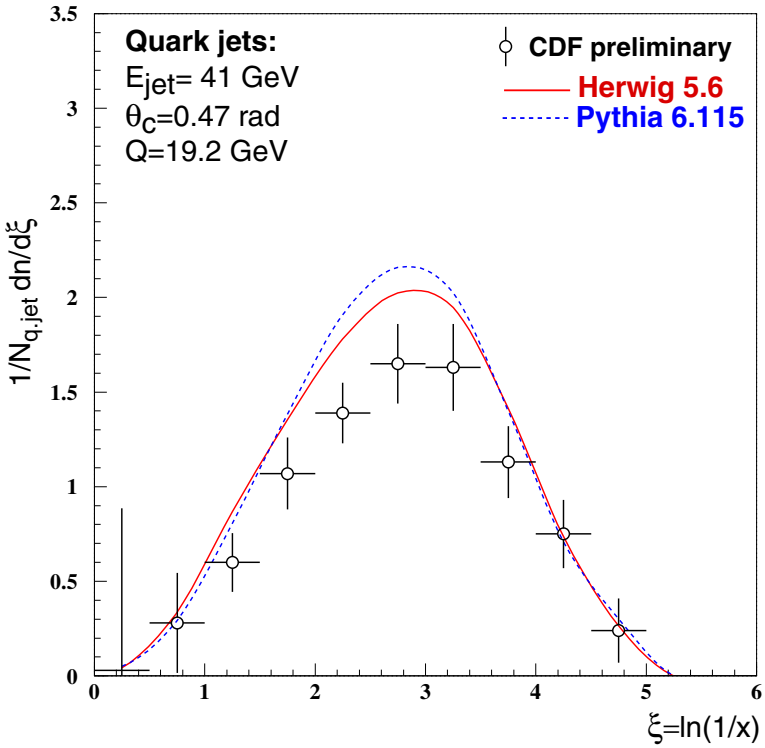

Figure 10–8: Inclusive momentum distribution, $\frac{1}{N_{jet}}\frac{dN}{d\xi}$ (where $\xi = \ln\frac{E_{jet}}{p}$), of charged particles in quark jets. The results are presented for E_{jet}=41 GeV and the opening angle θ_c=0.47 rad. The integral of the distribution gives the average charged particle multiplicity in quark jets. The error bars correspond to statistical and systematic uncertainties added in quadrature.

Table 10–3: Measured values of the momentum distribution, $\frac{1}{N_{jet}}\frac{dN}{d\xi}$, of charged particles in quark jets. The results are presented for E_{jet}=41 GeV and the opening angle θ_c=0.47.

$\xi = \log\frac{E_{jet}}{p}$	Data	Herwig	Pythia
0.25	0.03±0.85±0.01	0.0418±0.0029	0.0507±0.0035
0.75	0.28±0.26±0.04	0.332±0.008	0.294±0.009
1.25	0.60±0.15±0.04	0.868±0.013	0.806±0.014
1.75	1.07±0.12±0.15	1.355±0.017	1.384±0.019
2.25	1.39±0.12±0.11	1.780±0.019	1.908±0.022
2.75	1.65±0.12±0.17	2.023±0.020	2.158±0.023
3.25	1.63±0.12±0.20	1.946±0.020	2.024±0.022
3.75	1.13±0.11±0.15	1.413±0.017	1.399±0.019
4.25	0.75±0.12±0.13	0.738±0.012	0.709±0.013
4.75	0.24±0.16±0.06	0.264±0.007	0.301±0.009

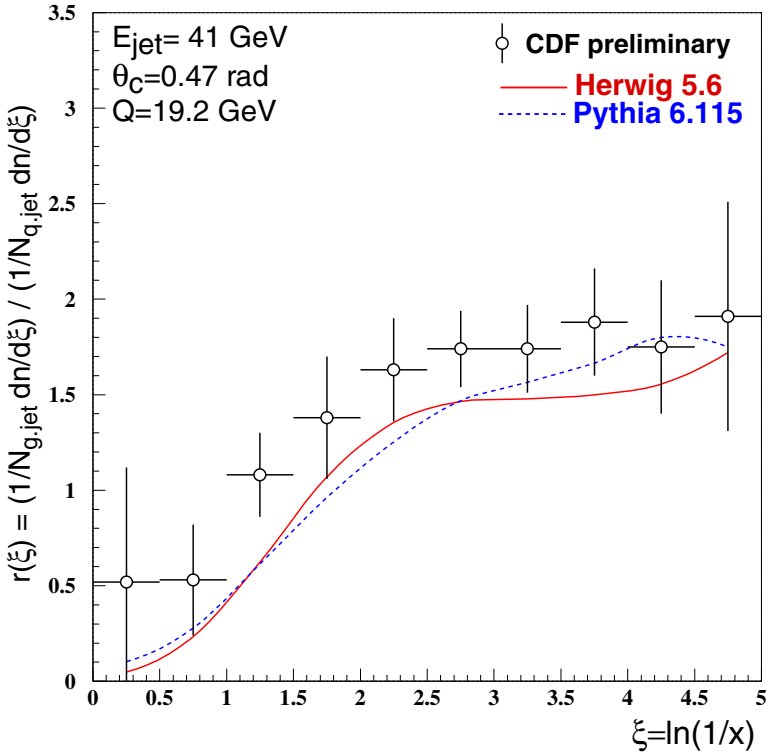

Figure 10–9: The ratio of momentum distributions, $r(\xi)$, of charged particles in gluon and quark jets. The results are presented for E_{jet}=41 GeV and the opening angle θ_c=0.47 rad. The error bars correspond to statistical and systematic uncertainties added in quadrature.

Table 10–4: Measured values of the ratio of momentum distributions, $r(\xi)$, of charged particles in gluon and quark jets. The results are presented for E_{jet}=41 GeV and the opening angle θ_c=0.47.

$\xi = \log \frac{E_{jet}}{p}$	Data	Herwig	Pythia
0.25	0.52±0.49±0.35	0.048±0.012	0.103±0.019
0.75	0.53±0.15±0.25	0.234±0.011	0.278±0.014
1.25	1.08±0.17±0.14	0.624±0.013	0.613±0.015
1.75	1.38±0.16±0.28	1.070±0.016	0.963±0.016
2.25	1.63±0.17±0.21	1.354±0.017	1.253±0.017
2.75	1.74±0.16±0.12	1.464±0.017	1.469±0.019
3.25	1.74±0.17±0.16	1.478±0.018	1.565±0.020
3.75	1.88±0.22±0.17	1.499±0.021	1.666±0.026
4.25	1.75±0.24±0.26	1.556±0.030	1.80±0.04
4.75	1.91±0.43±0.42	1.72±0.06	1.75±0.06

CHAPTER 11
SUMMARY AND CONCLUSION. FUTURE PERSPECTIVES

The study reported in this dissertation is the first model-independent measurement of quark and gluon jet properties using charged particles in a hadron collider environment. At $p\bar{p}$ collisions, jet production is a dominant process. Most of the jets produced are gluon jets. Unlike quark jets, our knowledge of gluon jet fragmentation is very limited. Until recently there have been only two model-independent measurements of gluon jet properties at well defined energy scales in e^+e^- collisions [50, 54]. This analysis improves our understanding of gluon jet fragmentation and proves that quark and gluon jet properties can be successfully studied in a largely model-independent way at hadron collisions. This independence is achieved by exploiting the difference in quark and gluon jet content of dijet events and γ+jet events in $p\bar{p}$ collisions. The analysis is carried out in the dijet or γ+jet center-of-mass frame, where the average jet energies are E_{jet}=41 and 53 GeV. The charged particle multiplicities in gluon and quark jets are measured in restricted cones with θ_c=0.28, 0.36, and 0.47 rad, where θ_c is the angle between the jet axis and the cone side.

In our measurements of multiplicity, we tried to reproduce theoretical assumptions as close as possible. Thus, we required only two high E_T back-to-back jets in the central η-region and counted particles in small opening angles. Furthermore, the small size of the cone and back-to-back geometry of events ensures unambiguous assignment of particles to jets. The contribution of the underlying event is subtracted by counting particles inside complementary cones.

The results of the analysis are compared to the theoretical predictions based on re-summed perturbative QCD calculations carried out in the framework of the

Modified Leading Log Approximation [22] and its extensions [24, 25, 26, 27], supplemented with the hypothesis of Local Parton-Hadron Duality [18]. The multiplicities in gluon and quark jets follow the predicted evolution with jet energy and opening angle as a function of $Q{=}E_{jet}\theta_c$. For the range of jet hardness 12 GeV $< Q <$ 25 GeV, the measured ratio of charged particle multiplicities in gluon and quark jets, $r = N_g/N_q$, varies between 1.5 and 1.7. At Q=19 GeV, the ratio is found to be r=1.64$\pm$0.17. This is in agreement with re-summed perturbative QCD calculations, 1.4$\leq r \leq$1.8 [24, 25, 26, 27]. Overall, the measured multiplicities in gluon and quark jets, as well as their ratio, are successfully described by recent NLLA expressions from Ref. [26] using the cut-off scale Q_{eff} =230 MeV [60]. This confirms that pQCD plays the dominant role in the jet fragmentation down to a very low scale—an observation made in earlier CDF model-dependent studies [59, 60].

The measured multiplicities in gluon and quark jets are found to be consistent with the data from e^+e^- experiments [50, 54, 55, 56, 75]. This consistency demonstrates the universality of jets produced in different environments.

The results on inclusive momentum distributions, $dN/d\xi$, of charged particles in gluon and quark jets and their ratio, $r(\xi)$, suggest that the multiplicity of energetic particles is higher in quark jets than in gluon jets ($r(\xi \to 0) \ll 1.0$). On the other hand, gluon jets have larger multiplicity of soft particles. Another interesting observation we make is that the ratio $r(\xi)$ appears to saturate in soft part of the momentum spectra at $r(\xi) \to r_{soft} \simeq 1.8$. The same behavior of $r(\xi)$ was also reported by OPAL [54].

When the results of the analysis are confronted with Monte Carlo predictions, we find that Herwig 5.6 and Pythia 6.115 reproduce the multiplicities in gluon jets fairly well, but they systematically overestimate the multiplicities in quark jets by as much as 30%. The analysis of the momentum distributions in quark jets reveals that most of the disagreement between data and Monte Carlo occurs in the region of

intermediate particle's momenta (around the peak of the distribution). More detailed studies are needed in order to trace the origin of this disagreement.

The measurement reported in this dissertation confirms that gluon and quark jets exhibit significant difference in fragmentation ($1.5 < r < 1.7$) even at relatively low jet energies ($E_{jet} \sim 40$–50 GeV) and small opening angles ($0.3 < \theta_c < 0.5$). This actually opens a possibility to use the difference between quarks and gluons as an extra tool to suppress QCD multi-jet backgrounds in any measurements involving jets from $W^{\pm} \to q`\bar{q}"$ and $Z \to q\bar{q}$ decays (e.g., $t\bar{t} \to b\bar{b}W^+W^- \to b\bar{b}jjjj$ where the signal is all quark jets and the background is many gluon jets).

The high luminosity of Run 2 at the Tevatron opens many opportunities for more precise studies of fragmentation differences between quark and gluon jets. It would also allow to extend the range of jet energies where these studies can be done. As one of the possible measurements, it would be interesting to study in more detail various inclusive momentum distributions (e.g., $dN/d\xi$, $dN/dk_{\perp}$, $dN/dp_{||}$, etc.) of particles in gluon and quark jets.

Another interesting measurement which can be done is the study of the KNO scaling in the multiplicity distributions of charged particles in gluon and quark jets. The e^+e^- experiments studied in great detail this effect in quark jets. However, there is no data on KNO scaling in gluon jets. Moreover, it is in the fluctuations and correlations in particle production that the detailed information on the underlying dynamics is expected to manifest itself. Therefore, this measurement would definitely improve our understanding of jet fragmentation.

And finally, all these future measurements will definitely help to test and improve the modeling of fragmentation in Monte Carlo event generators. This becomes especially important given the fact that many measurements at hadron colliders heavily rely on Monte Carlo simulation in order to obtain jet energy corrections, evaluate backgrounds, estimate acceptances, etc.

REFERENCES

[1] J.F. Donoghue, E. Golowich, B.R. Holstein, "Dynamics of the Standard Model", Cambridge Monographs on Particle Physics, Nuclear Physics and Cosmology, CUP, 1996 (reprinted).

[2] G. Arnison *et al.* [UA1 Collaboration], Phys. Lett. B **122**, 103 (1983).

[3] P. Bagnaia *et al.* [UA2 Collaboration], Phys. Lett. B **122**, 476 (1983).

[4] G. Arnison *et al.* [UA1 Collaboration], Phys. Lett. B **126**, 398 (1983).

[5] P. Bagnaia *et al.* [UA2 Collaboration], Phys. Lett. B **129**, 130 (1983).

[6] F. Abe *et al.* [CDF Collaboration], Phys. Rev. Lett. **74**, 2626 (1995); S. Abachi *et al.* [D0 Collaboration], Phys. Rev. Lett. **74**, 2632 (1995)

[7] M. Breidenbach *et al.*, Phys. Rev. Lett. **23**, 935 (1969); J.L. Friedman and H.I. Kendall, Ann. Rev. Nucl. Part. Science **22**, 203 (1972).

[8] J.D. Bjorken, Phys. Rev. **179**, 1547 (1969).

[9] R.P. Feynmann, *Photon-Hadron Interactions*, W.A. Benjamin, New York (1972).

[10] M. Gell-Mann, Phys. Lett. **8**, 218 (1964); G. Zweig, CERN-8419-TH-412 (1964).

[11] O.W. Greenberg, Phys. Rev. Lett. **13**, 598 (1964).

[12] D.J. Gross and F. Wilczek, Phys. Rev. Lett. **30**, 1343 (1973); H.D. Pollitzer, Phys. Rev. Lett. **30**, 1346 (1973).

[13] R.K. Ellis, W.J. Stirling and B.R. Webber, *QCD and Collider Physics*, Cambridge Monographs on Particle Physics, Nuclear Physics and Cosmology, CUP, 1996.

[14] PDG, Phys. Rev. D, 1 (2002).

[15] R.F. Schwitters *et al.*, Phys. Rev. Lett. **35**, 1320 (1975);
G.G. Hanson *et al.*, Phys. Rev. Lett. **35**, 1609 (1975).

[16] R. Brandelik *et al.* [TASSO Collaboration], Phys. Lett. B **86**, 243 (1979); **94**, 437 (1980);
D.P. Barber *et al.* [MARK Collaboration], Phys. Rev. Lett. **43**, 830 (1979);

Ch. Berger *et al.* [PLUTO Collaboration], Phys. Lett. B **86**, 418 (1979); W. Bartel *et al.* [JADE Collaboration], Phys. Lett. B **91**, 142 (1980).

[17] Yu. Dokshitzer, V. Khoze, A. Mueller and S. Troyan, *Basics of Perturbative QCD*, edited by J. Tran Thanh Van (Editions Frontières, Gif-sur-Yvette, 1991).

[18] Ya.I. Azimov, Yu. Dokshitzer, V. Khoze and S. Troyan, Z. Phys. C **27**, 65 (1985); **31**, 213 (1986).

[19] V.N. Gribov and L.N. Lipatov, Sov. J. Nucl. Phys. **15**, 438 (1972); L.N. Lipatov, Sov. J. Nucl. Phys. **20**, 94 (1975); G. Altarelli and P. Parisi, Nucl. Phys. B **126**, 298 (1977); Yu.L. Dokshitzer, Sov. Phys. JETP **46**, 641 (1977).

[20] W. Furmanski, R. Petronzio and Pokorski, Nucl. Phys. B **155**, 253 (1979); A. Bassetto, M. Ciafaloni and G. Marchesini, Nucl. Phys. B **163**, 477 (1980); Yu.L. Dokshitzer, V.S. Fadin and V.A. Khoze, Phys. Lett. B **115**, 242 (1982); Z. Phys. C **15**, 325 (1982).

[21] B.I. Ermolayev and V.S. Fadin, JETP Lett. **33**, 285 (1981); A.H. Mueller, Phys. Lett. B **104**, 161 (1981).

[22] Yu.L. Dokshitzer and S.I. Troyan, Proc. 19^{th} Winter School of the LNPI, Vol. 1, p.144, Leningrad preprint LNPI-922 (1984); A.H. Mueller, Nucl. Phys. B **213**, 85 (1983).

[23] D. Amati and G. Veneziano, Phys. Lett. B **83**, 87 (1979); A. Bassetto, M. Ciafaloni and G. Marchesini, Phys. Lett. B **83**, 207 (1979); G. Marchesini, L. Trentadue and G. Veneziano, Nucl. Phys. B **181**, 335 (1981).

[24] J.B. Gaffney and A.H. Mueller, Nucl. Phys. B **250**, 109 (1985).

[25] S. Catani *et al.*, Nucl. Phys. B **377**, 445 (1992).

[26] A. Capella *et al.*, Phys. Rev. D **61**, 074009 (2000).

[27] S. Lupia and W. Ochs, Phys. Lett. B **418**, 214 (1998).

[28] S.J. Brodsky and J.F. Gunion, Phys. Rev. Lett. **37**, 402 (1976); K. Konishi, A. Ukawa, and G. Veneziano, Nucl. Phys. B **157**, 45 (1979).

[29] V.A. Khoze, S. Lupia and W. Ochs, Phys. Lett. B **386**, 451 (1996); Eur. Phys. J. C **5**, 77 (1998).

[30] G. Marchesini and B.R. Webber, Nucl. Phys. B **238**, 1 (1984); **310**, 461 (1984); G. Marchesini *et al.*, Comput. Phys. Commun. **67**, 465 (1992).

[31] H.-U. Bengtsson and T. Sjöstrand, Comp. Phys. Comm. **46**, 43 (1987); T. Sjöstrand *et al.*, Comput. Phys. Commun. **135**, 238 (2001).

[32] V.N. Gribov and L.N. Lipatov, Sov. J. Nucl. Phys. **15**, 675 (1972); *ibid*, 675; L.N. Lipatov, Sov. J. Nucl. Phys. **20**, 94 (1975); G. Altarelli and G. Parisi, Nucl. Phys. B **126**, 298 (1977); Yu.L. Dokshitzer, Sov. Phys. JETP **46**, 641 (1977).

[33] R.D. Field and S. Wolfram, Nucl. Phys. B **213**, 65 (1983); B.R. Webber, Nucl. Phys. B **238**, 492 (1984).

[34] X. Artu and G. Mennessier, Nucl. Phys. B **70**, 93 (1974); M.G. Bowler, Z. Phys. C **11**, 169 (1981); B. Andersson, G. Gustafson and B. Söderberg, Z. Phys. C **20** 317 (1983); Nucl. Phys. B **264**, 29 (1986).

[35] C. Peterson *et al.*, Phys. Rev. D **27**, 105 (1983).

[36] I.M. Dremin and J.W. Gary, Phys. Rept. **349**, 301 (2001).

[37] V. Khoze *et al.*, in *At the Frontier of Particle Physics: Handbook of QCD*, vol.2, p.1101, edited by M.A. Shifman (World Scientific, 2001).

[38] M. Derrick *et al.* [HRS Collaboration], Phys. Lett. B **165**, 449 (1985).

[39] G. Alexander *et al.* [OPAL Collaboration], Phys. Lett. B **265**, 462 (1991).

[40] P.D. Acton *et al.* [OPAL Collaboration], Z. Phys. C **58**, 387 (1993).

[41] S. Catani *et al.*, Phys. Lett. B **269**, 432 (1991).

[42] Y. Iwasaki for the SLD Collaboration, SLAC-PUB-6597, Aug 1994, Presented at DPF 94, Albuquerque, NM, Aug 2-6, 1994; Y. Iwasaki for the SLD Collaboration, SLAC-R-95-460, SLAC preprint, Stanford, 1995.

[43] R. Akers *et al.* [OPAL Collaboration], Z. Phys. C **68**, 179 (1995).

[44] G. Alexander *et al.* [OPAL Collaboration], Z. Phys. C **69**, 543 (1996).

[45] D. Busculic *et al.* [ALEPH Collaboration], Phys. Lett. B **346**, 389 (1995); Phys. Lett. B **384**, 353 (1996).

[46] P. Abreu *et al.* [DELPHI Collaboration], Z. Phys. C **70**, 179 (1996).

[47] W. Bartel *et al.* [JADE Collaboration], Z. Phys. C **33**, 23 (1986).

[48] P. Eden, G. Gustafson and V.A. Khoze, Eur. Phys. J. C **11**, 345 (1999).

[49] CLEO, M.S. Alam *et al.*., Phys. Rev. D **56** (1997) 17.

[50] CLEO, M.S. Alam *et al.*., Phys. Rev. D **46** (1992) 4822.

[51] G. Alexander *et al.* [OPAL Collaboration], Phys. Lett. B **388**, 659 (1996).

[52] J.W. Gary, Phys. Rev. **D49**, 4503 (1994).

[53] K. Ackerstaff *et al.* [OPAL Collaboration], Eur. Phys. J. C **1**, 479 (1998).

[54] G. Abbiendi *et al.* [OPAL Collaboration], Eur. Phys. J. C **11**, 217 (1999).

[55] G. Abbiendi *et al.* [OPAL Collaboration], Eur. Phys. J. C **23**, 597 (2002).

[56] G. Abbiendi *et al.* [OPAL Collaboration], hep-ex/0310048

[57] P. Eden and G. Gustafson, JHEP **9809**, 597 (1998).

[58] G. Gustafson, Phys. Lett. B **75**, 453 (1986); G. Gustafson and U. Petterson, Nucl. Phys. B **306**, 746 (1988); B. Andersson, G. Gustafson and L. Lönnblad, Nucl. Phys. B **339**, 393 (1990).

[59] T. Affolder *et al.* [CDF Collaboration], Phys. Rev. Lett. **87**, 211804 (2001).

[60] D. Acosta *et al.* [CDF Collaboration], Phys. Rev. D **68**, 012003 (2003).

[61] F. Abe *et al.*, Nucl. Instrum. Methods Phys. Res. A **271**, 387 (1988).

[62] D. Amidei *et al.*, Nucl. Instrum. Methods Phys. Res. A **269**, 68 (1988).

[63] J. Huth, Proc. of the DPF 90 summer study on HEP, Snowmass, Colorado, World Scientific (1990).

[64] F. Abe *et al.*, Phys. Rev. D **45**, 1448 (1992).

[65] F. Abe *et al.*, Phys. Rev. D **48**, 2998 (1993)

[66] M. Shapiro, A. Bhatti, J. Benlloch, R. Harris, T. Rodrigo, P. Sphicas, and T. Westhusing, CDF note 1810.

[67] T. Affolder *et. al.*, Phys. Rev. D, **64**, 032001 (2001).

[68] D. Acosta *et al.*, Phys. Rev. D **65**, 112003 (2002).

[69] H.L. Lai *et al.*, Phys. Rev. D **55**, 1280 (1997).

[70] A. Korytov, A. Safonov, *CTC Track Reconstruction Efficiency in Jets*, CDF note 4883, February 9, 1999.

[71] V.A. Khoze, W.J. Stirling, Z. Phys. C **76**, 59 (1997).

[72] B. Abbott *et al.* [D0 Collaboration], Phys. Lett. B **464**, 145 (1999).

[73] S. Kuhlman, *Underlying Event E_T in Cones*, CDF note 1559, October 7, 1991.

[74] L. Galtieri, J. Lys, *How well do we understand jets in Run I? Study of the Jet Energy Scale for Raw Jet $E_T \geq 8GeV$*, CDF note 3983, December 9, 1996.

[75] Mark II Collab.: P.C. Rowson *et al.*, Phys. Rev. Lett. **54**, 2580 (1985); TPC Collab.: H. Aihara *et al.*, Phys. Lett. B **184**, 299 (1987); CLEO Collab.: M.S.

Alam et al., Phys. Rev. D **46**, 4822 (1992); SLD Collab.: K. Abe *et al.*, Phys. Lett. B **386**, 475 (1996); DELPHI Collab.: P. Abreu *et al.*, Eur. Phys. J. C **6**, 19 (1999); Phys. Lett. B **479**, 118 (2000); Erratum *ibid.* **492**, 398 (2000); OPAL Collab.: K. Ackerstaff *et al.*, Eur. Phys. J. C **1**, 479 (1998); G. Abbiendi *et al.*, Phys. Lett. B **550**, 33 (2002).

[76] I.M. Dremin and J.W. Gary, Phys. Lett. B **459**, 341 (1999).

BIOGRAPHICAL SKETCH

Alexandre P. Pronko was born on April 13, 1976, in the village of Juprany in Belarus. After graduating from high school in 1993, he continued his education in the Moscow Institute of Physics and Technology, MIPT (State University).

In 1997 he received his Bachelor of Science degree. In 1999 he received his master's degree *with highest distinction* from the same university. While studying in MIPT, he worked in the Institute for Theoretical and Experimental Physics with Professor Yuri M. Zaitsev. Alexandre's research work was related to the muon identification in the HERA-B experiment.

In the summer of 1999 Alexandre P. Pronko became a graduate student in the Department of Physics, University of Florida. In 2001 he joined the CDF Collaboration and worked with Professor Andrey Korytov on various aspects of experimental physics, particularly the jet fragmentation. In 2001-2005 Alexandre took a critical part in software development and operations of the Cherenkov Luminosity Counter during Run 2 at CDF.

In 2005, Alexandre P. Pronko graduated from the University of Florida with the degree of Doctor of Philosophy.